MAGYAR ÁLLAMI
EÖTVÖS LORÁND
GEOFIZIKAI INTÉZET

EÖTVÖS LORÁND
GEOPHYSICAL INSTITUTE
OF HUNGARY

GEOFIZIKAI KÖZLEMÉNYEK

GEOPHYSICAL TRANSACTIONS

ВЕНГЕРСКИЙ
ГЕОФИЗИЧЕСКИЙ
ИНСТИТУТ
ИМ Л. ЭТВЕША

ГЕОФИЗИЧЕСКИЙ
БЮЛЛЕТЕНЬ

CONTENTS

VOL. 33. NO. 2. NOV. 1987. (ISSN 0016—7177)

BUDAPEST

TARTALOMJEGYZÉK

СОДЕРЖАНИЕ

GEOPHYSICAL TRANSACTIONS 1987
Vol. 33. No 2. pp. 69–87

A DISCRETE-TIME INVERSE SCATTERING ALGORITHM FOR PLANE WAVE INCIDENCE IN A ONE-DIMENSIONAL INHOMOGENEOUS ACOUSTIC MEDIUM

Frederic B. LEYDS* and Jacob T. FOKKEMA*

A frequency based algorithm is developed to calculate the reflected acoustic signal resulting from plane wave incidence on a horizontally layered acoustic half-space. This forward modelling algorithm is inverted to yield a layer-peeling inversion algorithm to recover the acoustic impedance in each layer, using the principle of causality. At postcritical incidence, the development of an inverse algorithm is impossible because the evanescent waves in the horizontally layered half-space create a non-causal contribution to the scattered field.

The forward and inverse algorithms are tested for a complicated geology based on real well-log data. The inversion of synthetic signals produces excellent results. Experiments show that the inverse algorithm is sensitive to white noise. It remains stable only when those frequencies of the scattered field are used, at which the amplitude of the incident field visibly exceeds the amplitude of the noise. With this reduction of the bandwidth, the impedance profile of a geology of 684 layers can be recovered at a noise-to-signal ratio of 2% (r.m.s.). A simple geology of eight layers can be recontsructed at a noise-to-signal ratio of up to 30%, but only if recovered reflection coefficients within the noise range are removed by a threshold filter before the acoustic impedance profile is derived.

Keywords: plane wave, scattering, seismic inversion, signal-to-noise ratio, acoustical waves, one-dimensional models, algorithms, synthetic seismograms

1. Introduction

In seismic exploration, the measurement of a scattered wave field is used to obtain information about the structure of an often complicated subsurface geology. However, individual traces measured in the field usually do not allow for immediate and exact scaling and location of the elastic or acoustic parameters. All the field measurements must be used to determine the response of the geology from which, as a last step of the data processing, the parameters can be estimated.

The research presented in this article describes a method for obtaining the acoustic layer parameters from the individual plane wave components of a one shot gather over a horizontally layered geology. This is an unrealistic problem, because the layers usually have some dip. However, such a shot gather is approximated by a common-mid-point (CMP) gather of seismic field recordings [see, for example, ROBINSON and TREITEL 1980, Ch. 1].

* Delft University of Technology, Dept. of Mining Engineering. Lab. of Applied Geophysics, Mijnbouwstraat 120, 2628 RX Delft, the Netherlands
Paper presented at the 47th meeting of the EAEG, 4–7 June, 1985, Budapest, Hungary

In other words, the input data of the inversion method investigated here are presumed to be the result of a successful plane wave decomposition of common-mid-point data, that has reduced the inversion to essentially a one-dimensional problem. Only synthetic input data are used in this article. The plane wave decomposition itself is not discussed.

The inversion algorithm used here is based on a procedure which SCHUR [1917] developed for testing the boundedness of complex functions that are analytic inside the unit circle in the complex z-plane. BRUCKSTEIN, LEVY and KAILATH [1983] give an account of its use as an inversion algorithm following work done by GOUPILLAUD [1961], CLAERBOUT [1976] and ROBINSON [1982], while YAGLE and LEVY [1984] discussed some of its applications. In this article, the inversion algorithm is developed for solving our particular problem, and its behaviour in the case of postcritical incidence is examined. The algorithm is tested on a digital computer using synthetic seismic responses.

We begin with the configuration of the model and describe the forward modelling procedure for simulating the plane wave response of a horizontally-layered acoustic earth. Then the inverse problem is tackled. A key assumption is that the layer thickness and velocity parameters coincide with the time discretization. This allows a layer peeling inversion algorithm to be made. Specific problems in the case of postcritical incidence are treated in a separate section. It will be shown that for postcritical incidence a non-causal distortion in the seismic signal destroys the inversion algorithm.

Finally, the computer implementation is briefly discussed and some results are presented. The sensitivity to noise of the inversion is also investigated.

2. Model configuration and representation of the acoustic wave field

The geological model consists of a set of N horizontal homogeneous acoustic layers L_n, sandwiched between upper and lower homogeneous acoustic half-spaces, L_0 and L_{N+1} respectively. The configuration in which actual seismic data are obtained is always bounded at the top by a free surface. If the source is a monopole with dimensions small compared with a wavelength (for example a dynamite source), then the field data may be decomposed into plane waves [see, for example, TREITEL, GUTOWSKI and WAGNER 1982]. These plane wave components still contain the effects of the free surface, including multiples in the upper layer. In this paper it is assumed that the effects of the free surface have been removed and that the upper layer is a half-space. This half-space is represented by L_0.

The origin is chosen in the upper half-space, with the z-axis pointing downwards vertically along the normal to the layer interfaces; layer interfaces are defined by $z = z_n$ *(Fig. 1)*. Using this configuration, the scattered wave field as caused by an incident plane wave is examined. Under these circumstances it is clear that the wave field consists of plane waves throughout the model.

The theory is treated in the frequency (f) domain. The acoustic pressure

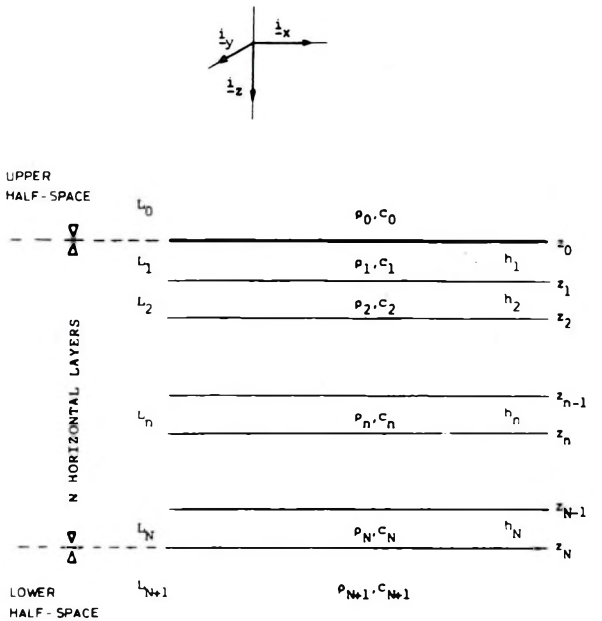

Fig. 1. The configuration
1. ábra. A modell
Рис. 1. Модель.

$\hat{P}$ is governed by the source-free wave equation:

$$\Delta \hat{P} + k^2 \hat{P} = 0 \tag{1}$$

where Δ is the Laplacian operator, k is the wavenumber:

$$k = (2\pi f)/c \tag{2}$$

and the acoustic wavespeed is:

$$c = (K/\varrho)^{1/2} \tag{3}$$

in which K is the bulk modulus and ϱ is the density.

The Fourier transform is defined as:

$$\hat{P}(f) = \int_{-\infty}^{+\infty} P(t) \exp(+i2\pi f t)\, dt \tag{4}$$

$$P(t) = \int_{-\infty}^{+\infty} \hat{P}(f) \exp(-i2\pi f t)\, df. \tag{5}$$

The wave fields in adjacent layers are coupled by two boundary conditions. These impose continuity on the pressure and on the vertical component of the particle velocity, everywhere along a layer interface:

$$\hat{P}_{n+1}(x, y, z_n, f) = \hat{P}_n(x, y, z_n, f) \quad \text{for all } f, x, y \quad \text{for } n = 0, 1, \ldots, N \tag{6}$$

and:

$$\hat{V}_{z,n+1}(x, y, z_n, f) = \hat{V}_{z,n}(x, y, z_n, f) \quad \text{for all } f, x, y \quad \text{for } n = 0, 1, \ldots, N. \tag{7}$$

In the frequency domain the vertical component of the particle velocity can be expressed in terms of pressure as follows:

$$\hat{V}_{z,n} = \frac{1}{\mathrm{i}2\pi f \varrho_n} \frac{\partial \hat{P}_n}{\partial z} \tag{8}$$

In a layer L_n two plane-wave solutions of the wave equation (1) can be distinguished, denoted by $\hat{P}_n^d$ and $\hat{P}_n^u$ respectively:

$$\hat{P}_n = \hat{P}_n^d + \hat{P}_n^u \tag{9}$$

$$\hat{P}_n^d = \hat{D}_n(f) \exp\{\mathrm{i}2\pi f(\alpha_n x + \beta_n y + \gamma_n z)/c_n\} \tag{10}$$

$$\hat{P}_n^u = \hat{U}_n(f) \exp\{\mathrm{i}2\pi f(\alpha_n x + \beta_n y - \gamma_n z)/c_n\} \tag{11}$$

where:

$$\gamma_n = (1 - \alpha_n^2 - \beta_n^2)^{1/2} \tag{12}$$

$$\text{with: } \mathrm{Re}\{\gamma_n\} \geqq 0 \tag{13}$$

$$\text{and: } \mathrm{Im}\{\gamma_n\} \geqq 0 \tag{14}$$

With this choice of γ_n and with the complex time factor $\exp(-\mathrm{i}2\pi f t)$, $\hat{P}_n^d$ represents a plane wave either propagating or decaying in the positive z-direction (i.e. downwards), whereas $\hat{P}_n^u$ represents a plane wave propagating or decaying in the negative z-direction (i.e. upwards).

The absence of discontinuities in the x and y directions yields Snell's law:

$$\frac{\alpha_n}{c_n} = \frac{\alpha_{n-1}}{c_{n-1}} = \frac{\alpha_0}{c_0} \tag{15}$$

and:

$$\frac{\beta_n}{c_n} = \frac{\beta_{n-1}}{c_{n-1}} = \frac{\beta_0}{c_0}. \tag{16}$$

In the upper half-space the downward-travelling wave corresponds to the incident fields as caused by the seismic source:

$$\hat{P}_0^d(x, y, z, f) = \hat{D}_0(f) \exp\{\mathrm{i}2\pi f(\alpha_0 x + \beta_0 y + \gamma_0 z)/c_0\} \tag{17}$$

while the upward-travelling wave, disappearing into the upper half-space, corresponds to the observed and recorded reflected field:

$$\hat{P}_0^u(x, y, z, f) = \hat{U}_0(f) \exp\{\mathrm{i}2\pi f(\alpha_0 x + \beta_0 y - \gamma_0 z)/c_0\} \tag{18}$$

where:

$$\alpha_0 = \sin(\Theta_0)\cos(\Psi_0) \tag{19}$$

$$\beta_0 = \sin(\Theta_0)\sin(\Psi_0) \tag{20}$$

$$\gamma_0 = \cos(\Theta_0) \tag{21}$$

with $0 \leqq \Theta_0 \leqq \pi/2$ and $0 \leqq \Psi_0 \leqq 2\pi$ in which Θ_0 and Ψ_0 are the vertical and horizontal components respectively of the spherical coordinates as shown in *Fig. 2.*

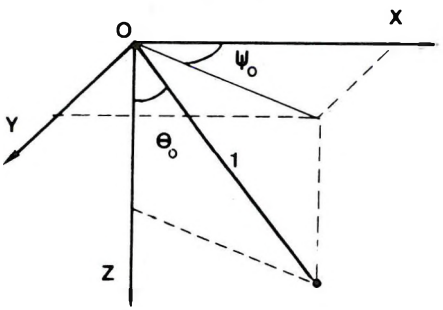

Fig. 2. Definition of spherical coordinates Ψ_0 and Θ_0

2. ábra. A Ψ_0 és Θ_0 gömbi koordináták definiciója

Рис. 2. Определение сферических координат Ψ_0 и Θ_0.

In the *forward* problem the structure of the model is given and, for a given incident field, the reflected field is to be computed. In the *inverse* problem the subsurface is unknown and must be reconstructed from measurements of the reflected field, using prior knowledge of the incident field and of the acoustic properties of the upper half-space only. In the research presented here the inversion aims at recovering the acoustic impedance profile; no attempt is made to recover the velocity and density profiles.

3. The forward problem

The relations obtained so far must be evaluated further to construct the wave field in all layers. As an aid in this construction, the *global reflection coefficient* of a layer L_n is defined as the ratio between upward- and downward-propagating wave fields, at a point just above the lower boundary $z = z_n$ of that layer:

$$\hat{R}_n(f) = \frac{\hat{P}_n^u(x, y, z_n, f)}{\hat{P}_n^d(x, y, z_n, f)} \tag{22}$$

or:

$$\hat{R}_n(f) = \frac{\hat{U}_n(f)}{\hat{D}_n(f)} \exp(-i4\pi f \gamma_n z_n / c_n) \tag{23}$$

It should be noted that the global reflection coefficient in the upper half-space equals the impulse response of the geology as measured just above the top layer.

By applying the boundary conditions Eqs. (6) and (7), and using the transmission property of a plane wave in a layer, the following recursion formula for the global reflection coefficient in layer L_n is obtained:

$$\hat{R}_n(f) = r_n + \frac{(1-r_n^2)\,\hat{R}_{n+1}(f)\,\hat{W}_{n+1}(f)}{1+r_n\hat{R}_{n+1}(f)\,\hat{W}_{n+1}(f)} \qquad \text{for } n = N-1, N-2, \ldots, 1, 0 \tag{24}$$

in which r_n is the local reflection coefficient at interface $z = z_n$ for a plane wave travelling downwards:

$$r_n = \frac{Y_n - Y_{n+1}}{Y_n + Y_{n+1}} \tag{25}$$

where Y_n is the z-component of the acoustic admittance:

$$Y_n = \gamma_n/\varrho_n c_n \tag{26}$$

and in which $\hat{W}_{n+1}(f)$ is the two-way phase delay of layer L_{n+1}:

$$\hat{W}_{n+1}(f) = \exp(\mathrm{i}2\pi f\tau_{n+1}) \tag{27}$$

where:

$$\tau_{n+1} = 2h_{n+1}\gamma_{n+1}/c_{n+1}. \tag{28}$$

It must be noted that τ_n is the two-way travel time within the nth layer for a propagating wave (in which γ_n is real).

The recursion process is initiated in the lower half-space L_{N+1} by imposing the radiation condition: this half-space does not contain any reflectors and therefore it contains no upward-travelling wave. Hence:

$$\hat{R}_N(f) = r_N. \tag{29}$$

Starting from this condition, the global reflection coefficient is calculated step by step in each layer L_n using the recursion formula (24) as an upwards moving operator:

$$\hat{R}_n(f) = \mathrm{UP}[\hat{R}_{n+1}](f) \tag{30}$$

The final outcome of this process is the global reflection coefficient in the upper half-space $\hat{R}_0(f)$. From Eqs. (17), (18) and (22) it can be seen that the reflected field at any point in the upper half-space can be expressed in terms of the spectrum of the incident field $\hat{D}_0(f)$:

$$\hat{P}_0^u(x, y, z_0, f) = \hat{R}_0(f)\,\hat{P}_0^d(x, y, z_0, f) \tag{31}$$

or

$$\hat{P}_0^u(x, y, z, f) = \hat{R}_0(f)\,\hat{D}_0(f)\exp\{i2\pi f(\alpha_0 x + \beta_0 y + \gamma_0(2z_0 - z))/c_0\} \qquad (32)$$

This is the solution of the forward problem. This solution is well-known as the 'reflectivity method' and can be found in many texts, see for example [KENNETT 1985].

4. The inverse problem

In order to solve the inverse problem, first the upwards moving operator (Eq. 30) is inverted to give a downwards moving operator:

$$\hat{R}_{m+1}(f) = \mathrm{DOWN}[\hat{R}_m](f) \qquad \text{for } m = M-1, M-2, \ldots, 1, 0 \qquad (33)$$

where:

$$\mathrm{DOWN}[\hat{R}_m](f) = \left[-r_m + \frac{(1-r_m^2)\hat{R}_m(f)}{1 - r_m\hat{R}_m(f)}\right]\hat{W}_{m+1}^{-1}(f) \qquad (34)$$

and in which the set of inverse recursion steps m is not yet determined. In the forward problem, recursion steps spanned the two-way travel times in the successive layers. In the inverse problem, of course nothing about the subsurface is known.

We now take advantage of the discretization of our time domain data. Following GOUPILLAUD [1961], the time discretization is taken as a constant recursion step, such that:

$$\hat{W}_m(f) = \exp\{i2\pi f\tau_m\} \qquad (35)$$

$$\text{where: } \tau_m = \Delta t \qquad \text{for } m = M-1, M-2, \ldots, 1, 0 \qquad (36)$$

This implies that our band-limited response can be described in terms of discrete layers L_m, each of which has a two-way travel time Δt. The aim of the recursion is now to find the contrast, if any, between these layers. It must be emphasized, in accordance with what has been said about the meaning of τ_n following equation (28), that this only makes sense for precritical reflection.

The frequency domain associated with discrete time sampling is periodic; the Fourier transform pair corresponding to this situation is as follows:

$$\hat{P}(f) = \sum_{n=-\infty}^{+\infty} P[n]\exp(+i2\pi f n\Delta t) \qquad (37)$$

$$P[n] = \Delta t \int_{-1/(2\delta t)}^{+1/(2\delta t)} \hat{P}(f)\exp(-i2\pi f n\Delta t)\,df \qquad (38)$$

As stated above, in the inverse problem both the incident field and the reflected field are known. The inverse recursion process is initiated in the upper half-space L_0 by:

$$\hat{R}_0(f) = \frac{\hat{P}_0^u(x, y, z_0, f)}{\hat{P}_0^d(x, y, z_0, f)} \tag{39}$$

or:

$$\hat{R}_0(f) = \frac{\hat{P}_0^u(x, y, z, f)}{\hat{D}_0(f)} \exp\{-i2\pi f(\alpha_0 x + \beta_0 y + \gamma_0(2z_0 - z))/c_0\}, \tag{40}$$

where the reflected field $\hat{P}_0^u(x, y, z, f)$ corresponds to the field measurement, while the division by $\hat{D}_0(f)$ represents the process of deconvolution, and removes the source function.

Before each step of the inverse recursion (33), the next local reflection coefficient must be determined. For this purpose, the forward recursion formula (24) is dissected by expanding $\hat{R}_m(f)$ and all its intrinsic previous $\hat{R}_i(f)$ into a Taylor series; this is rather like taking apart a set of nested Matryoshka dolls. Each term of this Taylor series consists of a combination of local reflection coefficients with an exponential factor, expressing a particular scattering path and its two-way travel time. After adding up terms with a common exponential factor, an expression of the following form is obtained:

$$\hat{R}_m(f) = r_m + \sum_{k=1}^{\infty} A_k^{(m)} \exp(i2\pi f k \Delta t) \tag{41}$$

where each coefficient $A_k^{(m)}$ is a sum of combinations of the local frequency-independent reflection coefficients r_i and is therefore also frequency independent. It should be noted that the summation starts at $k = 1$; no zero-order exponentials occur in the summation. The inverse Fourier transform (Eq. 38) is then applied:

$$R_m[n] = \Delta t \int_{-1/(2\Delta t)}^{+1/(2\Delta t)} \hat{R}_m(f) \exp(-i2\pi f n \Delta t)\, df \tag{42}$$

or:

$$\begin{aligned} R_m[n] = {} & r_m \int_{-1/(2\Delta t)}^{+1/(2\Delta t)} \exp(-i2\pi f n \Delta t)\, df + \\ & + \sum_{k=1}^{\infty} A_k^{(m)} \Delta t \int_{-1/(2\Delta t)}^{+1/(2\Delta t)} \exp\{-i2\pi f(n-k)\Delta t\}\, df \end{aligned} \tag{43}$$

The first integral on the right hand side of the above relation results in one pulse at $t = 0$. The summed integrals in the second part produce a series of pulses, all occurring *after* $t = 0$:

$$R_m[n] = r_m \delta[n] + \sum_{k=1}^{\infty} A_k^{(m)} \delta[n-k] \tag{44}$$

Now it is clear that for $n = 0$:

$$R_m[0] = r_m \tag{45}$$

It will be recognized that this illustrates the causality principle. The first sample of a reflected signal is a single primary reflection, uncontaminated by primary or multiple reflections from deeper layers, which must all arrive later. As $R_m[n]$ represents an impulse response, the amplitude of this first sample is equal to r_m, the local reflection coefficient of the 'shallowest' reflector.

In order to derive r_m directly from the frequency domain of the global reflection coefficient, equations (42) and (45) are combined:

$$r_m = \Delta t \int_{-1/(2\Delta t)}^{+1/(2\Delta t)} \hat{R}_m(f)\,\mathrm{d}f \tag{46}$$

After computation of one local reflection coefficient by means of the method described above, it can be used in the inverse recursion formula (34) to remove from the signal all effects of this reflector and the underlying layer, including multiple reflections, thus arriving at the next global reflection coefficient:

$$\hat{R}_{m+1}(f) = \mathrm{DOWN}\,[\hat{R}_m]\,(f) \tag{47}$$

The inversion process becomes a sequence of alternately calculating a local reflection coefficient (Eq. 46) and applying the downward operator (Eq. 47). In this manner, having initiated the procedure in the upper half-space with formula (40), a maximum of $M+1$ reflectors or M layers can be identified.

recursion:	$\hat{R}_0$	$\overset{*}{\rightarrow} r_0$	$\overset{\delta}{\rightarrow} \hat{R}_1$	$\overset{*}{\rightarrow} r_1$	$\overset{\delta}{\rightarrow} \hat{R}_2$	$\overset{*}{\rightarrow} r_2$	...	$\hat{R}_M \overset{*}{\rightarrow} r_M$
time:	0		Δt		$2\Delta t$		...	$M\Delta t$
layer No.:		1		2			...	M

Fig. 3. Inverse recursion scheme
* — calculation of reflection coefficient r_m with Eq. (46); δ — applying the DOWN-operator with Eq. (47)

3. ábra. Az inverz rekurziós séma
* — az r_m reflexiós együttható számítása a (46) egyenlettel; δ — a DOWN operátor alkalmazása a (47) egyenlettel

Рис. 3. Схема обращенной рекурсии
* — расчет коэффициента отражения r_m по уравнению (46); δ — применение оператора DOWN по уравнению (47).

The inversion scheme is illustrated in *Fig. 3.* The final result is a trace containing the recovered local reflection coefficients, at a constant interval of Δt. Finally, from the reflection coefficients, using the inverted version of formula (25), a profile can be derived of the vertical component of the acoustic admittance:

$$Y_{m+1} = \frac{1 - r_m}{1 + r_m} Y_m \tag{48}$$

with:

$$Y_m = \frac{\gamma_m}{\varrho_m c_m} \tag{49}$$

5. Postcritical incidence

It is necessary to reassess equations (41) to (45) for postcritical incidence. This is reached when:

$$\frac{1}{c_{K+1}^2} < \frac{1}{c_0^2}(\alpha_0^2 + \beta_0^2) \tag{50}$$

in a layer L_{K+1}. It follows from equations (15), (16) and (12) that γ_{K+1} is now purely imaginary. From equations (25) and (26) it then follows that the local reflection coefficient is complex and depends on the sign of the frequency:

$$\hat{r}_K(f) = \exp\left(-\mathrm{i}2\varepsilon \frac{f}{|f|}\right) \tag{51}$$

where:

$$\varepsilon = \arctan\left(\frac{|\gamma_{K+1}|}{\gamma_K} \frac{\varrho_K c_K}{\varrho_{K+1} c_{K+1}}\right), \tag{52}$$

This has grave consequences for the recursion process and for the relations as derived from equation (41) onwards, where the forward recursion formula was expanded into a Taylor series. The expansion converges on condition that:

$$|\hat{r}_m(f)|\,|\hat{R}_{m+1}(f)|\,|\hat{W}_{m+1}(f)| < 1 \tag{53}$$

From expression (51) it is clear that

$$|\hat{r}_K(f)| = 1 \tag{54}$$

This latter property may pose a threat to the convergence of the Taylor expansion. In all recursion steps through layers of *pre*critical incidence, the two-way transmission factor $\hat{W}_{m+1}(f)$ as defined in Eq. (27) is a complex exponent and the local reflection coefficient r_m is a real number:

$$|\hat{W}_{m+1}(f)| = 1 \tag{55}$$

$$r_m \leqq 1 \tag{56}$$

On the other hand, in recursion steps through layers of *post*critical incidence, the transmission factor is a real decay factor, and the local reflection coefficient is now complex with modulus 1:

$$\hat{W}_{m+1}(f) \leqq 1 \tag{57}$$

$$|\hat{r}_m(f)| = 1 \tag{58}$$

In fact, if critical reflection is reached in layer L_{K+1}, it can easily be shown that:

$$|\hat{R}_m(f)| \leqq 1 \quad \text{for} \quad m = K+1, \ldots, M-1, M \tag{59}$$

$$|\hat{R}_m(f)| = 1 \quad \text{for} \quad m = 0, 1, \ldots, K-1, K. \tag{60}$$

Relations (55) to (60) show that expression (53) always contains at least one factor of magnitude less than one, which secures the convergence of the Taylor expansion; it is 'safe' for both precritical and postcritical incidence.

The whole analysis from equation (41) onwards is now reconsidered by examining the simple case of postcritical incidence in the lower half-space L_{M+1}. As before, each term in the Taylor series of $\hat{R}_m(f)$ represents a particular scattering path. Some of these terms contain the complex $\hat{r}_M(f)$ at least once, the number of times depending on how often the postcritical reflection surface $z = z_M$ is included in that particular scattering path. The smallest exponential factor attached to one of these terms is $\exp\{i2\pi f(M-m)\Delta t\}$, which expresses the earliest or primary postcritical reflection .

As before, terms with a common exponential factor are collected into a single coefficient. However, frequency dependent terms containing $\hat{r}_M(f)$ are here isolated in a separate summation:

$$\hat{R}_m(f) = r_m + \sum_{k=1}^{\infty} \hat{A}_k^{(m)} \exp(i2\pi f k\Delta t) + \sum_{k=M-m}^{\infty} \hat{B}_k^{(m)}(f) \exp(i2\pi f k\Delta t) \tag{61}$$

$$\text{for} \quad m < M$$

Every term $\hat{B}_k^{(m)}(f)$ in the second summation on the right hand side has the form of a summation itself:

$$\hat{B}_k^{(m)}(f) = \sum_{j=1}^{\infty} G_{k,j}^{(m)} \exp\left(-i2\varepsilon j \frac{f}{|f|}\right) \tag{62}$$

where j indicates the number of reflections at interface $z = z_M$ and $G_{k,j}^{(m)}$ is a real and frequency independent factor representing the sum of all possible scattering paths between m and M for a given j and two-way traveltime $k\Delta t$.

Applying an inverse Fourier transform (Eq. 38) to $\hat{B}_k^{(m)}(f)$ leads to:

$$B_k^{(m)}[0] = \sum_{j=1}^{\infty} G_{k,j}^{(m)} \cos(2\varepsilon j) \tag{63}$$

and:

$$B_k^{(m)}[n] = \sum_{j=1}^{\infty} G_{k,j}^{(m)} \frac{-2\sin(2\varepsilon j)}{\pi n} \qquad \text{for } |n| = 1, 3, 5\ldots \tag{64}$$

$$B_k^{(m)}[n] = 0 \qquad \text{for } |n| = 2, 4, 6\ldots \tag{65}$$

Equations (44) and (45) now appear as:

$$R_m[n] = r_m\delta[n] + \sum_{k=1}^{\infty} A_k^{(m)}\delta[n-k] + \sum_{k=M-m}^{\infty} B_k^{(m)}[n-k] \tag{66}$$

and:

$$R_m[0] = r_m + \sum_{k=L}^{\infty}\sum_{j=1}^{\infty} G_{(2k+1),j}^{(m)} \frac{2\sin(2\varepsilon j)}{\pi(2k+1)}$$
$$\text{with} \quad L = (M-m-1)/2 \qquad \text{for odd } (M-m)$$
$$\text{or} \quad L = (M-m)/2 \qquad \text{for even } (M-m) \tag{67}$$

The first sample of the global reflection coefficient is contaminated by an undesired non-causal noise, originating from the postcritical reflection from deeper layers. This non-causal effect is not suprising. It is a consequence of the formulation. The incident plane wave has been propagating for an infinite time before passing the origin of the coordinates at our chosen time origin $t = 0$. For postcritical incidence the evanescent wave travels faster horizontally than the propagating wave and therefore creates a scattered field before the incident wave arrives.

This shows that the forward recursion process produces an impulse response of the geology containing a non-causal element for postcritical incidence only. As a result of this, there can be no inverse recursion which uses the concept of causality to reconstruct the acoustic layer parameters.

6. Numerical results

In accordance with the theory, a forward program and an inverse program were developed. Discretized versions of both recursion formulae were used, of course, with a time sampling interval of two milliseconds and a total of 4096 sampling elements.

The programs were implemented on a Gould 32/67 computer equipped with a 32-bit CPU with high-speed transistor-to-transistor logic (TTL), operating at 150 nanoseconds machine cycle time. The CPU time used by the forward program of course depends heavily on the number of layers in the geological model, as this determines the number of recursion steps. The inverse program uses 2,629 seconds CPU time for 2048 recursion steps.

Figure 4(a) shows an acoustic impedance profile of a structure containing

4. ábra. A 684 réteges modell
(a) akusztikus impedancia szelvény; (b) szintetikus szeizmogram merőleges beesésre az 5. ábrán látható elemi hullámmal; (c) az inverzió eredménye zaj nélkül, maximális frekvencia 250 Hz; (d) az inverzió eredménye 2% fehér zaj hozzáadása után, maximális frekvencia 125 Hz

Рис. 4. Геологическая модель с 684 слоями:
(a) профиль акустического импеданса; (b) синтетическая сейсмограмма при прямом вхождении для вавелета рис. 5; (c) результат обращения, без шума, максимальная частота – 250 гц; (d) результат обращения после добавления 2% белого шума, максимальная частота – 125 гц.

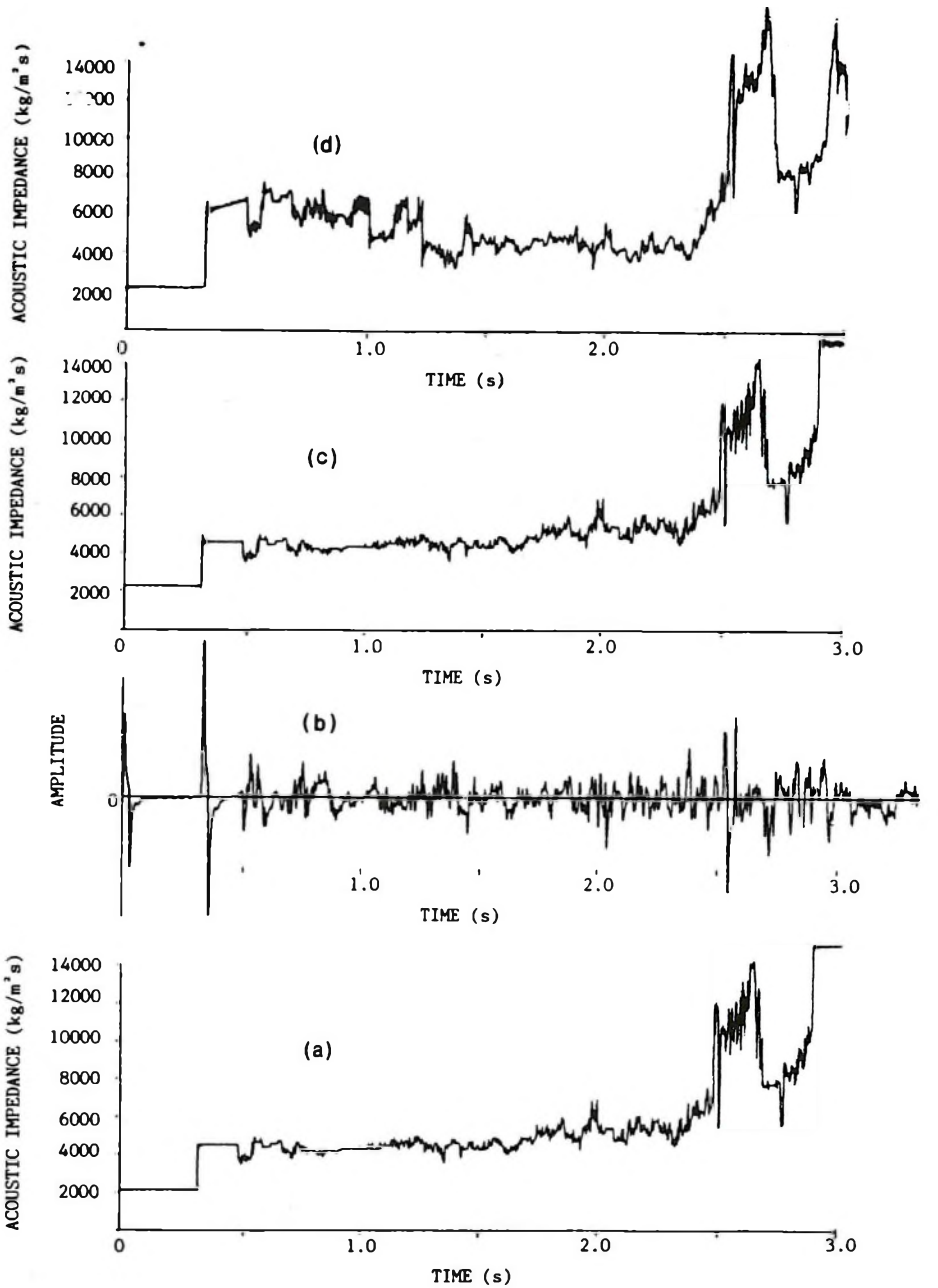

Fig. 4. The model of 684 layers
(a) acoustic impedance profile; (b) synthetic seismogram for normal incidence with the wavelet shown in Fig. 5; (c) inversion result, no noise, maximum frequency 250 Hz; (d) inversion result after adding 2% white noise, maximum frequency 125 Hz

684 layers. This geological model is based on real data taken from a North Sea oil well. The upper half-space consists of sea water. A synthetic wavelet *(Fig. 5)* was used to calculate a seismic response for normal incidence, shown in *Fig. 4(b)*. The result of the inversion algorithm is demonstrated in *Fig. 4(c)*. Clearly, it yields a perfect reconstruction of the whole subsurface sequence, from the 'sea bottom' down to the lower half-space. It should be remembered that the complete inversion scheme entails two recursive processes. First the local reflection coefficients are recovered through the inversion, using the layer peeling and multiple removing algorithm illustrated by Fig. 3; secondly, the acoustic impedance (or admittance) profile is derived using equation (48).

For all precritical angles an excellent result was obtained: an exact reconstruction of the vertical acoustic impedance component, based on a two-way travel time scale.

As a first step towards reality, the sensitivity of the algorithm to noise was tested. *Figure 4(d)* shows the result of the algorithm after adding white noise to the signal shown in Fig. 4b, at a noise-to-signal ratio of two per cent (r.m.s.). In order to obtain a stable solution, the frequency bandwidth had to be cut by half: only frequencies up to 125 Hz instead of 250 Hz were included in the inversion scheme. Apparently, at higher frequencies the information bearing content of the reflected signal has been flooded by the noise content; an effect enhanced by the deconvolution process as expressed by formulae (39) and (40).

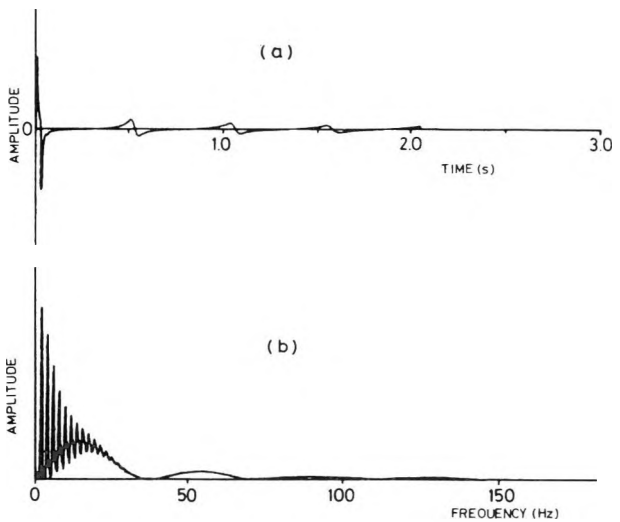

Fig. 5. Synthetic wavelet in time- (a) and frequency (b) domain

5. ábra. Szintetikus elemi hullám az idő- (a) és a frekvencia- (b) tartományban

Рис. 5. Синтетический вавелет: (a) временная область; (b) частотная область.

It can be seen in Fig. 4(d) that the shape of the impedance profile is recovered more or less correctly. Most strikingly, individual reflections are identified at the correct two-way travel times, hence layer interfaces are put at the right place throughout the structure. The magnitude of the identified reflection coefficients contains an error—as can be expected—which, in its turn, causes an overall deviation in the reconstructed impedance profile. This becomes clear especially at relatively sharp contrasts. Sometimes minor contrasts are exaggerated and smooth layers acquire an irregular appearance; this is most noticeable at the lower half-space where the global reflection coefficient should have been zero for all frequencies. However, as stated before, the error in the local reflection coefficients never destabilizes the inverse layer peeling and multiple removing algorithm, as long as 'unreliable' frequencies are excluded from the inversion process.

Finally, the ultimate limits to the noise endurance of the algorithm were explored. An extremely simple synthetic geology *(Fig. 6(a))* was scanned with a minimum phase wavelet shown in *Fig. 7*, which has a more broad-band and more regular spectrum than the synthetic wavelet used previously.

Figure 6(b) shows the resulting reflected wave with a noise-to signal ratio of 30 per cent. *Figure 6(c)* shows the recovered reflection coefficients, using frequencies up to 75 Hertz only. All reflections are still identified at exactly the correct two-way travel times. The layer peeling and multiple removing algorithm has remained stable, but the quantitative error in the magnitude of the recovered reflection coefficients is such that the recursive process of reconstructing the impedance profile does not at first produce a sensible result. However, if a threshold value is implemented to select only those reflection coefficients which exceed the expected noise level, an impedance profile is obtained which gives a reasonable estimate of at least the shape of the subsurface *(Fig. 6(d))*.

The inversion process becomes unstable if either the noise level or the bandwidth is increased. Thus the resolution of the inversion process depends on the bandwidth for which there is an adequate signal-to-noise ratio.

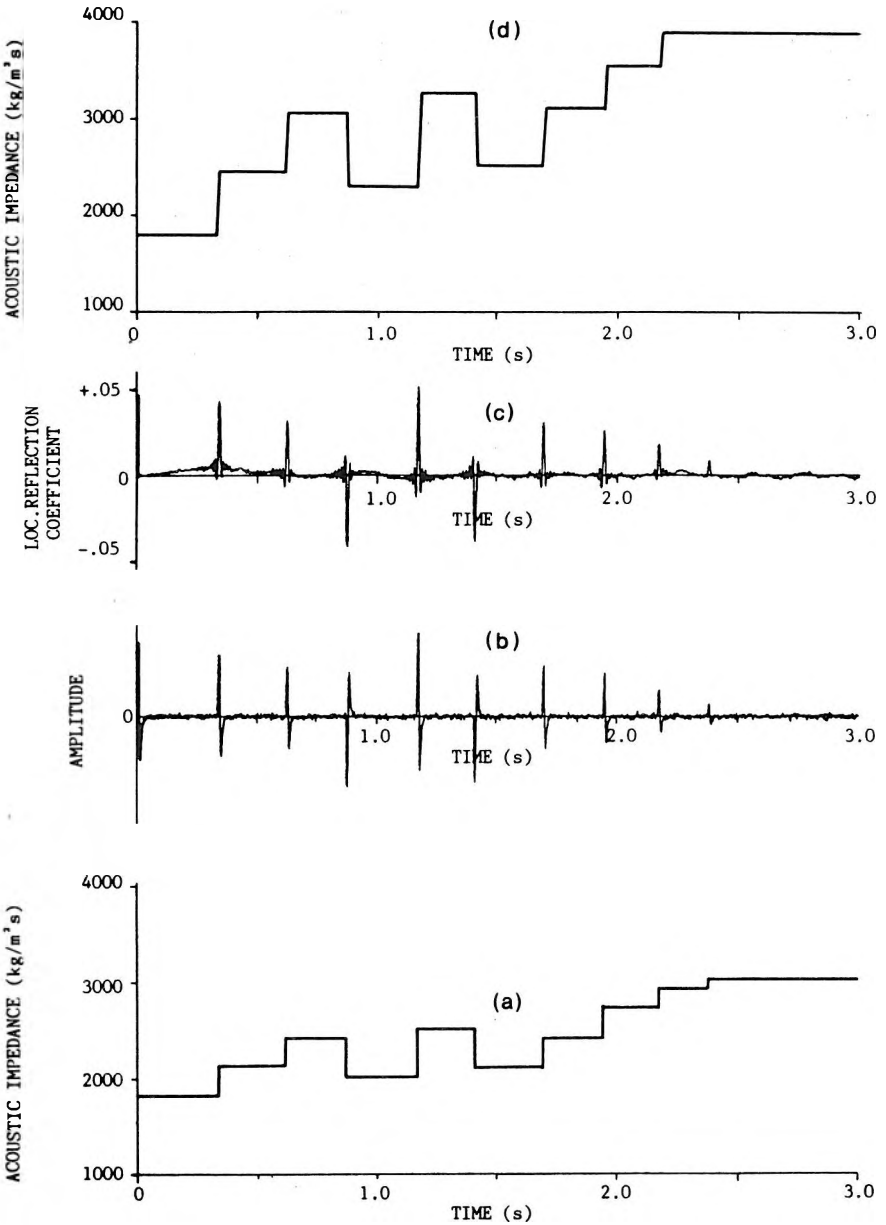

Fig. 6. Simple geological model
(a) acoustic impedance profile; (b) synthetic seismogram for normal incidence with the wavelet shown in Fig. 7, 30% white noise added; (c) recovered reflection coefficients, maximum frequency 75 Hz; (d) reconstruction of the acoustic impedance profile after applying a 30% threshold filter

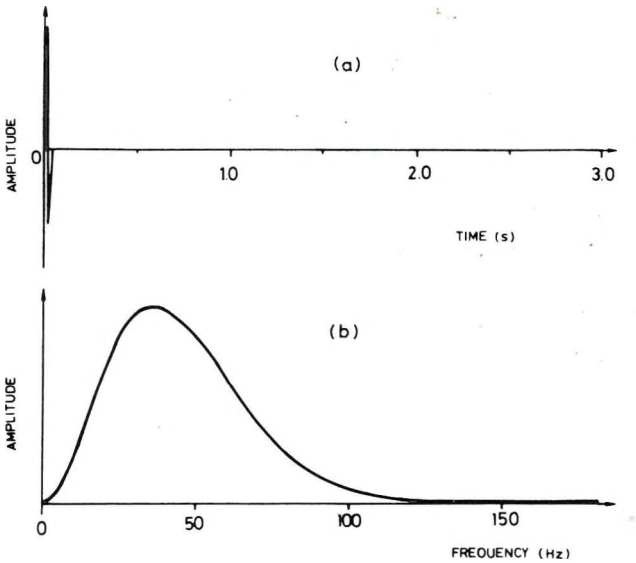

Fig. 7. Minimum phase wavelet in time- (a) and frequency (b) domain

7. ábra. Minimum fázisú elemi hullám az idő- (a) és frekvencia- (b) tartományban

Рис. 7. Вавелет в фазе минимума: (a) временная область; (b) частотная область.

6. ábra. Egyszerű földtani modell
(a) akusztikus impedancia szelvény; (b) szintetikus szeizmogram merőleges beesés mellett a 7. ábrán látható elemi hullámmal, 30% fehér zaj esetén; (c) az inverzióval visszanyert reflexiós együttható sorozat, maximális frekvencia 75 Hz; (d) az akusztikus impedancia szelvény rekonstrukciója, 30% küszöbszűrőt alkalmazva

Рис. 6. Простоя геологическая модель:
(a) профиль акустического импеданса; (b) сигнал отраженной волны при прямом вхождении для вавелета рис. 7, 30% белого шума; (c) полученные путем инверсии коэффиенты отражений, максимальная частота – 75 гц; (d) воссоздание профиля акустического импеданса с использованием порогового фильтра 30%.

7. Conclusions

Using acoustic wave theory, a frequency based recursion scheme has been developed to calculate the reflected wave signal of a horizontally leyered structure for plane wave incidence. By inverting this recursion algorithm and using the causality principle, a layer peeling and multiple removing algorithm has been derived, which recovers the layer structure from the reflected wave.

In the case of postcritical incidence the reflected wave contains a non-causal component; an inversion algorithm using the concept of causality cannot be developed.

For any precritical angle of incidence the inversion algorithm yields excellent results on noise-free synthetic reflected field signals.

Tests show that the inverse algorithm remains stable when the reflected signal is contaminated with white noise, although parts of the frequency domain where the signal-to-noise ratio is small must be left out of the algorithm. Qualitatively, the recursion performs well and the reflection coefficients are identified at the correct two-way travel times. However, the recovered reflection coefficients contain a quantitative error which at very high noise levels necessitates the use of a threshold filter, in order to obtain a faithful acoustic impedance or admittance profile.

Acknowledgements

The authors wish to thank the Management Office for Energy Research (PEO), Utrecht, the Netherlands, for financially supporting the research presented in this article.

REFERENCES

BRUCKSTEIN A., LEVY B. C. and KAILATH T. 1983: Differential methods in inverse scattering. Tech. Rep. Information Systems Lab., Stanford Univ.

CLAERBOUT J. F. 1976: Fundamentals of geophysical data processing. McGraw Hill, New York, 274 p.

GOUPILLAUD P. 1961: An approach to inverse filtering of near surface layer effects from seismic records. Geophysics, **26**, 6, pp. 754–760

KENNETT B. L. N. 1985: Seismic wave propagation in stratified media. Cambridge Univ. Press, 342 p.

ROBINSON E. A. 1982: Spectral approach to geophysical inversion by Lorentz, Fourier and Radon transforms. Proc. IEEE, **70**, 9, pp. 1039–1054

ROBINSON E. A. and TREITEL S. 1980: Geophysical signal analysis. Prentice-Hall Inc., Englewood Cliffs, New York, 466 p.

SCHUR I. 1917: Über Potenzreihen, die im Innern des Einheitskreises beschränkt sind. J. für die reine und angewandte Mathematik, **147**, pp. 205–232

TREITEL S., GUTOWSKI P. R. and WAGNER D. E. 1982: Plane-wave decomposition of seismograms. Geophysics, **47**, 10, pp. 1375–1401

YAGLE A. E. and LEVY B. C. 1984: The Schur algorithm and its applications. Tech. Rep. Lab. for Information and Decision Systems and the Dept. of Electrical Engineering and Computer Science, Mass. Inst. of Tech.

INVERZ SZÓRÁSI ALGORITMUS SÍKHULLÁM BEESÉSRE, EGYDIMENZIÓS INHOMOGÉN AKUSZTIKUS KÖZEGBEN

Frederic B. LEYDS és Jacob T. FOKKEMA

Vízszintesen rétegzett akusztikus féltérre beeső, síkhullámból keletkező reflektált akusztikus jel számítására kifejlesztettünk egy, a frekvencián alapuló algoritmust. Ezt a modellező algoritmust invertáltuk, hogy egy réteglefejtő algoritmust kapjunk, amellyel minden rétegben meg tudjuk határozni az akusztikus impedancia értéket, az okság elvének alkalmazásával. A kritikusnál nagyobb beesési szögnél az inverz algoritmus kidolgozása lehetetlen, mert a lecsengő hullámok a vízszintesen rétegzett féltérben egy nem-oksági taggal járulnak hozzá a szórt térhez.

A direkt és inverz algoritmust valódi karotázs adatokon alapuló bonyolult szerkezeten ellenőriztük. A szintetikus jelek inverziója kiváló eredményeket ad. Kísérletek mutatják, hogy az inverz algoritmus a fehér zajra érzékeny. Csak akkor marad stabil, ha a szórt térnek azon frekvenciáját használjuk, amelynél a beeső tér amplitúdója láthatóan meghaladja a zaj amplitúdóját. A sávszélességnek ezzel a csökkentésével 684 rétegű modell impedancia szelvényét lehet elkészíteni 2% (r. m. s.) zaj/jel viszony esetén. Nyolc rétegű egyszerű felépítés 30% zaj/jel arányig rekonstruálható, de csak abban az esetben, ha a zaj tartományába eső reflexiós együtthatókat eltávolítjuk egy küszöb szűrővel, mielőtt az akusztikus impedancia szelvényt levezetnénk.

АЛЬГОРИТМ ОБРАТНОЙ ДИСПЕРСИИ, ДИСКРЕТНОЙ ВО ВРЕМЕНИ, ДЛЯ ВХОЖДЕНИЯ ПЛОСКОЙ ВОЛНЫ, В ОДНОМЕРНОЙ НЕОДНОРОДНОЙ АКУСТИЧЕСКОЙ СРЕДЕ

Ф. Б. ЛЕЙДС и Дж. Т. ФОКЕМА

Разработан альгоритм на базе частот для расчета отраженного акустического сигнала, возникающего из плоской волны, входящей в горизонтально слоистое акустическое полупространство. Данный альгоритм, осуществляющий моделирование во времени, был обращен с целью получения альгоритма снятия слоев для получения значений акустического импеданса по всем слоям путем применения принципа причинности. При угле вхождения больше критического разработка обращенного альгоритма невозможно, ибо затухающие волны в дисперсном поле образуют непричинный член в горизонтально слоистой среде.

Прямой и обращенный альгоритмы проверялись на каротажных данных, полученных в сложных геологических условиях. Обращение искусственных сигналов обеспечивает отличные результаты. Экспериментами учтановлено, что обращенный альгоритм чувствителен к белому шуму, оставаясь стабильным лишь в том случае, если используются те частоты дисперсного поля, на которых амплитуда входящего поля явно превышает амплитуду шума. Подобным уменьшением ширины полосы можно составить профиль импеганса могели с 684 геологическими слоями при 2%-ном соотношении шум: сигнал (r. m. s.). Простая геологическая модель с восемью слоями может быть воссоздана вплоть до 30%-ного соотношения шум: сигнал, но лишь в том случае, если вскрытые коэффициенты отпажения в диапазоне шума удаляются пороговым фильтром еще до вывода профиля акустического импеданса.

GEOPHYSICAL TRANSACTIONS 1987
Vol. 33. No. 2. pp. 89–111

REFLECTION AND TRANSMISSION OF SH-WAVES IN LATERALLY AND VERTICALLY HETEROGENEOUS MEDIA AT AN IRREGULAR BOUNDARY

Suversha GUPTA*

Reflection and transmission coefficients of plane SH-waves at a corrugated interface between two laterally and vertically heterogeneous media have been studied by using Rayleigh's method of approximation. Effects of lateral and vertical variation constants, amplitude of the corrugated boundary, wavelength of the irregular interface and velocity contrast were considered numerically and graphically for the normal incidence case, for the first order approximation.

Keywords: reflection coefficient, transmission coefficient, SH-waves, Rayleigh's approximation, heterogeneous media, corrugated boundary

1. Introduction

Waves are generally affected by discontinuities between media. Wave conversion and phase change take place upon reflection and refraction at plane interfaces. Studies of these modifications in the propagation of various kinds of waves upon reflection and transmission at plane interfaces have been made extensively. Since earthquake generated seismic waves encounter in their paths mountain basins and mountain roots, such irregularities do affect the reflection and transmission of elastic waves through the media. Thus the study of the dynamic characteristics of waves reflected and refracted by rough surfaces is of great practical importance.

The study of the problems of reflection and refraction of waves incident upon an irregular boundary, initiated by RAYLEIGH [1893, 1896, 1907] for sound and light waves, has given rise to a rich literature in other fields also. Since these types of problems involve considerable mathematical difficulty, the exact solutions of the problem have not yet been found. In recent years, a number of approximate methods for computing the field produced by scattering at an irregular surface have been developed. These more general treatments include work by BREKHOVSKIKH [1951], ECKART [1953], MILES [1954], PARKAR [1956, 1957], TWERSKY [1957], LYSANOV [1958], ABUBAKAR [1962], HERRARA [1964], HERRARA and MAL [1965], SLAVIN and WOLF [1970]. In the study of elastic waves in solids, HOMMA [1941] seems to have been the first to make an attempt to solve the problem of reflection of body waves at a corrugated traction-free

* Department of Mathematics, Lincoln University, PA 19352-0999, U.S.A.
Manuscript received: 10 February, 1987

surface, by reducing it to the problem of a plane surface. A similar attempt was made by GILBERT and KNOPOFF [1960]. SATO [1955] also considered the reflection of elastic waves at a corrugated, free surface by using the method that was first applied to acoustic and optical gratings by RAYLEIGH [1907]. ASANO [1960, 1961, 1966] used Rayleigh's method of approximation to solve reflection and refraction of elastic waves at a corrugated interface.

The reflection of body waves from an arbitrary, not necessarily periodic, rough surface of a semi-infinite solid was discussed by ABUBAKAR [1962a, 1962b], and by DUNKIN and ERINGEN [1962], each of whom applied a perturbation technique to arrive at the result. ABUBAKAR [1962c] devoted another paper to working out the particular case of a flat boundary having a local depression, while DUNKIN and ERINGEN also dealt with the diffraction of Rayleigh surface waves by a wavy boundary – a problem analysed earlier by BREKHOVSKIKH [1959]. ADAMS and CHUNG-PO CHANG [1964] investigated the wave propagation phenomenon at an irregular infinite interface by applying the Weber integral solution to the wave equation. DERESIEWICZ and WOLF [1964] studied the reflected field arising from body waves incident on a rough boundary of a saturated porous medium. LEVY and DERESIEWICZ [1967] investigated the reflection and transmission of elastic waves in a system of corrugated layers. WOLF [1967, 1970] studied the propagation of Love waves in surface layers of varying thicknesses and the propagation of Love waves in layers with irregular boundaries. SLAVIN and WOLF [1970] investigated the scattering of Love waves in a surface layer with an irregular boundary for a rigid underlying half-space. SUMNER and DERESIEWICZ [1972] investigated the effect of surface irregularity on the propagation of waves in an isotropic elastic plate by employing the perturbation technique. YAMADA and SATO [1976] studied SH-wave propagation in a medium having a step-shaped discontinuity. GUPTA [1978] studied the reflection and refraction from curved interfaces.

In all the above investigations, the media considered were homogeneous and isotropic. Very little work has been done on inhomogeneous media with an irregular boundary. CHATTOPADHYAY and PAL [1982] studied the propagation of SH-waves in an inhomogeneous medium with an irregular interface overlying an initially stressed elastic half-space. ITS and YANOVSKAYA [1985] studied the propagation of surface waves in a half-space with near-vertical curved interfaces. Here, we have made an attempt to study the reflection and transmission of plane SH-waves at a corrugated interface between two laterally and vertically heterogeneous media. Rayleigh's method of approximation has been followed to find expressions for reflection and transmission coefficients for the first and second order approximations. The effect of lateral and vertical variation constants, amplitude of the corrugated boundary, wavelength of the irregular interface and velocity contrast have been considered numerically and graphically for the normal incidence case, for the first order approximation.

2. Formulation of the problem

The geometry of the problem under consideration is shown in *Figure 1*; M_1 and M_2 are two laterally and vertically inhomogeneous half-spaces, separated by an irregular boundary. The x- and y-axes are on the horizontal surface and the z-axis is taken positive vertically downwards. The equation of the boundary surface is assumed to be $z=\zeta$, where ζ is a periodic function of x and is independent of y, the mean value of which is zero. Then ζ can be represented by a Fourier series as follows:

$$\zeta = \sum_{n=1}^{\infty} (\zeta_n e^{inpx} + \zeta_{-n} e^{-inpx}), \tag{1}$$

$$\zeta = c_1 \cos px + c_2 \cos 2px + s_2 \sin 2px + c_3 \cos 3px + s_3 \sin 3px + \ldots + \\ + c_n \cos npx + s_n \sin npx + \ldots, \tag{2}$$

where

$$\zeta_1 = \zeta_{-1} = c_1/2 \tag{3}$$

and

$$\zeta_{\pm n} = (c_n \mp i s_n)/2. \tag{4}$$

When the boundary surface is expressible by only one cosine term, i.e. $\zeta = c_1 \cos px$, the wavelength of the corrugation is $2\pi/p$.

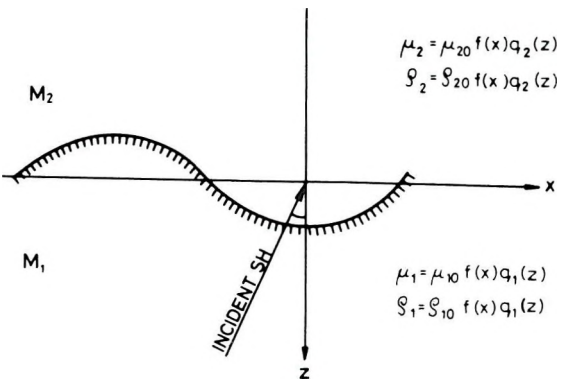

Fig. 1. Geometry of the problem

1. ábra. A feladat geometriája

Рис. 1. Геометрические условия задачи.

We consider the case when the plane SH-wave with period $2\pi/\omega$ is incident from the lower to the upper half-space, making an angle Θ with the z-axis. The quantities concerning the lower medium will be denoted by suffix 1 and those of the upper medium by suffix 2. Let ϱ_j be the density and μ_j the rigidity in M_j (medium: $j = 1, 2$) and:

$$\begin{aligned} \varrho_j(x, z) &= \varrho_{j0} f(x)\, q_j(z), \\ \mu_j(x, z) &= \mu_{j0} f(x)\, q_j(z) \end{aligned} \tag{5}$$

where ϱ_{j0} and μ_{j0} are constants. We also assume that $f(x)$ and $q_j(z)$ satisfy the equations:

$$\begin{aligned} \frac{1}{2}\frac{f''(x)}{f(x)} - \frac{1}{4}\left[\frac{f'(x)}{f(x)}\right]^2 &= a_0^2 \\ \frac{1}{2}\frac{q_j''(z)}{q_j(z)} - \frac{1}{4}\left[\frac{q_j'(z)}{q_j(z)}\right]^2 &= b_j^2 \quad \text{for } j = 1 \text{ and } 2 \end{aligned} \tag{6}$$

where a_0^2, b_j^2 are constants. Functional forms of the solutions are of the type exp (ax), $(1 + ax)^2$, $\sinh^2(ax)$, $\cosh^2(ax)$ (7)

If the boundary surface is a plane, then we have the following solutions [MALHOTRA et al. 1982]:

Incident wave

$$v_0 = \frac{1}{[\mu_{10} f(x)\, q_1(z)]^{1/2}} \exp\left[i\omega(t - x \sin\Theta/\beta_1) - i\, sz\right] \tag{8}$$

Reflected wave

$$v_1 = \frac{1}{[\mu_{10} f(x)\, q_1(z)]^{1/2}} R_0 \exp\left[i\omega(t - x \sin\Theta/\beta_1) + i\, sz\right], \tag{9}$$

Refracted wave

$$v_2 = \frac{1}{[\mu_{20} f(x)\, q_2(z)]^{1/2}} T_0 \exp\left[i\omega(t - x \sin\delta/\beta_2) - irz\right], \tag{10}$$

where

$$\beta_j^2 = \mu_{j0}/\varrho_{j0},\ k_{\beta_j} = \omega/\beta_j \tag{11}$$

s and r are given by:

$$s = \begin{cases} [k_{\beta_1}^2 \cos^2\Theta - a_0^2 - b_1^2]^{1/2} & \text{for} \quad k_{\beta_1}\cos\Theta > (a_0^2 + b_1^2)^{1/2} \\ -i[a_0^2 + b_1^2 - k_{\beta_1}^2 \cos^2\Theta]^{1/2} & \text{for} \quad k_{\beta_1}\cos\Theta < (a_0^2 + b_1^2)^{1/2}, \end{cases} \tag{12}$$

$$r = \begin{cases} [k_{\beta_2}^2 \cos^2\delta - a_0^2 - b_2^2]^{1/2} & \text{for} \quad k_{\beta_2}\cos\delta > (a_0^2 + b_2^2)^{1/2} \\ -i[a_0^2 + b_2^2 - k_{\beta_2}^2 \cos^2\delta]^{1/2} & \text{for} \quad k_{\beta_2}\cos\delta < (a_0^2 + b_2^2)^{1/2}, \end{cases} \tag{13}$$

δ being the angle which the refracted wave makes with the z-axis and connected with the incidence angle θ, by Snell's law.

$$\frac{\sin \Theta}{\beta_1} = \frac{\sin \delta}{\beta_2} = \frac{k}{\omega} \tag{14}$$

k being the wavenumber.

In addition to the incident and regularly reflected and regularly refracted waves, we have to consider the effect of corrugation on the reflection and refraction of SH-waves. For irregularly reflected waves, whose spectrum of the nth order is:

$$v_1' = \frac{1}{[\mu_{10} f(x) q_1(z)]^{1/2}} \Big[R_n \exp [i\omega(t - x \sin \Theta_n/\beta_1) + is_n z] + R_n' \exp [i\omega(t - x \sin \Theta_n'/\beta_1) + is_n' z] \Big], \tag{15}$$

where, by the elementary theory of these spectra [ABUBAKAR 1962],

$$\sin \Theta_n - \sin \Theta = \pm |np|/k_{\beta_1} \tag{16}$$

and

$$s_n = \begin{cases} [k_{\beta_1}^2 \cos^2 \Theta_n - (a_0^2 + b_1^2)]^{1/2} & \text{for} \quad k_{\beta_1} \cos \Theta_n > (a_0^2 + b_1^2)^{1/2} \\ -i[(a_0^2 + b_1^2) - k_{\beta_1}^2 \cos^2 \Theta_n]^{1/2} & \text{for} \quad k_{\beta_1} \cos \Theta_n < (a_0^2 + b_1^2)^{1/2}, \end{cases}$$

$$s_n' = \begin{cases} [k_{\beta_1}^2 \cos^2 \Theta_n' - (a_0^2 + b_1^2)]^{1/2} & \text{for} \quad k_{\beta_1} \cos \Theta_n' < (a_0^2 + b_1^2)^{1/2} \\ -i[(a_0^2 + b_1^2) - k_{\beta_1}^2 \cos^2 \Theta_n']^{1/2} & \text{for} \quad k_{\beta_1} \cos \Theta_n' < (a_0^2 + b_1^2)^{1/2}, \end{cases} \tag{17}$$

where Θ_n, Θ_n' are the angles which the irregularly reflected waves make with the z-axis. In equation (16), we shall choose the upper sign (positive) for Θ_n and the lower sign (negative) for Θ_n'. Thus the complete expression of the displacement V_1 in the lower medium takes the form:

$$V_1 = \frac{1}{[\mu_{10} f(x) q_1(z)]^{1/2}} \exp [i\omega(t - x \sin \Theta/\beta_1)] [e^{-isz} + R_0 e^{isz} + \sum R_n e^{-inpx} e^{is_n z} + \sum R_n' e^{inpx} e^{is_n' z}]. \tag{18}$$

Similarly, in the upper medium the spectrum of the nth order is represented by:

$$v_2' = \frac{1}{[\mu_{20} f(x) q_2(z)]^{1/2}} \Big[T_n \exp [i\omega(t - x \sin \delta_n/\beta_2) - ir_n z] + T_n' \exp [i\omega(t - x \sin \delta_n'/\beta_2) + ir_n' z] \Big], \tag{19}$$

where δ_n, δ_n' are the angles which the irregularly refracted waves make with the z-axis and are connected by the relation:

$$\sin \delta_n - \sin \delta = +|np|/k_{\beta_2}, \qquad \sin \delta_n' - \sin \delta = -|np|/k_{\beta_2} \tag{20}$$

and

$$r_n = \begin{cases} [k_{\beta_2}^2 \cos^2 \delta_n - (a_0^2 + b_2^2)]^{1/2} & \text{for} \quad k_{\beta_2} \cos \delta_n > (a_0^2 + b_2^2)^{1/2} \\ -\mathrm{i}[a_0^2 + b_2^2 - k_{\beta_2}^2 \cos^2 \delta_n]^{1/2} & \text{for} \quad k_{\beta_2} \cos \delta_n < (a_0^2 + b_2^2)^{1/2}, \end{cases}$$

$$r_n' = \begin{cases} [k_{\beta_2}^2 \cos^2 \delta_n' - (a_0^2 + b_2^2)]^{1/2} & \text{for} \quad k_{\beta_2} \cos \delta_n' > (a_0^2 + b_2^2)^{1/2} \\ -\mathrm{i}[(a_0^2 + b_2^2) - k_{\beta_2}^2 \cos^2 \delta_n']^{1/2} & \text{for} \quad k_{\beta_2} \cos \delta_n' < (a_0^2 + b_2^2)^{1/2}, \end{cases} \tag{21}$$

Hence the complete displacement V_2 in the upper medium takes the form:

$$V_2 = \frac{1}{[\mu_{20} f(x) q_2(z)]^{1/2}} \exp[\mathrm{i}\omega(t - x \sin \delta/\beta_2)] [T_0 \mathrm{e}^{-\mathrm{i}rz} + \\ + \sum T_n \mathrm{e}^{-\mathrm{i}npx} \mathrm{e}^{-\mathrm{i}r_n z} + \sum T_n' \mathrm{e}^{\mathrm{i}npx} \mathrm{e}^{-\mathrm{i}r_n' z}]. \tag{22}$$

3. Boundary conditions

The conditions to be satisfied at the boundary are:

(i) The displacement should be continuous at the interface, i.e.

$$V_1 = V_2 \quad \text{at } z = \zeta. \tag{23}$$

(ii) The tangential stress should be continouous at the interface, i.e.

$$\mu_1 \left[\frac{\partial v_1}{\partial z} - \frac{\partial v_1}{\partial x} \zeta'\right] \frac{1}{\sqrt{1 + \zeta'^2}} = \mu_2 \left[\frac{\partial v_2}{\partial z} - \frac{\partial v_2}{\partial x} \zeta'\right] \frac{1}{\sqrt{1 + \zeta'^2}},$$

$$\mu_{10} q_1(z) \left[\frac{\partial v_1}{\partial z} - \frac{\partial v_1}{\partial x} \zeta'\right] = \mu_{20} q_2(z) \left[\frac{\partial v_2}{\partial z} - \frac{\partial v_2}{\partial x} \zeta'\right]. \tag{24}$$

The boundary conditions (23) and (24) yield:

$$[q_2(z)]_{z=\zeta}^{1/2} [\mathrm{e}^{-\mathrm{i}s\zeta} + R_0 \mathrm{e}^{\mathrm{i}s\zeta} + \sum R_n \mathrm{e}^{-\mathrm{i}npx} \mathrm{e}^{\mathrm{i}s_n\zeta} + \sum R_n' \mathrm{e}^{\mathrm{i}npx} \mathrm{e}^{\mathrm{i}s_n'\zeta}] =$$

$$= \sqrt{m}\, [q_1(z)]_{z=\zeta}^{1/2} [T_0 e^{-\mathrm{i}r\zeta} + \sum T_n \mathrm{e}^{-\mathrm{i}npx} \mathrm{e}^{-\mathrm{i}r_n\zeta} + \sum T_n' \mathrm{e}^{\mathrm{i}npx} \mathrm{e}^{-\mathrm{i}r_n'}], \tag{25}$$

$$\sqrt{m'}\, [q_1(z)]_{z=\zeta}^{1/2} \left\{ \left[-\frac{1}{2} \left(\frac{q_1'}{q_1}\right)_{z=\zeta} - \mathrm{i}s\zeta + \left(\frac{1}{2} \frac{f'}{f} + \mathrm{i}k_{\beta_1} \sin \Theta\right) \zeta' \right] \right.$$

$$\mathrm{e}^{-\mathrm{i}s\zeta} + R_0 \left[\mathrm{i}s - \frac{1}{2} \left(\frac{q_1'}{q_1}\right)_{z=\zeta} + \left(\frac{1}{2} \frac{f'}{f} + \mathrm{i}k_{\beta_1} \sin \Theta\right) \zeta' \right] \mathrm{e}^{\mathrm{i}s\zeta} +$$

$$+ \sum R_n \mathrm{e}^{-\mathrm{i}npx} \left[\mathrm{i}s_n\zeta - \frac{1}{2} \left(\frac{q_1'}{q_1}\right)_{z=\zeta} + \left(\mathrm{i}np + \frac{1}{2} \frac{f'}{f} + \mathrm{i}k_{\beta_1} \sin \Theta\right) \zeta \right] \mathrm{e}^{\mathrm{i}s_n\zeta} +$$

$$\left. + \sum R_n \mathrm{e}^{\mathrm{i}npx} \left[\mathrm{i}s_n'\zeta - \frac{1}{2} \left(\frac{q_1'}{q_1}\right)_{z=\zeta} + \left(-\mathrm{i}np + \frac{1}{2} \frac{f'}{f} + \mathrm{i}k_{\beta_1} \sin \Theta\right) \zeta' \right] \mathrm{e}^{\mathrm{i}s_n'\zeta} \right\} = \tag{26}$$

$$= [q_2(z)]_{z=\zeta}^{1/2} \left\{ T_0 \left[-ir\zeta - \frac{1}{2}\left(\frac{q_2'}{q_2}\right)_{z=\zeta} + \left(\frac{1}{2}\frac{f'}{f} + ik_{\beta_2}\sin\delta\right)\zeta' \right] e^{-ir\zeta} + \right.$$
$$+ \sum T_n e^{inpx} \left[-ir_n\zeta - \frac{1}{2}\left(\frac{q_2'}{q_2}\right)_{z=\zeta} + \left(inp + \frac{1}{2}\frac{f'}{f} + ik_{\beta_2}\sin\delta\right)\zeta' \right] e^{-ir_n\zeta} +$$
$$\left. \sum T_n' e^{inpx} \left[-ir_n'\zeta - \frac{1}{2}\left(\frac{q_2'}{q_2}\right)_{z=\zeta} + \zeta' \left(-inp + \frac{1}{2}\frac{f'}{f} + \right.\right.\right.$$
$$\left.\left.\left. + ik_{\beta_2}\sin\delta \right) \right] e^{-ir_n'\zeta} \right\},$$

where $m = \mu_{10}/\mu_{20}$.

4. Approximate solutions

To find the approximate solutions, we assume that the functions $f(x)$ and $q_j(z)$ are in the exponential form:

$$\begin{aligned} f(x) &= \exp(\alpha x), \\ q_j(z) &= \exp(\gamma_j z), \quad j = 1, 2. \end{aligned} \tag{27}$$

We also assume that the amplitude of the corrugation and the slope of the corrugated interface are both small. By an iteration procedure, the approximations are advanced. For first order approximation, the terms independent of x and ζ are retained in (25) and (26) to determine the first approximation of R_0 and T_0. By making use of (27), we get:

$$1 + R_0 = \sqrt{m}\, T_0, \tag{28}$$

$$\left(-\frac{\gamma_1}{2} - is \right) + R_0 \left(-\frac{\gamma_1}{2} + is \right) = \frac{1}{\sqrt{m}} \left(ir - \frac{\gamma_2}{2} \right) T_0. \tag{29}$$

These two equations, (28) and (29), give the amplitudes of the reflected and refracted waves for a plane boundary surface. From these two equations, R_0 and T_0 are obtained as follows:

$$R_0 = \frac{m\left(\frac{\gamma_1}{2} + is\right) - \left(ir + \frac{\gamma_2}{2}\right)}{m\left(is - \frac{\gamma_1}{2}\right) + \left(ir + \frac{\gamma_2}{2}\right)}, \tag{30}$$

$$T_0 = \frac{2is\sqrt{m}}{m\left(is - \frac{\gamma_1}{2}\right) + \left(ir + \frac{\gamma_2}{2}\right)} \tag{31}$$

After further simplification, expressions (30) and (31) coincide with the results of SINGH et al. [1978].

In order to obtain the first order approximation of R_n and T_n, the coefficients of e^{-inpx} on each side of the boundary conditions (25) and (26) are equated. By carrying out this procedure, the following formulae for the first approximation of R_n and T_n are obtained:

$$R_n - \sqrt{m}\, T_n = \sqrt{m}\left(\frac{\gamma_1}{2} - ir\right) T_0\, \zeta_{-n} + is(1 - R_0)\, \zeta_{-n} - \frac{\gamma_2}{2}(1 + R_0)\, \zeta_{-n}, \tag{32}$$

$$\left(is_n - \frac{\gamma_1}{2}\right) R_n + \frac{1}{\sqrt{m}}(ir_n + \gamma_2/2)\, T_n =$$

$$= \left[s^2 + \frac{\gamma_1^2}{4} + inp\left(\frac{\alpha}{2} + ik_{\beta_1} \sin \Theta\right)\right]\left[1 + R_0\right] \zeta_{-n} - \frac{1}{\sqrt{m}}$$

$$\left[r^2 + \frac{\gamma_2^2}{4} + inp\left(\frac{\alpha}{2} + ik_{\beta_2} \sin \delta\right) T_0\right] \zeta_{-n}. \tag{33}$$

Similarly equating the coefficients of e^{inpx} in the boundary conditions (23) and (24), by making use of (25), we obtain the first approximation of R_n' and T_n' as follows:

$$R_n' - \sqrt{m}\, T_n' = \sqrt{m}\left(\frac{\gamma_1}{2} - ir\right) \zeta_n T_0 + is(1 - R_0)\, \zeta_n - \frac{\gamma_2}{2}(1 - R_0)\, \zeta_{-n}, \tag{34}$$

$$R_n'\left(is_n' - \frac{\gamma_1}{2}\right) + \frac{1}{\sqrt{m}}\left(ir_n' + \frac{\gamma_2}{2}\right) T_n' = \left[s^2 + \frac{\gamma_1^2}{4} - inp\left(\frac{a}{2} +\right.\right.$$

$$\left.\left. + ik_{\beta_1} \sin \Theta\right)\right]\left[1 + R_0\right] \zeta_n - \frac{1}{\sqrt{m}}\left[r^2 + \frac{\gamma_2^2}{4} - inp\left(\frac{\alpha}{2} + ik_{\beta_2} \sin \delta\right)\right] T_0 \zeta_{-n}. \tag{35}$$

5. Solutions of the second approximation

Next, if the terms of higher order than ζ^2 in equations (25) and (26) are neglected then, by making use of equation (27), the following two equations are obtained:

$$\left[1 + \frac{\gamma_2}{2}\zeta + \frac{\gamma_2^2}{8}\zeta^2\right]\left\{\left[1 - is\zeta - s^2\frac{\zeta^2}{2}\right] + \left[1 + is\zeta - \frac{s^2\zeta^2}{2}\right] R_0 +\right.$$

$$\left.\sum R_n\, e^{-inpx}\left[1 + is_n\zeta - s_n^2\frac{\zeta^2}{2}\right] + \sum R_n'\, e^{inpx}\left[1 + is_n'\zeta - \frac{s_n'^2\zeta^2}{2}\right]\right\} =$$

$$= \sqrt{m}\left[1+\frac{\gamma_1}{2}+\frac{\gamma_1^2\zeta^2}{8}\right]\left\{\left[1-ir-r^2\frac{\zeta^2}{2}\right]T_0+\sum T_n e^{-inpx}\left[1-ir_n\zeta-r_n^2\zeta^2/2\right]+\right.$$

$$\left.+\sum T_n e^{inpx}\left[1-ir_n'\zeta-\frac{r_n'^2\zeta^2}{2}\right]\right\}, \tag{36}$$

$$\left[1+\frac{\gamma_1}{2}\zeta+\frac{\gamma_1^2}{8}\zeta^2\right]\left\{\left[1-is\zeta-\frac{s^2\zeta^2}{2}\right]\left[-\frac{\gamma_1}{2}-is+\left(\frac{\alpha}{2}+ik_{\beta_1}\sin\Theta\right)\zeta'\right]+\right.$$

$$+R_0\left[1+is\zeta-s^2\frac{\zeta^2}{2}\right]\left[is-\frac{\gamma_1}{2}+\left(\frac{\alpha}{2}+ik_{\beta_1}\sin\Theta\right)\zeta'\right]+$$

$$\sum R_n e^{-inpx}\left[1+is_n\zeta-s_n^2\frac{\zeta^2}{2}\right]\left[is_n-\frac{\gamma_1}{2}+\left(inp+\frac{\alpha}{2}+ik_{\beta_1}\sin\Theta\right)\zeta'\right]+$$

$$\left.+\sum R_n' e^{inpx}\left[1+is_n'\zeta-s_n'^2\frac{\zeta^2}{2}\right]\left[is_n'-\frac{\gamma_1}{2}+\left(-inp+\frac{\alpha}{2}+ik_{\beta_1}\sin\Theta\right)\zeta'\right]\right\}=$$

$$=\frac{1}{\sqrt{m}}\left[1+\frac{\gamma_2}{2}\zeta+\frac{\gamma_2^2}{8}\zeta^2\right]\left\{T_0\left[-ir-\frac{\gamma_2}{2}+\right.\right.$$

$$\left.\left(\frac{\alpha}{2}+ik_{\beta_2}\sin\delta\right)\zeta'\right]\left[1-ir\zeta-r^2\frac{\zeta^2}{2}\right]+\sum T_n e^{-inpx}\left[-ir_n-\frac{\gamma_2}{2}+\right.$$

$$\left.+\left(inp+\frac{\alpha}{2}+ik_{\beta_2}\sin\delta\right)\zeta'\right]\left[1-ir_n\zeta-\frac{r_n^2\zeta^2}{2}\right]+$$

$$\left.+\sum T_n' e^{inpx}\left[-ir_n'-\frac{\gamma_2}{2}+\left(inp+\frac{\alpha}{2}+ik_{\beta_2}\sin\delta\right)\zeta'\right]\left[1-ir_n'\zeta-r_n'^2\zeta^2/2\right]\right\} \tag{37}$$

From equations (36) and (37) we obtain the second order approximation for R_0, T_0, R_n', T_n', R_n and T_n by picking up the terms independent of x; collecting the coefficients of e^{-inpx}; and the coefficients of e^{inpx}. They are as follows:

$$R_0\left[1+\zeta_n\zeta_{-n}\left(\frac{\gamma_2^2}{4}+i\gamma_2 s\right)\right]-\sqrt{m}\,T_0\left[1+\zeta_n\zeta_{-n}\left(\frac{\gamma_1^2}{4}-ir\gamma_1\right)\right]=$$

$$=\left(\frac{\gamma_2^2}{4}-is\gamma_2\right)\zeta_n\zeta_{-n}-1-R_n\left(is_n+\frac{\gamma_2}{2}\right)\zeta_n-R_n'\left(is_n'+\frac{\gamma_2}{2}\right)\zeta_{-n}+$$

$$+T_n\sqrt{m}\left(\frac{\gamma_1}{2}-ir_n\right)\zeta_n+\sqrt{m}\,T_n'\left(\frac{\gamma_1}{2}-ir_n'\right), \tag{38}$$

$$R_0\left[\mathrm{i}s-\frac{\gamma_1}{2}\right]\left[1+\zeta_n\zeta_{-n}\left(\mathrm{i}s\,\gamma_1-s^2+\frac{\gamma_1^2}{4}\right)\right]-T_0\frac{1}{\sqrt{m}}\left[\mathrm{i}r+\frac{\gamma_2}{2}\right]\left[-1+\right.$$

$$\left.+\zeta_n\zeta_{-n}\left(\mathrm{i}r\gamma_2+r^2-\frac{\gamma_2^2}{4}\right)\right]=\left[\mathrm{i}s+\frac{\gamma_1}{2}\right]\left[1-\zeta_n\zeta_{-n}\left(\mathrm{i}s\gamma_1+s^2-\gamma_1^2/4\right)\right]+$$

$$+R_n\zeta_n\left[s_n^2+\frac{\gamma_1^2}{4}-\mathrm{i}np\left(\mathrm{i}np+\frac{\alpha}{2}+\mathrm{i}k_{\beta_1}\sin\Theta\right)\right]+R_n'\zeta_{-n}\left[s_n^{12}+\frac{\gamma_1^2}{4}+\mathrm{i}np+\frac{\alpha}{2}+\right.$$

$$\left.+ik_{\beta_1}\sin\Theta\right)\Big]-\frac{1}{\sqrt{m}}T_n\zeta_n\left[r_n^2+\frac{\gamma_2^2}{4}-\mathrm{i}np(\mathrm{i}np+\alpha/2+\mathrm{i}k_{\beta_1}\sin\delta)\right]-$$

$$-\frac{T_n'}{\sqrt{m}}\zeta_{-n}\left[r_n'^2+\frac{\gamma_2^2}{4}+\mathrm{i}np\left(-\mathrm{i}np+\frac{\alpha}{2}+\mathrm{i}k_{\beta_2}\sin\delta\right)\right], \tag{39}$$

$$\left(\frac{\gamma_2}{2}-\mathrm{i}s\right)\zeta_{-n}+R_0\Big)\left(\mathrm{i}s+\frac{\gamma_2}{2}\right)\zeta_{-n}+R_n\left[+1\left(\frac{\gamma_2^2}{4}-s_n^2+\mathrm{i}s_n\gamma_2\right)\zeta_n\zeta_{-n}\right]+$$

$$+R_n'\zeta_{-n}^2\left(\frac{\gamma_2^2}{8}-\frac{s_n'^2}{2}+\mathrm{i}s_n'\frac{\gamma_2}{2}\right)=\sqrt{m}\,T_0\left(\frac{\gamma_1}{2}-\mathrm{i}r\right)\zeta_{-n}+\sqrt{m}\,T_n\left[1+\right.$$

$$\left.+\left(\frac{\gamma_1^2}{4}-r_n^2-\mathrm{i}r_n\gamma_1\right)\zeta_n\zeta_{-n}\right]+\sqrt{m}\,T_n'\zeta_{-n}^2\left(\frac{\gamma_2^2}{8}-\frac{r_n'^2}{2}-\mathrm{i}r_n\frac{\gamma_1}{2}\right), \tag{40}$$

$$\left[s^2+\frac{\gamma_1^2}{2}+\mathrm{i}np\left(\frac{\alpha}{2}+\mathrm{i}k_{\beta_1}\sin\Theta\right)\right]\zeta_{-n}+R_0\zeta_{-n}\left[s^2+\mathrm{i}np\left(\frac{\alpha}{2}+\right.\right.$$

$$\left.\left.+\mathrm{i}k_{\beta_1}\sin\Theta\right)+\frac{\gamma_1^2}{4}\right]-R_n\left[\mathrm{i}s_n-\frac{\gamma_1}{2}\right]\left[1+\zeta_n\zeta_{-n}\left(\frac{\gamma_1^2}{4}-s_n^2+\mathrm{i}\gamma_1 s_n\right)\right]-$$

$$-R_n'\zeta_{-n}^2\left[\left(\mathrm{i}s_n'-\frac{\gamma_1}{2}\right)\left(\frac{\gamma_2^2}{8}+\mathrm{i}\frac{\gamma_2 s_n}{2}-s_n'^2/2\right)+np\left(\mathrm{i}s_n-\mathrm{i}\frac{\gamma_1}{2}\right)\left(\frac{\alpha}{2}-\mathrm{i}np+\right.\right.$$

$$\left.\left.\mathrm{i}k_{\beta_1}\sin\Theta\right)\right]=\frac{1}{\sqrt{m}}T_0\left[r^2+\frac{\gamma_2^2}{4}+\mathrm{i}np\left(\frac{\alpha}{2}+\mathrm{i}k_{\beta_1}\sin\Theta\right)\right]\zeta_{-n}+$$

$$+\frac{1}{\sqrt{m}}T_n\left[\mathrm{i}r_n+\frac{\gamma_2}{2}\right]\left[1+\zeta_n\zeta_{-n}\left(\frac{\gamma_2^2}{4}-r_n^2-\mathrm{i}r_n\gamma_2\right)\right]-\frac{1}{\sqrt{m}}T_n'\zeta_{-n}^2$$

$$\left[\left(\mathrm{i}r_n'+\frac{\gamma_2}{2}\right)\left(\frac{r_n'^2}{2}+\mathrm{i}r_n'\frac{\gamma_2}{2}-\frac{\gamma_2^2}{8}\right)-np\left(r_n'+\mathrm{i}\frac{\gamma_2}{2}\right)\left(\frac{\alpha}{2}-\mathrm{i}np+\mathrm{i}k_{\beta_2}\sin\delta\right)\right], \tag{41}$$

$$\left(\frac{\gamma_2}{2}-\mathrm{i}s\right)\zeta_n+R_0\left(\mathrm{i}s+\frac{\gamma_2}{2}\right)\zeta_n+R_n\zeta_n^2\left(\frac{\gamma_2^2}{8}+\mathrm{i}s_n\frac{\gamma_2}{2}-\frac{s_n^2}{2}\right)+$$

$$R_n'\left[1+\zeta_n\zeta_{-n}\left(\frac{\gamma_2^2}{4}-s_n^2+\mathrm{i}\gamma_2 s_n\right)\right]=\sqrt{m}\,T_0\left(\frac{\gamma_1}{2}-\mathrm{i}r\right)\zeta_n+\sqrt{m}$$

$$T_n\left(\frac{\gamma_1^2}{8}-\mathrm{i}r_n\frac{\gamma_1}{2}-\frac{\gamma_n^2}{2}\right)\zeta_n^2+T_n'\sqrt{m}\left[1+\zeta_n\zeta_{-n}\left(\frac{\gamma_1^2}{4}-r_n'^2-\mathrm{i}\gamma_2 r_n\right)\right], \tag{42}$$

$$\left[s^2+\frac{\gamma_1^2}{4}-\mathrm{i}np\left(\frac{\alpha}{2}+\mathrm{i}k_{\beta_1}\sin\Theta\right)\right]\zeta_n+R_0\left[s^2+\frac{\gamma_1^2}{4}-\mathrm{i}np\left(\frac{\alpha}{2}+\mathrm{i}k_{\beta_1}\sin\Theta\right)\right]\zeta_n-$$

$$-R_n\left[\left(\mathrm{i}s_n-\frac{\gamma_1}{2}\right)\left(\frac{\gamma_1^2}{8}-\frac{s_n^2}{2}+\mathrm{i}s_n\frac{\gamma_1}{2}\right)+np\left(\mathrm{i}\frac{\gamma_1}{2}-s_n\right)\left(\mathrm{i}np+\frac{\alpha}{2}+\right.\right.$$

$$\left.\left.+\mathrm{i}k_{\beta_1}\sin\Theta\right)\right]\zeta_n^2-R_n'\left[\mathrm{i}s_n'-\frac{\gamma_1}{2}\right]\left[1+\left(\frac{\gamma_1^2}{4}-s_n'^2+\mathrm{i}s_n'\gamma_1\right)\zeta_n\zeta_{-n}\right]=$$

$$=\frac{1}{\sqrt{m}}T_0\left[r^2+\frac{\gamma_2^2}{4}-\mathrm{i}np\left(\frac{\alpha}{2}+\mathrm{i}k_{\beta_2}\sin\delta\right)\right]-\frac{1}{\sqrt{m}}T_n\left[\left(\mathrm{i}r_n+\frac{\gamma_2}{2}\right)\left(\frac{r_n^2}{2}-\frac{\gamma_1^2}{8}+\right.\right.$$

$$\left.+\mathrm{i}r_n-\frac{\gamma_1}{2}\right)+np\left(r_n+\mathrm{i}\frac{\gamma_1}{2}\right)\left(\mathrm{i}np+\frac{\alpha}{2}+\mathrm{i}k_{\beta_2}\sin\delta\right)\left.\right]\zeta^2+\frac{1}{\sqrt{m}}T_n'\left[\mathrm{i}r_n'+\frac{\gamma_2}{2}\right]$$

$$\left[1+\zeta_n\zeta_{-n}\left(\frac{\gamma_2^2}{4}-r_n'^2-\mathrm{i}r_n'\gamma_1\right)\right] \tag{43}$$

Equations (38) – (43) give the reflection and transmission coefficients for the second order approximation.

6. Normal incidence on the boundary surface $\zeta = c\cos px$

For simplicity's sake, normal incidence on the boundary surface given by the equation $\zeta = c\cos px$, has been computed numerically. In this case, $\zeta_n=\zeta_{-n}=0\,(n\neq 1);\zeta_1=\zeta_{-1}=c/2;\Theta=\delta=0;\cos\Theta_1=\cos\Theta_1'$ and $\cos\delta_1=\cos\delta_1'$. Then the solutions of the first order approximation for R_1 and T_1 are given as follows:

$$R_1=c\bar{s}\left[2\,[1-m]\,[mp\alpha-\gamma_2\,(\bar{r}+\bar{r}_1)]+\mathrm{i}\,[(1-m)(4\gamma_1\gamma_2+\gamma_2^2-m\gamma_1\gamma_2-4\bar{r}\bar{r}_1)+\right.$$

$$\left.+4m(m\bar{s}^2-\bar{r}^2)+m(m\gamma_1^2-\gamma_2^2)]\right]/deno, \tag{44}$$

$$T_1 = c\bar{s}\sqrt{m}\Big[2(1-m)(\gamma_2\bar{s}-\gamma_1\bar{r}+p\alpha)+\mathrm{i}(1-m)(4\bar{r}\bar{s}_1+\gamma_1\gamma_2)+4(m\bar{s}^2-\bar{r}^2)+$$

$$+(m\gamma_1^2-\gamma_2^2)\Big]/deno, \tag{45}$$

where

$$deno = [(\gamma_2-m\gamma_1)^2-4(m\bar{s}+\bar{r}_1)(m\bar{s}+\bar{r})+2\mathrm{i}[\gamma_2-m\gamma_1][(m\bar{s}_1+\bar{r}_1)+(m\bar{s}+\bar{r})]. \tag{46}$$

In this particular case: $\bar{s}$, $\bar{r}$, $\bar{s}_1$ and $\bar{r}_1$ are given [from Equations (12), (13), (17) and (21)] by:

$$\bar{s} = \begin{cases} \left[k_{\beta_1}^2-\frac{1}{4}(\alpha^2+\gamma_1^2)\right]^{1/2} & \text{for} \quad k_{\beta_1} > \frac{1}{2}(\alpha^2+\gamma_1^2)^{1/2} \\ -\mathrm{i}\left[\frac{1}{4}(\alpha^2+\gamma_1^2)-k_{\beta_1}^2\right]^{1/2} & \text{for} \quad k_{\beta_1} < \frac{1}{2}(\alpha^2+\gamma_1^2)^{1/2}, \end{cases}$$

$$\bar{r} = \begin{cases} \left[k_{\beta_2}^2-\frac{1}{4}(\alpha^2+\gamma_2^2)\right]^{1/2} & \text{for} \quad k_{\beta_2} > \frac{1}{2}(\alpha^2+\gamma_2^2)^{1/2} \\ -\mathrm{i}\left[\frac{1}{4}(\alpha^2+\gamma_2^2)-k_{\beta_2}^2\right]^{1/2} & \text{for} \quad k_{\beta_2} < \frac{1}{2}(\alpha^2+\gamma_2^2)^{1/2}, \end{cases}$$

$$\bar{s}_1 = \begin{cases} \left[k_{\beta_1}^2-p^2-\frac{1}{4}(\alpha^2+\gamma_1^2)\right]^{1/2} & \text{for} \quad k_{\beta_1} > p^2+\frac{1}{4}(\alpha^2+\gamma_1^2)^{1/2} \\ -\mathrm{i}\left[p^2+\frac{1}{4}(\alpha^2+\gamma_1^2)-k_{\beta_1}^2\right]^{1/2} & \text{for} \quad k_{\beta_1} < p^2+\frac{1}{4}(\alpha^2+\gamma_1^2)^{1/2}, \end{cases}$$

$$\bar{r}_1 = \begin{cases} \left[k_{\beta_2}^2-p^2-\frac{1}{4}(\alpha^2+\gamma_2^2)\right]^{1/2} & \text{for} \quad k_{\beta_2} > p^2+\frac{1}{4}(\alpha^2+\gamma_2^2)^{1/2} \\ -\mathrm{i}\left[p^2+\frac{1}{4}(\alpha^2+\gamma_2^2)-k_{\beta_2}^2\right]^{1/2} & \text{for} \quad k_{\beta_2} < p^2+\frac{1}{4}(\alpha^2+\gamma_2^2)^{1/2} \end{cases} \tag{47}$$

7. Numerical computations

The computations have been carried out by assuming the elastic parameters as:

$$\begin{aligned} &\beta_1 = 4.358 \text{ km/s}, \quad && p_1 = 3.32 \text{ gm/cm}^3, \\ &\beta_2 = 6.707 \text{ km/s}, \quad && p_2 = 4.93 \text{ gm/cm}^3 \end{aligned} \tag{48}$$

and

$$\gamma_1 = -0.0087, \quad \gamma_2 = -0.0030, \quad \alpha = 0.0020. \tag{49}$$

The effects of the lateral and vertical variation constants and of the frequency of the incident SH-wave have been examined numerically and graphically for the normal incidence case, against the dimensionless parameter cp; c being the amplitude of the corrugated boundary.

8. Effect of frequency

Computations have been made for four different values of $\Omega(=\omega c/\beta_1)$, namely $\Omega=0.5$, 1.0, 1.5 and 2.0 at intervals of 0.01.

It has been observed that for large frequency, the behaviour of the reflection and transmission coefficients remains the same. The values of these coefficients increase with the increase in Ω. These coefficients have been plotted graphically in *Figures 2* and *3* respectively for $\Omega=0.5$, 1.0 and 1.5.

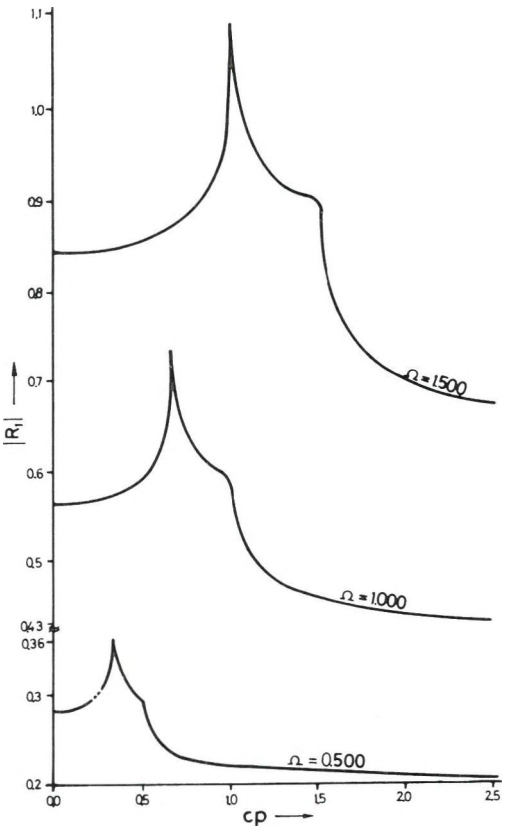

Fig. 2. Reflection coefficient $|R_1|$ of irregular SH-waves for normal incidence against the dimensionless parameter cp for different values of the dimensionless frequency $\Omega = \omega c/\beta_1$

2. ábra. A szabálytalan SH-hullámok $|R_1|$ reflexiós együtthatója merőleges beesés mellett a cp dimenzió nélküli paraméter függvényében, az $\Omega = \omega c/\beta_1$ dimenzió nélküli frekvencia különböző értékeire

Рис. 2. Коэффициент отражения $|R_1|$ неправильных волн SH при перпендикулярном вхождении в зависимости от безразмерного параметра cp и при различных значениях безразмерной частоты $\Omega = \omega c/\beta_1$.

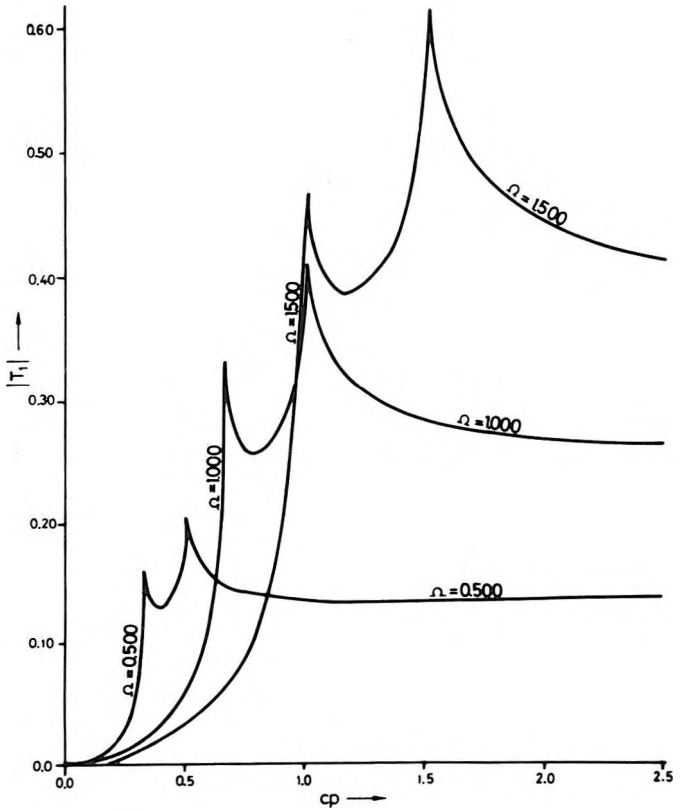

Fig. 3. Transmission coefficient $|T_1|$ of irregular SH-waves for normal incidence against the dimensionless parameter cp for different values of the dimensionless frequency $\Omega = \omega c/\beta_1$

3. ábra. A szabálytalan SH-hullámok $|T_1|$ transzmissziós együtthatója merőleges beesés mellett a cp dimenzió nélküli paraméter függvényében, az $\Omega = \omega c/\beta_1$ dimenzió nélküli frekvencia különböző értékeire

Рис. 3. Коэффициент передачи $|T_1|$ неправильных волн SH при перпендикулярном вхождении в зависимости от безразмерного параметра cp и при различных значениях безразмерной частоты $\Omega = \omega c/\beta_1$.

9. Effect of lateral variation

Computations have been made for different values of α, namely $\alpha = 0.001$, 0.002, 0.004, 0.008 and 0.016 at intervals of 0.01, keeping $\Omega = 1.0$ fixed. It has been observed that with the increase in α, the value of the reflection coefficient decreases slowly and this decrease is large for larger values of cp. But the value

of the transmission coefficient increases with the increase in α and this increase is also large for larger values of *cp*. The behaviour of the reflection and transmission coefficients for two different values of α, namely $\alpha = 0.002$ and 0.008, have been plotted graphically in *Figures 4* and *5* respectively.

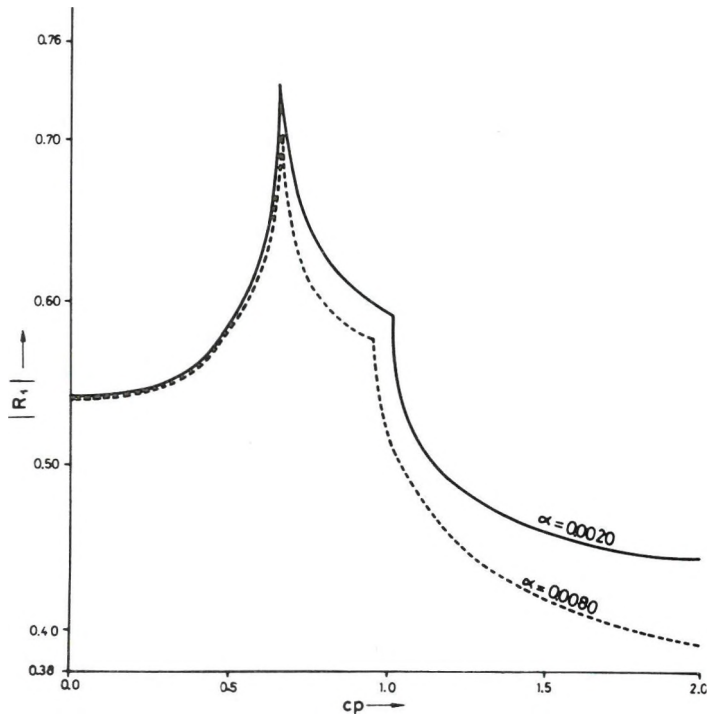

Fig. 4. Reflection coefficient $|R_1|$ of irregular SH-waves for normal incidence against the dimensionless parameter *cp* for different values of the lateral variation constant α

4. ábra. A szabálytalan SH-hullámok $|R_1|$ reflexiós együtthatója merőleges beesés mellett a *cp* dimenzió nélküli paraméter függvényében, az α oldalirányú variációs állandó különböző értékeire

Рис. 4. Коэффициент отражения $|R_1|$ неправильных волн SH при перпендикулярном вхождении в зависимости от безразмерного параметра *cp* и при различных значениях коэффициента вариаций α по латерали.

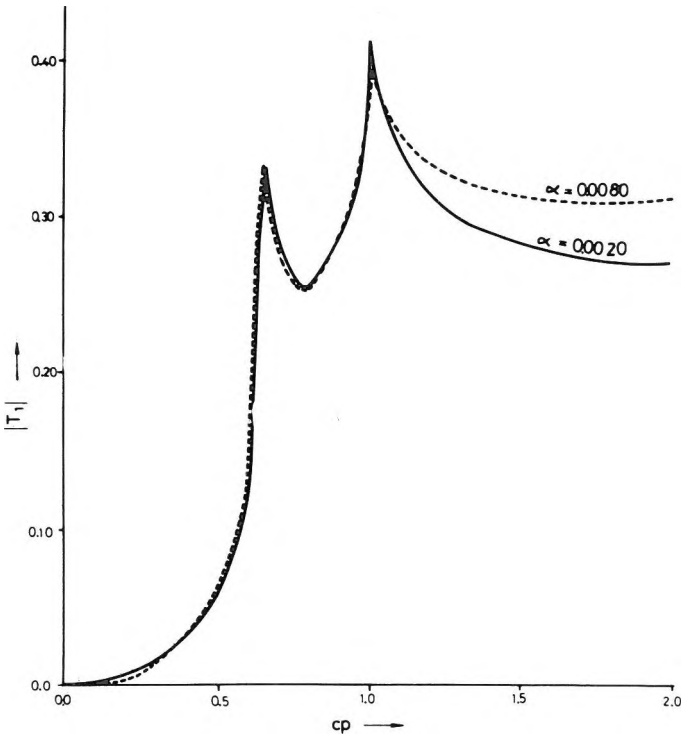

Fig. 5. Transmission coefficient $|T_1|$ of irregular SH-waves for normal incidence against the dimensionless parameter *cp* for different values of the lateral variation constant α

5. ábra. A szabálytalan SH-hullámok $|T_1|$ transzmissziós együtthatója merőleges beesés mellett a *cp* dimenzió nélküli paraméter függvényében, az α oldalirányú variációs állandó különböző értékeire

Рис. 5. Коэффициент передачи $|T_1|$ неправильных волн SH при перпендикулярном вхождении в зависимости от безразмерного параметра *cp* и при различных значениях коэффициента вариаций α по латерали.

10. Effect of vertical variation

Effects of the vertical variation constants γ_1 and γ_2 were considere separately. Computations have been made for different values of γ namely: $\gamma_1 = -0.0043$, -0.0087, -0.0174, -0.0348 and -0.0696 at intervals of 0.01, keeping $\Omega = 1.0$ fixed. It has been observed that as γ_1 decreases, the value of the reflection coefficient decreases slowly and this decrease remains almost the same

for all values of *cp*. The transmission coefficient increases slowly with the decrease in γ_1 and this decrease is slightly large for larger values of *cp*. The behaviour of these coefficients for two different values of γ_1, namely: $\gamma_1 = -0.0087$ and -0.0348 have been plotted graphically in *Figures 6* and *7* respectively.

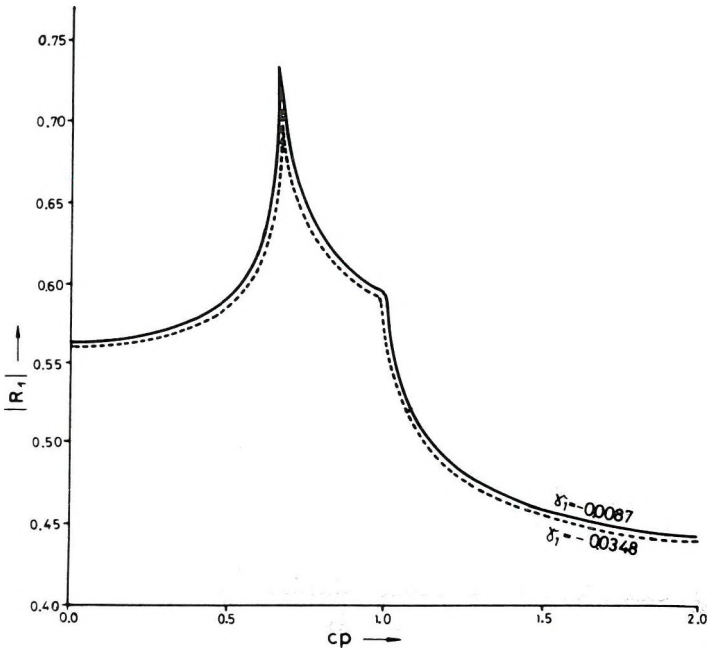

Fig. 6. Reflection coefficient $|R_1|$ of irregular SH-waves for normal incidence against the dimensionless parameter *cp* for different values of the vertical variation constant γ_1 in the lower half-space

6. ábra. A szabálytalan SH-hullámok $|R_1|$ reflexiós együtthatója merőleges beesés mellett a *cp* dimenzió nélküli paraméter függvényében, a γ_1 függőleges irányú variációs állandó különböző értékeire, az alsó féltérben

Рис. 6. Коэффициент отражения $|R_1|$ неправильных волн SH при перпендикулярном вхождении в зависимости от безразмерного параметра *cp* и при различных значениях коэффициента вариаций γ_1 по вертикали в нижнем полупространстве.

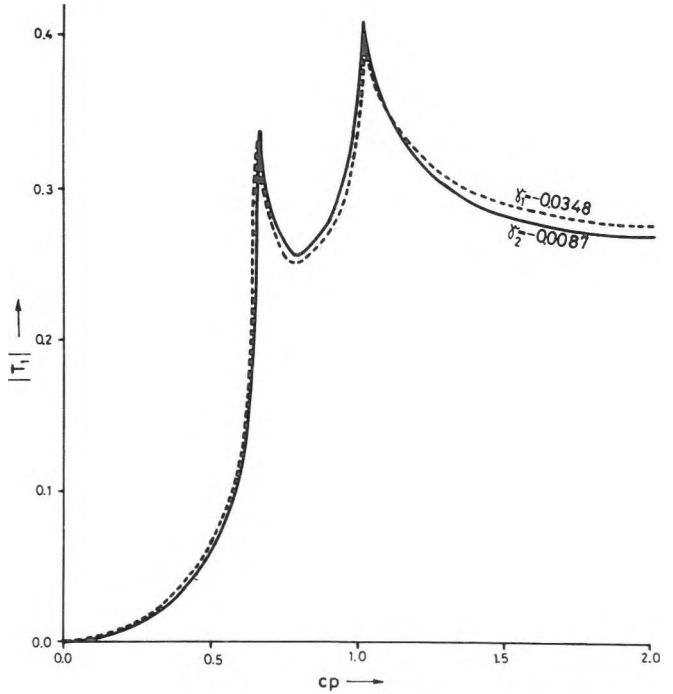

Fig. 7. Transmission coefficient $|T_1|$ of irregular SH-waves for normal incidence against the dimensionless parameter *cp* for different values of the vertical variation constant γ_1 in the lower half-space

7. ábra. A szabálytalan SH-hullámok $|T_1|$ transzmissziós együtthatója merőleges beesés mellett a *cp* dimenzió nélküli paraméter függvényében, a γ_1 függőleges irányú variációs állandó különböző értékeire, az alsó féltérben

Рис. 7. Коэффициент передачи $|T_1|$ неправильных волн SH при перпендикулярном вхождении в зависимости от безразмерного параметра *cp* и при различных значениях коэффициента вариаций γ_1 по вертикали в нижнем полупространстве.

To find the effect of vertical variation constant γ_2, computations have been made for different values of γ_2 namely: $\gamma_2 = -0.0015$, -0.0030, -0.0060, -0.0120 and -0.0240 at intervals of 0.01, keeping $\Omega = 1.0$ fixed. It has been observed that as *cp* increases, the value of the reflection coefficient first increases and after reaching its maximum value, it starts decreasing. However, R_1 is smaller for smaller values of γ_2 until the maximum is attained, while the behaviour is reversed after the maximum is reached. The value of the transmission coefficient decreases with the increase in γ_2. This behaviour remains for

small values of *cp*, but for large *cp* the behaviour of the transmission coefficient for γ_2 is reversed. The value of the transmission coefficient starts increasing with the increase in γ_2. The behaviour of the reflection and transmission coefficients for two different values of γ_2, namely $\gamma_2 = -0.003$ and -0.12, have been plotted graphically in *Figures 8* and *9* respectively.

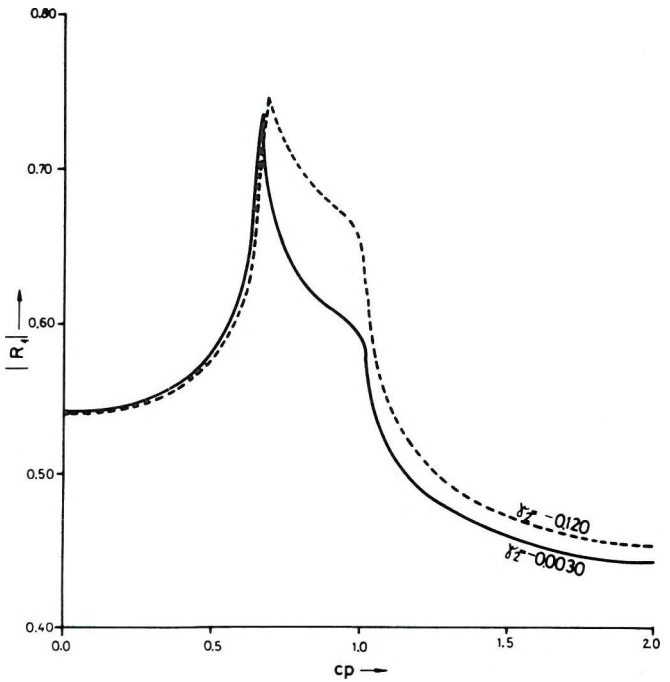

Fig. 8. Reflection coefficient $|R_1|$ of irregular SH-waves for normal incidence against the dimensionless parameter *cp* for different values of the vertical variation constant γ_2 in the upper half-space

8. ábra. A szabálytalan SH-hullámok $|R_1|$ reflexiós együtthatója merőleges beesés mellett a *cp* dimenzió nélküli paraméter függvényében, a γ_2 függőleges irányú variációs állandó különböző értékeire, a felső féltérben

Рис. 8. Коэффициент отражения $|R_1|$ неправильных волн SH при перпендикулярном вхождении в зависимости от безразмерного параметра *cp* и при различных значениях коэффициента вариаций γ_2 по вертикали в верхнем полупространстве.

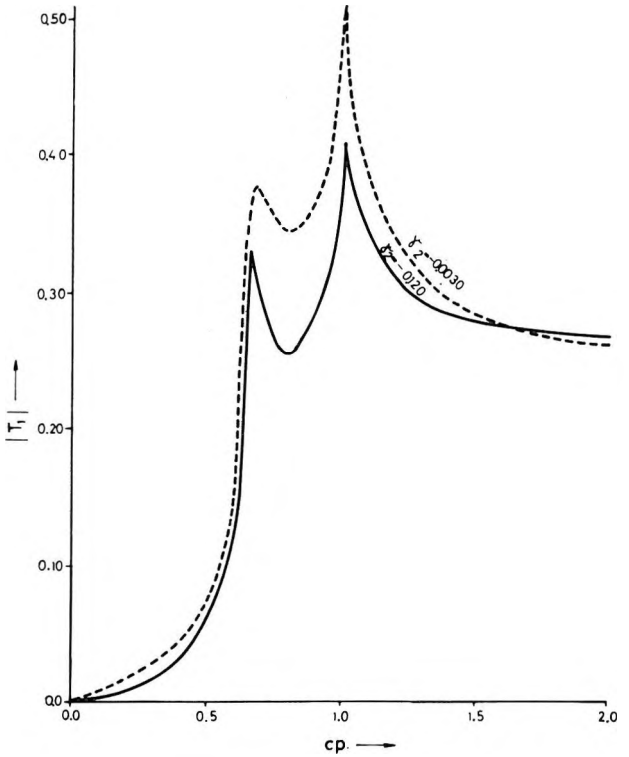

Fig. 9. Transmission coefficient $|T_1|$ of irregular SH-waves for normal incidence against the dimensionless parameter *cp* for different values of the vertical variation constant γ_2 in the upper half-space

9. ábra. A szabálytalan SH-hullámok $|T_1|$ transzmissziós együtthatója merőleges beesés mellett a *cp* dimenzió nélküli paraméter függvényében, a γ_2 függőleges irányú variációs állandó különböző értékeire, a felső féltérben

Рис. 9. Коэффициент передачи $|T_1|$ неправильных волн SH при перпендикулярном вхождении в зависимости от безразмерного параметра *cp* и при различных значениях коэффициента вариаций γ_2 по вертикали в верхнем полупространстве.

11. Effect of velocity contrast

The effect of the velocity contrast has been seen for three different cases, namely for the first case SH-wave velocity in the incident medium is taken as 3.00 km/s and in the refracted medium as 5.00 km/s; the density ratio of the two media ($\varrho_{10}/\varrho_{20}$) being 4.8, called model (3.0/5.0). For the second case, SH-wave velocity in the incident medium is taken as 5.00 km/s and in the refracted medium as 6.00 km/s; the density ratio being 1.6, called model (5.0/6.0). For the

third case, SH-wave velocity in the incident medium is taken as 7.5 km/s and in the refracted medium as 7.0 km/s: the density ratio being 1.2, called model (7.5/7.0). With these distributions of velocity and density the other elastic constants are taken to be the same as in (49). *Figure 10* shows how the amplitude of the irregular waves or the reflection coefficient changes with the amplitude of the corrugation. As R_1 is proportional to the amplitude of the corrugation in this approximation, the graphs are given by straight lines. Thus Figure 10 shows that the larger the velocity contrast and the larger the amplitude of the corrugation, the larger is the effect of corrugation. The results obtained in this case are nearly the same as those derived by ASANO [1966] for the case of P-waves, when the medium considered was homogeneous.

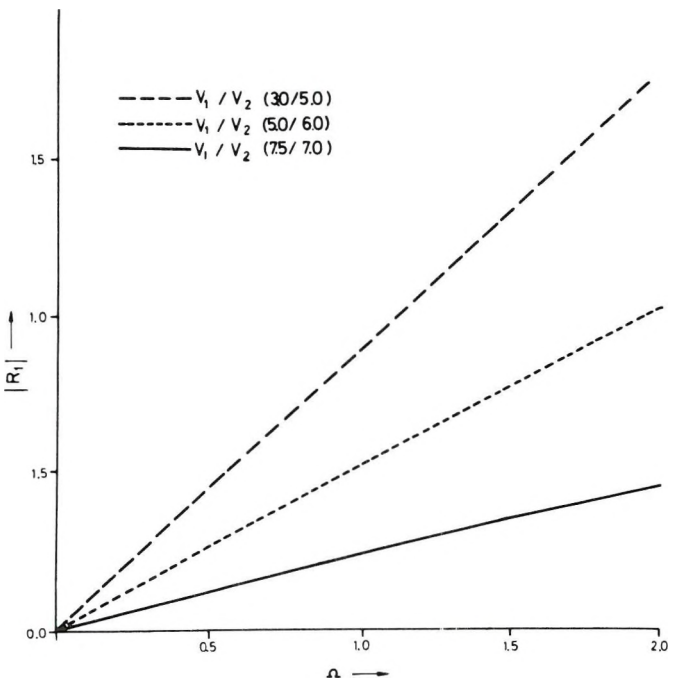

Fig. 10. Reflection coefficient $|R_1|$ of irregular SH-waves for three different velocity models for normal incidence against the dimensionless parameter $\Omega = \omega c/\beta_1$

10. ábra. A szabálytalan SH-hullámok $|R_1|$ reflexiós együtthatója három különböző sebességmodellre, merőleges beesés mellett, az $\Omega = \omega c/\beta_1$ dimenzió nélküli paraméter függvényében

Рис. 10. Коэффициент отражения $|R_1|$ неправильных волн SH для трех различных моделей распределения скоростей при перпендикулярном вхождении в зависимости от безразмерного параметра $\Omega = \omega c/\beta_1$.

REFERENCES

ABUBAKAR I. 1962a: Scattering of plane elastic waves of rough surfaces. Proc. Camb. Phil. Soc. **58,** pp. 136–157

ABUBAKAR I. 1962b: Reflection and refraction of plane SH waves at irregular interfaces–I. J. Phys. Earth, **10,** pp. 1–14

ABUBAKAR I. 1962c: Reflection and refraction of plane SH waves at irregular interfaces–II. J. Phys. Earth, **10,** pp. 15–20

ADAMS W. M. and CHUNG-PO CHANG 1964: Wave propagation phenomena at an irregular infinite interface: Part I: Theory. Bull. Seism. Soc. Am. **54,** 6, pp. 2209–2222

ASANO S. 1960: Reflection and refraction of elastic waves at a corrugated boundary surface: Part I. Bull. Earthq. Res. Inst. **38,** pp. 177–197

ASANO S. 1961: Reflection and refraction of elastic waves at a corrugated boundary surface: Part II. Bull. Earthq. Res. Inst. **39,** pp. 367–466

ASANO S. 1966: Reflection and refraction of elastic waves at a corrugated interface. Bull. Seism. Soc. Am. **56,** 1, pp. 201–222

BREKHOVSKIKH L. M. 1951: Diffraction of sound waves at an uneven surface. Doklady Akad. Nauk SSSR **79,** 585 p.

BREKHOVSKIKH L. M. 1959: Propagation of surface Rayleigh waves along the uneven boundary of an elastic solid. English translation in Soviet Physics–Acoustics. Akusticheskiy Zhurnal, **5,** pp. 282–289

CHATTOPADHYAY A. and PAL A. 1982: Propagation of SH waves in an inhomogeneous medium with irregular interface lying over an initially stressed elastic half-space. Bul. Inst. Politeh. 'Gheorghe Gheorghiu – Dej' Bucuresti, Ser. Electroteh. **44,** 3, pp. 47–56

DERESIEWICZ H. and WOLF B. 1964: The effect of boundaries on wave propagation in a liquid filled porous solid: IX.: Reflection of plane waves at an irregular boundary. Bull. Seism. Soc. Am. **54,** 5, pp. 1537–1561

DUNKIN J. W. and ERINGEN A. C. 1962: Reflection of elastic waves from the wavy boundary of a half-space. Proc. 4th U.S. Nat. Congr. Appl. Mech. (Berkeley), pp. 143–160

ECKART C. 1953: The scattering of sound waves from the free surface. J. Acoustic Soc. Am. **25,** pp. 566–570

GILBERT F. and KNOPOFF L. 1960: Seismic scattering from topographic irregularities. J. Geophys. Res. **65,** pp. 3437–3444

GUPTA S. K. 1978: Reflections and refractions from curved interfaces: model-study. Geophys. Prospect. **26,** 1, pp. 82–96

HERRERA I. 1964: A perturbation method for elastic wave propagation 1. Nonparallel Boundaries. J. Geophys. Res. **69,** pp. 3845–3851

HERRERA I. and MAL A. K. 1965: A perturbation method for elastic wave propagation 2. Small inhomogeneities. J. Geophys. Res. **70,** pp. 871–883

HOMMA S. 1941: The effect of topography on the surface vibration. J. Seism. **11,** pp. 349–364

ITS E. N. and YANOVSKAYA T. B. 1985: Reflection and refraction of surface waves on a curved interface. Vychisl. Seismol. **15,** pp. 87–92

LEVY A. and DERESIEWICZ H. 1967: Reflection and transmission of elastic waves in a system of corrugated layers. Bull. Seism. Soc. Am. **57,** 3, pp. 393–419

LYSANOV I. P. 1958: Theory of the scattering of waves at periodically uneven surface. English translation in Soviet Physics-Acoustics. Akusticheskii Zhurnal, **4,** pp. 3–12

MALHOTRA S., CHOPRA S. D. and GOGNA M. L. 1982: Reflection transmission of SH waves from a laterally and vertically heterogeneous transition layer of a finite thickness. Acta Geophys. Pol. **30,** 4. pp. 341–357

MILES J. W. 1954: On non-specular reflection at a rough surface. Acoust. Soc. Am. **26,** pp. 191–199

PARKAR I. G. 1956: Reflection of plane sound waves from an irregular surface. J. Acoust. Soc. Am. **28,** pp. 672–680

PARKAR I. G. 1957: Reflection of plane sound waves from a sinusoidal surface. J. Acoust. Soc. Am. **29,** pp. 377–380

RAYLEIGH Lord 1893: On the reflection of sound or light from a corrugated surface. Rep. Brit. Assoc. Adv. Sci. pp. 690–691

RAYLEIGH Lord 1896: The theory of sound, 2nd ed. art. 270, Dover Publications.

RAYLEIGH Lord 1907: On the dynamical theory of gratings. Proc. Roy. Soc. Lond. A, **79,** pp. 399–416

SATO R. 1955: The reflection of elastic waves on corrugated surface. Zisin (ii), (J. Seism. Soc. Japan), **8,** pp. 8–22

SINGH B. M., SINGH S. J. and CHOPRA S. D. 1978: Reflection and refraction of SH waves at the plane boundary between two laterally and vertically heterogeneous solids. Acta Geophys. Pol. **36,** pp. 209–216

SLAVIN L. M. and WOLF B. 1970: Scattering of Love waves in a surface layer with an irregular boundary for the case of a rigid underlying halfspace. Bull. Seism. Soc. Am. **60,** 3, pp. 859–877

SUMNER J. H. and DERESIEWICZ H. 1972: Waves in an elastic plate with an irregular boundary. Pure Appl. Geophys. **96,** IV, pp. 106–125

TWERSKY V. 1957: On the scattering and reflection of sound by rough surfaces. J. Acoust. Soc. Am. **29,** pp. 209–226

WOLF B. 1967: Propagation of Love waves in surface layers of varying thickness. Pure Appl. Geophysics, **67,** II, pp. 76–82

WOLF B. 1970: Propagation of Love waves in layers with irregular boundaries. Pure Appl. Geophysics **78,** I, pp. 48–57

YAMADA T. and SATO R. 1976: SH wave propagation in a medium having step-shaped discontinuity. J. Phys. Earth **24,** 2, pp. 105–130

YANOVSKAYA T. B. 1984: Solution of the inverse problem of seismology for laterally inhomogeneous media. Geophys. J. Roy. Astron. Soc. **79,** 1, pp. 293–304

SH-HULLÁMOK REFLEXIÓJA ÉS TRANSZMISSZIÓJA FÜGGŐLEGES- ÉS OLDALIRÁNYBAN HETEROGÉN KÖZEGBEN, SZABÁLYTALAN HATÁRFELÜLETEN

Suversha GUPTA

SH-síkhullámok reflexiós és transzmissziós együtthatóját tanulmányozza két vízszintes és függőleges irányban heterogén közeg közötti hullámos határfelületen, a Rayleigh-féle közelítő módszerrel. Az oldal- és függőleges irányú variációs állandók, a hullámos határfelület amplitúdója, a szabálytalan határfelület hullámhossza és a sebességkontraszt hatását vizsgálja numerikusan és grafikusan, merőleges beesés esetére, elsőrendű közelítés mellett.

ОТРАЖЕНИЕ И ПЕРЕДАЧА ВОЛН SH В БОКОВОМ И ВЕРТИКАЛЬНОМ НАПРАВЛЕНИЯХ В НЕОДНОРОДНОЙ СРЕДЕ В СЛУЧАЕ НЕПРАВИЛЬНЫХ ГРАНИЧНЫХ ПОВЕРХНОСТЕЙ

Суверша ГУПТА

С помощью приближения Рэлея рассматриваются коэффициенты отражения и передачи плоскостных волн SH, относящиеся к складчатой граничной поверхности раздела между двумя слоями, неоднородными как по вертикали, так и по латерали. Для случая прямого вхождения волн и приближения первого порядка в цифровом и графическом виде исследовано влияние коэффициентов вариаций по вертикали и по латерали, амплитуды складок поверхности раздела, длины волн неправильной поверхности раздела и контраста скоростей.

GEOPHYSICAL TRANSACTIONS 1987
Vol. 33. No. 2. pp. 113–122

ASPECTS OF FINITE DIFFERENCE MODELLING OF THE ELECTROMAGNETIC FIELD OF AN OSCILLATING ELECTRIC DIPOLE

Gábor PETHŐ*

Assuming a harmonic time dependent electric source parallel to the strike the paper deals with the determination of its electromagnetic field for the plane which is perpendicular to the strike and contains the source. The chosen numerical procedure is the finite difference method. A direct method taking the blocked-tridiagonal structure of coefficient matrix into consideration is recommended for solving the resulting linear system. After solving the set of equations for numerous spatial wavenumbers the field components are determined numerically by inverse Fourier transformation. The number and distribution of discrete spatial wavenumbers need to be planned. The way of planning is shown by an example.

Keywords: 2-D structure, conductivity, electric dipole source, finite difference method, Fourier transformation

1. Introduction

If we assume a 2-D conductivity structure the determination of the electromagnetic field of an electric source treated as a point source is a 3-D problem. Fourier transformation may be used to substitute the three-dimensional problem for a series of two-dimensional problems. In the case of direct current sounding Laplace's and Poisson's equations and in the present case (frequency sounding) Maxwell's equations are to be Fourier transformed over the strike direction. As a result of Fourier transformation the series of 2-D problems belongs to different spatial wavenumbers; inverse Fourier transformation enables the field to be calculated. DEY and MORRISON [1979] developed this method to solve the three-dimensional potential distribution about a point source of direct current located in or on the surface of a half-space containing 2-D conductivity structure. STOYER and GREENFIELD [1976] worked out the response of a 2-D earth to an oscillating magnetic dipole source in this way. However, their general formulation can be applied to electric dipole sources.

* Department of Geophysics, Technical University for Heavy Industry, Miskolc, Egyetemváros, H–3515, Hungary

Paper presented at the 31st International Geophysical Symposium, Gdansk, 30 September–3 October, 1986

2. Mathematical formulation

The basic relationships governing this electromagnetic phenomenon are Maxwell's equations. Assuming only $e^{j\omega t}$ time dependent electric source they are:

$$\text{rot } \vec{E} = -j\omega\mu\vec{H} \quad (1)$$
$$\text{rot } \vec{H} = (\sigma + j\omega\varepsilon)\vec{E} + \vec{i}_s \quad (2)$$

where $\vec{i}_s$ is the current density. If equations (1), (2) are reduced to components in the x, y, z directions the Fourier transforms of the equations can be determined over the strike direction (x). If G denotes any component of $\vec{E}$ or $\vec{H}$ the Fourier transform of G over x is:

$$\tilde{G}(k_x, y, z) = \int_{-\infty}^{x} G(x, y, z)e^{-jk_x x}\,dx \quad (3)$$

The Fourier transform of the function $\frac{\partial G}{\partial x}$ over x is $(-jk_x)$ times $\tilde{G}(k_x, y, z)$ because $G(x, y, z)$ vanishes as $x \to \pm\infty$ if the source is placed to the origin of the Cartesian system of coordinates. Taking into consideration the above-mentioned relationships and assuming only an electric source parallel to the strike the densest form of the Fourier transform of the component equations (1), (2) is:

$$-\frac{\partial}{\partial y}\left(\frac{1}{\vartheta^M}\frac{\partial \tilde{H}_x}{\partial y}\right) - \frac{\partial}{\partial z}\left(\frac{1}{\vartheta^M}\frac{\partial \tilde{H}_x}{\partial z}\right) - jk_x\frac{\partial \xi}{\partial y}\frac{\partial \tilde{E}_x}{\partial z} + jk_x\frac{\partial \xi}{\partial z}\frac{\partial \tilde{E}_x}{\partial y} + \gamma^M\tilde{H}_x = 0 \quad (4)$$

$$-\frac{\partial}{\partial y}\left(\frac{1}{\vartheta^E}\frac{\partial \tilde{E}_x}{\partial y}\right) - \frac{\partial}{\partial z}\left(\frac{1}{\vartheta^E}\frac{\partial \tilde{E}_x}{\partial z}\right) + jk_x\frac{\partial \xi}{\partial y}\frac{\partial \tilde{H}_x}{\partial z} - jk_x\frac{\partial \xi}{\partial z}\frac{\partial \tilde{H}_x}{\partial y} + \gamma^E\tilde{E}_x = -\tilde{i}_{sx} \quad (5)$$

Equations (4), (5) are called the Transverse Magnetic *(TM)* and the Transverse Electric *(TE)* equation, respectively. In these equations $\tilde{H}_x$, $\tilde{E}_x$ are the Fourier transforms of H_x and E_x over x; $\tilde{i}_{sx}$ is the Fourier transform of the electric source term in the strike direction. If k denotes the wavenumber, ξ, *TM* admittance, *TE* impedance, *TE* admittance, *TM* impedance can be defined after STOYER [1974] in the following way: $\xi = (k_x^2 - k^2)^{-1}$; $\gamma^M = j\omega\mu$; $\vartheta^E = (1 - k_x^2/k^2)\gamma^M$; $\gamma^E = (\sigma + j\omega\varepsilon)$; $\vartheta^M = (1 - k_x^2/k^2)\gamma^E$. These parameters are constant within each grid element *(Fig. 1)*.

Without solving the coupled partial differential equations (4), (5) it is easy to see that $\tilde{E}_x(k_x, y, z)$ must be even in k_x and $\tilde{H}_x(k_x, y, z)$ must be odd in k_x. To verify the assertion above observe that $\tilde{i}_{sx}$ is an even function in k_x on the right side of equation (5). Therefore the superposition of terms occurring on the right side of equation (5) must be even in k_x as well. It follows from this that each term on the right side of equation (5) must be even in k_x. It is possible if and only if function $\tilde{E}_x(k_x, y, z)$ is even and function $\tilde{H}_x(k_x, y, z)$ is odd in k_x. In order to get the solution in the space domain the solution of equations (4),

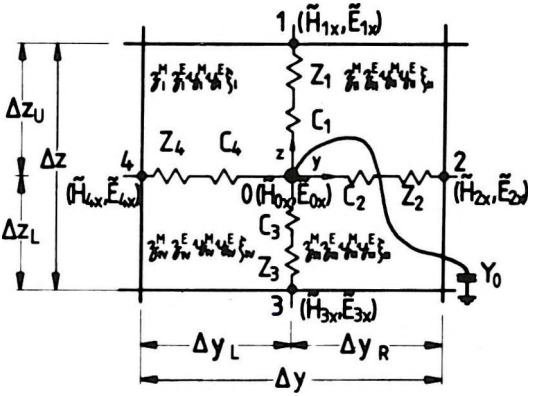

Fig. 1. Grid element of two-dimensional conductivity model in the (k_x, y, z) domain

1. ábra. Kétdimenziós vezetőképesség modell elektromos szimulációjának részlete a (k_x, y, z) tartományban

Рис. 1. Фрагмент электрического боспроизведения двумерной модели электропроводности области (k_x, y, z).

(5) is to be inverse Fourier transformed. This transformation for the plane which is perpendicular to the strike and contains the source becomes simple because $x=0$. This fact further simplifies the inverse Fourier transformations:

$$E_x(0, y, z) = \frac{1}{\pi} \int_0^\infty \tilde{E}_x(k_x, y, z)\, \mathrm{d}k_x \tag{6}$$

$$H_x(0, y, z) = 0 \tag{7}$$

For a source-free area $\tilde{H}_y$, $\tilde{H}_z$, $\tilde{E}_y$, $\tilde{E}_z$ can be expressed as a function of $\tilde{E}_x$ and $\tilde{H}_x$. These are used for calculating the other components of the field:

$$H_y(0, y, z) = \frac{1}{\pi} \int_0^\infty \left(\frac{-\dfrac{\partial \tilde{E}_x}{\partial z}}{(1 - k_x^2/k^2)\mathrm{j}\omega\mu} - \frac{\mathrm{j}k_x}{(k_x^2 - k^2)} \frac{\partial \tilde{H}_x}{\partial y} \right) \mathrm{d}k_x \tag{8}$$

$$H_z(0, y, z) = \frac{1}{\pi} \int_0^\infty \left(\frac{\dfrac{\partial \tilde{E}_x}{\partial y}}{(1 - k_x^2/k^2)\mathrm{j}\omega\mu} - \frac{\mathrm{j}k_x}{(k_x^2 - k^2)} \frac{\partial \tilde{H}_x}{\partial z} \right) \mathrm{d}k_x \tag{9}$$

$$E_y(0, y, z) = 0 \tag{10}$$

$$E_z(0, y, z) = 0 \tag{11}$$

3. Numerical process

As has already been pointed out the numerical procedure utilized is the finite difference method. The coupled partial differential equations have been given in (4), (5). The next step is to discretize them over a rectangular net.

3.1 Structure of the system of equations

Using a three-point difference operator for the second derivative and averaging each term on the left-hand side over the four quarter blocks surrounding a central node, the final form of the finite difference equations is:

$$\sum_{i=1}^{4} p_i \left[\frac{\tilde{H}_{ix} - \tilde{H}_{ox}}{-Z_i^M} + \frac{\tilde{E}_{ix} - \tilde{E}_{ox}}{C_i} \right] + Y_o^M \tilde{H}_{ox} = 0 \tag{12}$$

$$\sum_{i=1}^{4} p_i \left[\frac{\tilde{E}_{ix} - \tilde{E}_{ox}}{-Z_i^E} - \frac{\tilde{H}_{ix} - \tilde{H}_{ox}}{C_i} \right] + Y_o^E \tilde{E}_{ox} = -\tilde{I}_{sox} \Delta y \Delta z \tag{13}$$

where Z denotes lumped impedances, C denotes coupling terms between the central and one of the four neighbouring nodes, and Y denotes lumped admittances (Fig. 1). Similarly to 2-D magnetotellurics the lumped impedances are the parallel combinations of the impedances of two adjacent elements, and the lumped admittances are the parallel combinations of the admittances of the four elements surrounding a node.

The reciprocal values of coupling terms – which do not occur in magnetotellurics – are directly proportional to values ξ of the adjacent elements and are independent of the size of elements. For example Z_1^M, C_1 and Y_o^M can be given by the formulae:

$$\frac{1}{Z_1^M} = \frac{2}{\Delta z_U} \left(\frac{\Delta y_R}{\vartheta_{II}^M} + \frac{\Delta y_L}{\vartheta_I^M} \right) \tag{14}$$

$$\frac{1}{C_1} = 2 \mathrm{j} k_x (\xi_I - \xi_{II}) \tag{15}$$

$$Y_0^M = \Delta y_L \Delta z_U \vartheta_I^M + \Delta y_R \Delta z_U \vartheta_{II}^M + \Delta y_R \Delta z_L \vartheta_{III}^M + \Delta y_L \Delta z_L \vartheta_{IV}^M \tag{16}$$

Using a Neumann-type boundary condition in equations (12) and (13), $p_i = 0$ if point P_i is outside the grid, and $p_i = 1$ in any other case. If we use a terminal-impedance type boundary condition, i.e. the edge of the mesh is grounded, the outward-directed lumped impedances are a fraction of the inward-directed lumped impedances. This can be accomplished by a suitable choice of p_i. In equation (13) $\tilde{I}_{sox}$ is the Fourier transform of the strike directional electric source term in finite difference form. The sources can be treated like distributed parameters [Stoyer 1974]. Oscillating electric dipoles are treated as

point sources in the strike direction. If their lengths were finite in the strike direction, the Fourier transforms of sources would be oscillating functions in k_x. The strike directional source term on the surface is treated as a Heaviside function in the two adjacent quarter elements situated below the surface *(Fig. 2)*. The treatment above makes it possible to determine the Fourier transform of the electric source placed in the strike direction:

$$\tilde{i}_{sox} \approx \frac{1}{\frac{\Delta y_L}{2} \cdot \frac{\Delta z_L}{2}} \int_{z_0 - \frac{\Delta z_L}{2}}^{z_0} \int_{y_0 - \frac{\Delta y_L}{2}}^{y_0 + \frac{\Delta y_R}{2}} \tilde{i}_{sx} \, dy \, dz = \int_{-\infty}^{\infty} i_{sx} \delta(x) \, e^{-jk_x x} \, dx = i_{sx} \qquad (17)$$

It means that there is only one node that has a source term different from zero, and it is equal to the applied electric source.

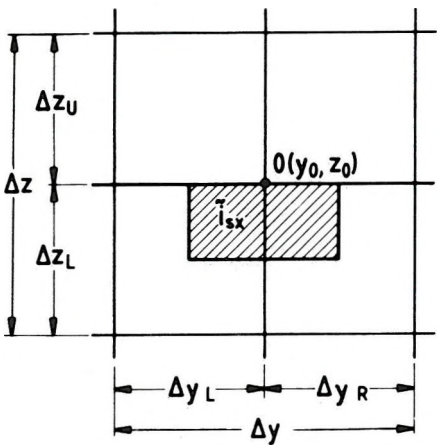

Fig. 2. Treatment of an electric source in strike direction on the surface

2. ábra. Felszínen levő, csapásirányú elektromos dipólus egyszerűsített vázlaza

Рис. 2. Упрощенная схема электрического диполя, параллельного простиранию и находящегося на поверхности.

After decomposition of finite difference equations (12), (13) to equations containing either real (R) or imaginary (I) terms we get four (TM_R, TM_I, TE_R, TE_I) equations belonging to a node. Progressing column-wise on the grid nodes from left to right and writing the equations successively the resulting linear set of equations has the form *(Fig. 3)*

$$[Q] \vec{X} = \vec{S} \qquad (18)$$

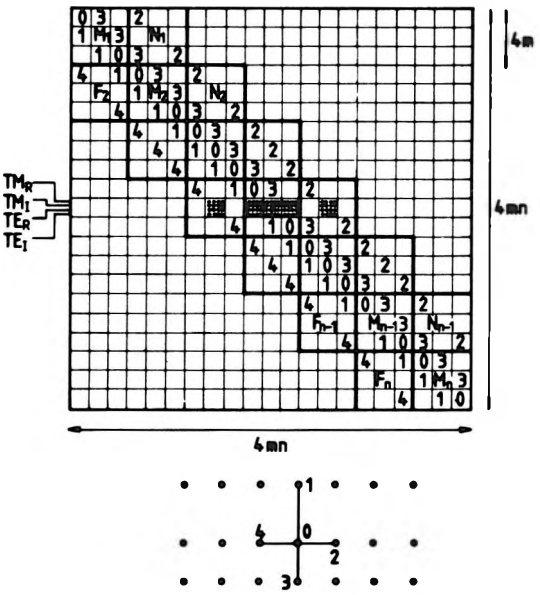

Fig. 3. Structure of a coefficient matrix belonging to a grid with three rows and seven columns

3. ábra. Három sorból és hét oszlopból álló rácshoz tartozó együtthatómátrix szerkezete

Рис. 3. Структура матричного коэффициента, принадлежащего сетке, состоящей из трех строчек и семи граф.

Coefficient matrix $[Q]$ has a band structure, it is a square and non-symmetrical matrix; $\vec{X}$ is the column vector of unknowns containing the components in the order of $\tilde{H}_x^R$, $\tilde{H}_x^I$, $\tilde{E}_x^R$, $\tilde{E}_x^I$; $\vec{S}$ is a column vector containing the Fourier transforms of source terms in finite difference form belonging to TM_R, TM_I, TE_R, TE_I equations. If we use a Neumann-type or terminal-impedance type boundary condition, $[Q]$ has a blocked-tridiagonal structure as well. If the grid has m rows and n columns and m is smaller than n it is worth numbering the nodes column-wise, because the size of blocks and $[Q]$ can be partitioned in the form:

$$[Q] = \{[F]_l[M]_l[N]_l\}_1^n = [L][U] \tag{19}$$

where l denotes the number of the actual column, $[F]_l$ and $[N]_l$ are co-diagonal blocks, and $[M]_l$ represents main diagonal blocks. Each block has $4m.4m$ elements. Vectors $\vec{X}$ and $\vec{S}$ can be partitioned in the same manner: $\vec{X}_l$ and $\vec{S}_l$ belong to column l.

3.2 Solution of the set of equations

SCHECHTER [1960] suggested a reduction of Q to the form shown in equation (19) where L and U are square matrices, partitioned in the same manner as $[Q]$, of the form

$$[L] = \{[C]_l [I]_l [0]\}_1^n \tag{20}$$

$$[U] = \{[0][A]_l [N]_l\}_1^n \tag{21}$$

where $[I]_l$ denotes unit matrix.

From equations (19), (20), (21) $[A]_l$ may be determined recursively:

$$[A]_1 = [M]_1 \tag{22}$$

$$[A]_l = [M]_l - [F]_l [A]_{l-1}^{-1} [N]_{l-1} \qquad l = 2, 3, \ldots . n. \tag{23}$$

Introducing $[U]\vec{X} = \vec{V}$ the first step is to solve $[L]\vec{V} = \vec{S}$. Its solution may be obtained recursively too:

$$\vec{V}_1 = \vec{S}_1 \tag{24}$$

$$\vec{V}_l = \vec{S}_l - [F]_l [A]_{l-1}^{-1} \vec{V}_{l-1} \qquad l = 2, 3, \ldots, n. \tag{25}$$

The solution of $[U]\vec{X} = \vec{V}$ is equal to those of (18):

$$\vec{X}_n = [A]_n^{-1} \vec{V}_n \tag{26}$$

$$\vec{X}_l = [A]_l^{-1} (\vec{V}_l - [N]_l \vec{X}_{l+1}) \qquad l = n-1, n-2, \ldots, 2, 1 \tag{27}$$

Using the same geoelectric section and frequency with the same grid size but having another source position or another type of source ($\vec{R}$) one has only to change in the source terms of equations (24), (25):

$$\vec{V}_1 = \vec{R}_1 \tag{28}$$

$$\vec{V}_l = \vec{R}_l - [F]_l [A]_{l-1}^{-1} \vec{V}_{l-1} \qquad l = 2, 3, \ldots, n. \tag{29}$$

The advantage of this decomposition is obvious from the above: it reduces the $4mn.4mn$ matrix ($[Q]$) inversion to n $4m.4m$ matrix ($[A]_l$) inversions.

This direct method was applied to solve that part of the problem related to the homogeneous half-space. We were restricted to the case of $k_x = 0$. The frequency 20 kHz, the grid 12 by 25 nodes, and the conductivity of the earth was 0.01 mho/meter. The number of unknowns is 1200. The distribution of the absolute value of strike directional electric field in Vm^{-1} and the structure of the grid are illustrated in *Figure 4*. The source was placed on the surface (6th row) and into the 13th column, its current intensity was 10 A. The smallest grid elements, having a length of 5m and a width of 5m, are next to the source.

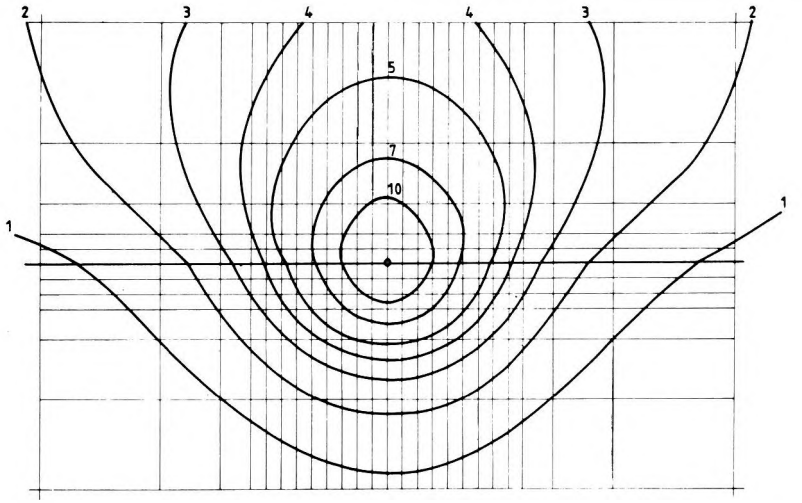

Fig. 4. Distribution of Fourier transformed strike directional field component in V/m

4. ábra. Csapásirányú elektromos térkomponens Fourier transzformáltjának izovonalas térképe V/m-ben

Рис. 4. Карта изолиний V/m трансформата Фурье электрической компоненты поля, параллельной простиранию.

3.3 Planning of wavenumber domain

The set of equations (18) has to be solved for different k_x values. The simultaneous aim is to compute for as few k_x values as possible and to achieve suitable accuracy. For this reason the number and the distribution of discrete spatial wavenumbers need to be planned. They depend upon the geoelectric and geometric parameters of structures, the frequency and the transmitter–receiver arrangement. We can only plan for 1—D geoelectric sections. The electromagnetic field of an electric dipole source placed on a homogeneous or a layered half-space can be computed for a line which is parallel to the strike direction and is situated on the surface. After this these functions are to be Fourier transformed over x. In order to get accurate space domain values by inverse Fourier transformation for $x=0$, we have to choose the appropriate number and distribution of k_x values. *Figure 5* shows the Fourier transforms of strike directional electric field components computed numerically from the space domain values over half-spaces of different conductivity [TAKÁCS 1983]. Assuming a horizontal electric dipole source in the x direction on the surface, the electric field has been determined for the line which is parallel to the x-direction and is situated 900 metres from the source on the surface. The current intensity of the source is 1 A. Formulae derived by BANNISTER and DUBE [1978] allow ready computation of these functions. The Fourier transform of component E_x

with indices 1, 2, 3 refers to $\varrho_1 = 190\ \Omega$m, $f_1 = 800$ Hz; $\varrho_2 = 24\ \Omega$m, $f_2 = 244$ Hz; $\varrho_3 = 60\ \Omega$m, $f_3 = 25$ Hz, respectively. Subsequent inverse Fourier transformation showed that the 13 k_x values selected logarithmically in the range of $0 < k_x \leqq \leqq 1.648 \cdot 10^{-3}\ \mathrm{m}^{-1}$ were sufficient to achieve an accuracy within 1% in the $x = 0$ plane. In this way, if we have a 2-D inhomogeneity embedded in a 1-D structure, we can determine approximately for which k_x values the set of equations is to be solved.

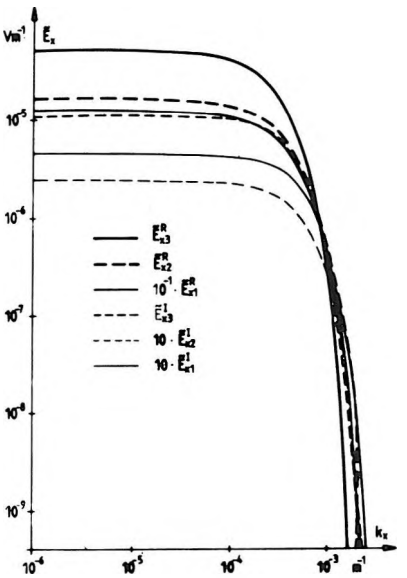

Fig. 5. Fourier transforms of strike directional electric field components over a half-space computed for a line parallel to the source in the strike direction

5. ábra. Csapásirányú mos dipólus csapásirányú mos tér komponenseinek Fourier transzformáltjai forrással párhuzamos felszíni vonal mentén homogén féltér esetén

Рис. 5. Трансформаты Фурье электрической компоненты поля, параллельной простиранию, над однородным полупространством, рассчитанные вдоль линии, параллельной источнику вдоль простирания.

4. Conclusions

Earlier the response of a 2-D earth to an oscillating magnetic dipole source was investigated. The present work describes a numerical method which makes it possible to determine the electromagnetic field of an oscillating electric dipole source placed on a 2-D earth. The electric source is parallel to the strike and it is treated as a point source. The result of a parity test is taken into consideration to determine the field components for the plane which is perpendicular to the strike and contains the source. The algorithm worked out by SCHECHTER has been applied to find the solution to the set of equations. On the basis of the numerical calculations the spatial wavenumber domains to be considered are equal under the condition of constant transmitter–receiver distance.

Acknowledgements

The author is indebted to Professor E. Takács who made it possible for him to work on this theme. Computation work on a CDC 3300 was financially supported by the Geophysical Department of the Technical University for Heavy Industry, Miskolc.

REFERENCES

BANNISTER P. R., DUBE R. L. 1978: Simple expressions for horizontal electric dipole quasi-static range subsurface-to-subsurface and subsurface-to-air propagation. Radio Science, **13,** 3, pp. 501–507

DEY A., MORRISON H. F. 1979: Resistivity modelling for arbitrarily shaped two-dimensional structures. Geophysical Prospecting, **27,** 1, pp. 106–136

SCHECHTER S. 1960: Quasi-tridiagonal matrices and type-insensitive difference equations. Quart. Appl. Math., **18,** 3, pp. 285–295

STOYER C. H. 1974: Numerical solutions of the response of a two-dimensional earth to an oscillating magnetic dipole source with application to a groundwater field study. Ph.D. thesis, Pennsylvania State University

STOYER C. H., GREENFIELD R. J. 1976: Numerical solutions of the response of a two-dimensional earth to an oscillating magnetic dipole source. Geophysics, **41,** 3, pp. 519–530

TAKÁCS E. 1983: Development of EM theoretical methods (in Hungarian). NME report, pp. 30–41

MEGJEGYZÉSEK AZ OSZCILLÁLÓ ELEKTROMOS DIPÓLUS FORRÁS ELEKTROMÁGNESES TERÉNEK NUMERIKUS MODELLEZÉSÉHEZ

PETHŐ Gábor

Harmonikus, időtől függő, csapásiránnyal párhuzamos elektromos forrást feltételezve a cikk a csapásirányra merőleges, a forrást tartalmazó sík elektromágneses terének meghatározásával foglalkozik. Az alkalmazott numerikus eljárás a véges differenciák módszere. Az együttható mátrix blokktridiagonális szerkezetét figyelembe vevő direkt módszert javasolja a kapott lineáris egyenletrendszer megoldására. Számos térbeli hullámszámra megoldva az egyenletrendszert, a térkomponenseket inverz Fourier transzformáció segítségével határozza meg numerikusan. A diszkrét térbeli hullámszámok számát és eloszlását meg kell tervezni. Ezt az eljárást egy példán keresztül mutatja be.

ЦИФРОВОЕ МОДЕЛИРОВАНИЕ ЭЛЕКТРОМАГНИТНОГО ПОЛЯ ДВУМЕРНОГО КАЧАЮЩЕГОСЯ ЭЛЕКТРИЧЕСКОГО ДИПОЛЯ

Габор ПЕТЭ

В статье рассматривается определение электромагнитного поля плоскости, перпендикулярной простиранию и проходящей через источник, предполагая гармонический электрический источник, параллельный структурному простиранию и зависящий от времени. Применяется цифровой метод — способ конечных разностей. Для решения полученной линейной системы рекомендуется прямой метод, учитывающий блоковую, тридиагональную структуру матричного коэффициента. Вслед за решением системы уравнений нескольких объемных волновых чисел полевые компоненты определяются в цифровом виде, с помощью обратных трансформатов Фурье. Необходимо запланировать распределение и количество дискретных объемных волновых чисел, что́ иллюстрируется конкретным примером.

GEOPHYSICAL TRANSACTIONS 1987
Vol. 33. No. 2. pp. 123–130

ANALYSIS OF SEVERAL FEATURES OF RESPONSE FUNCTIONS OF FREQUENCY SOUNDINGS OVER H- AND K-TYPE MODELS

Gábor SZIGETI*

A simple three-layer model is examined for a better understanding of the exploration potential of frequency sounding. A clear condition for the screening effect of the intermediate layer, as well as the exact condition of equivalence for the thin layers and their simplified description are obtained by an asymptotic estimate, related to the parameters of the intermediate layer.

Keywords: frequency sounding, equivalence, screening, electromagnetic field, one-dimensional model

1. Introduction

The frequency sounding method significantly increased the possibilities of surface geoelectric exploration. The interpretation of frequency soundings renders the calculation of the electromagnetic field over a horizontally layered medium essential. In order to facilitate the vertical magnetic dipole-source, transition zone frequency sounding work carried out at ELGI a computer program-package was developed to compute response curves for the layered half-space [PRÁCSER et al. 1982]. Thus, a possiblity is given for the purely numerical analysis of the effect of changes in model parameters on the sounding curves. However, questions of the solvability of the geological problem, survey planning and quality of interpretation make it necessary —besides the numerical study of the curve-behaviour— to have as clear view as possible of the dependence of sounding curves on layer parameters.

Such a view may be obtained by the asymptotic analysis of computational formulae of quite simple models. A layer embedded in a homogeneous half-space is examined by such a method in this paper and simple, suggestive pictures describing the effect of that layer are presented in two cases. In the first case the layer is thick and conductive so it screens the underlying formation. The second case is the asymptotic one, when the layer is thin, having only a slight resistivity difference compared with the surroundings and its effect is proportional to its thickness resistivity-difference product.

The validity-domain of the simple rules obtained by the asymptotic estimation is to be controlled because the inequalities determining the above domain could not be fully analysed due to the complexity of the formulae describing the phenomenon of induction.

* Eötvös Loránd Geophysical Institute of Hungary, POB 35, Budapest, H–1440
Manuscript received: 13 July, 1987

However, this is not identical with the empirical study of the effect of parameters. Let us see it through the example of equivalence. Equivalent models may be found by computing numerous models. Knowing the deduction of the thin layer case it is given how model pairs considered to be equivalent should be chosen, only the question whether the models satisfy the conditions of the deduction needs to be checked. It is difficult to check the latter, so we test the equivalence of the model pair.

2. Computational formulae of EM field

Let us place a layer of ϱ_2 resistivity and d thickness into a homogeneous half-space of ϱ_1 resistivity at the depth h (*Fig. 1*). The model is type K if $\varrho_2 > \varrho_1$, and type H if $\varrho_2 < \varrho_1$.

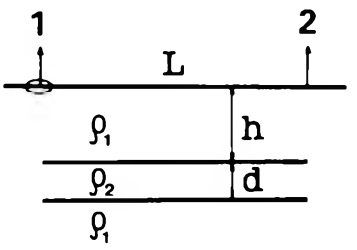

Fig. 1. Parameters of our geoelectric model containing an interbedded layer
1 – transmitter; 2 – receiver

1. ábra. A vizsgált, betelepült réteget tartalmazó geoelektromos modell paraméterei
1 – adó; 2 – vevő

Рис. 1. Параметры геоэлектрического разреза с исследуемым средним слоем: 1 – передатчик, 2 – приемник.

The two functions to be presented below concern all electromagnetic components over the three-layer model, but for brevity's sake only the H_z component is deduced now.

Using the formulae and symbols of PRÁCSER et al. [1982] for the n-layer model, the $H_z^{(a)}$ differential component — this is the deviation of the EM field existing over the layered half-space from the field over the homogeneous half-space — may be written as follows:

$$H_z^{(a)} = \frac{9IS}{2\pi i\omega\mu\sigma_1 L^5}\left\{\frac{2}{9}r^5 \int_0^\infty \frac{\beta_1 b_1}{\frac{t+\beta_1}{t-\beta_1}+b_1}\, t^3\, J_0(r\ t)\,\mathrm{d}t\right\}. \qquad (1)$$

The more important parameters are:

μ magnetic permeability
IS moment of transmitter
ω frequency of transmitter
L transmitter–receiver distance, $r = L/h$
t variable of Hankel transform

$$\beta_j = \sqrt{t^2 - 2iB_j^2\left(\frac{h}{L}\right)^2}, \quad \operatorname{Re}\beta_j \geq 0$$

$$B_j = L/\delta_j; \quad \delta_j = \sqrt{\frac{2}{\omega\mu\sigma_j}}; \quad \sigma_j = 1/\varrho_j \quad \text{for} \quad j = 1, 2, 3$$

and let us denote B_1 by B. The recursively defined b_1 quantity may be arranged into the following formula, taking it into account that $\beta_1 = \beta_3$:

$$b_1 = \frac{a(\beta_1^2 - \beta_2^2)}{2\beta_1\beta_2 + a(\beta_1^2 + \beta_2^2)} e^{-2\beta_1} \tag{2}$$

where

$$a = \operatorname{th}\left(\frac{d}{h}\beta_2\right) = \operatorname{th}(z).$$

3. Deduction of condition of screening

It is easy to see, that if $\operatorname{Re}(Z) \geq 1.47$ then $\operatorname{th}(Z) \cong 1$ (10% accuracy). Thus, if for $Z = \frac{d}{h} \cdot \beta_2$ it is true then $H_z^{(a)}$ is independent of the thickness d of the intermediate layer, because the $\varphi(t) = \varphi(t, a)$ kernel function of expression (1) uniformly converges to the function $\varphi(t, 1)$ over any $0 \leq t \leq T$ interval, if $a \to 1$.

On the basis of the following estimate to fulfil $\operatorname{Re}(d/h \cdot \beta_2) \geq 1.47$ a satisfactory condition which is independent of t is

$$\frac{d}{h}\operatorname{Re}\left(\sqrt{t^2 - 2iB_2^2\left(\frac{h}{L}\right)^2}\right) \geq \frac{d}{h}\sqrt{2B_2^2\left(\frac{h}{L}\right)^2}\frac{1}{\sqrt{2}} = \frac{d}{L}B_2 =$$

$$= \frac{d}{L}B\sqrt{\frac{\sigma_2}{\sigma_1}} \geq 1.47. \tag{3}$$

Thus, if B, L and σ_1 are given and the parameters of the intermediate layer fulfil inequality (3) then an increasing d does not affect $H_z^{(a)}$; that is, in this type of H and K model no information is given about the bottom of the intermediate layer. If Eq. (3) is fulfilled in the whole induction number-domain then even the whole sounding curve does not "sense" the bottom of the intermediate layer. If it is accepted as true that a layer of smaller resistivity contrast or of greater depth causes a smaller effect then no information is obtained not only about the bottom of the second layer that satisfies Eq. (3) but also about the layers below it even if the third layer is a multilayered, inhomogeneous medium whose maximum resistivity contrast compared with σ_1 does not exceed the contrast of σ_1 and σ_2. Inequality (3) is satisfied if d/L is great or σ_2 is great, for given B,

L, σ_1. However, the fact that no information may be gained from below a layer of about L thickness is well-known, independently of this deduction, so the screening becomes interesting when $\sigma_2 \gg \sigma_1$.

It is also known [e.g. MUNDRY and BLOHM 1986] that frequency sounding gives no information from below a sufficiently conductive layer. Inequality (3) gives the quantitative meaning of "sufficiently" and shows how screening should be interpreted.

Estimate (3) is independent of the depth of the intermediate layer. An infinitely thin and ideally conductive plate really acts as a screen independently of its depth because the EM field does not penetrate through it. So the question arises concerning the extent to which the screening effect of the intermediate, not infinitely thin and not ideally conductive plate is independent of its depth, i.e. of h/L. In other words, the questions are: how sharp is estimate (3), e.g. in the case of fixed L, B, σ_2, σ_1 and h how great is the interval d in which — though the estimate is not realized — the layer still acts as a screen.

These questions were examined by numerical computation. It is also assumed that $h/L \geq 0.2$, since B_1 is involved in Eq. (3), but the induction number should be matched to the resistivity of the first layer only if it is not too thin. By means of $B = 1, 3, 6$ and 9 values for $h/L = 0.2$ and 0.4, studies were carried out to determine the lowest d^*/L value for which, if it is increased, the $H_z^{(a)}$ anomalous field only slightly changes (10%). This d^*/L value proved to be nearly the same for the two h/L values, and this value is involved in the upper lines of *Table I*. Estimates on the basis of Eq. (3) are found in the bottom line. The

M	B			
	1	3	6	9
H–5	(x) (x)	0.15 0.22	0.08 0.11	0.05 0.07
H–10	0.35 0.47	0.12 0.16	0.06 0.08	0.05 0.05
H–50	0.12 0.21	0.06 0.07	0.03 0.03	0.02 0.02

Table I. Smallest d^*/L thicknesses of the *interbedded* layer necessary to behave as a screen for type H models. Upper values were obtained by a numerical program computing the field, lower values were given by estimate (3). B is the induction number, M is the identifier of the model

I. táblázat. H típusú modellben a betelepült réteg árnyékolóként való viselkedéséhez szükséges legkisebb d^*/L vastagságot tartalmazó táblázat. A felső sor a numerikus térszámoló programmal kapott, az alsó pedig (3) becslés alapján meghatározott értékeket mutatja. B az indukciószám, M a modell azonosítója

Таблица I. Минимальные мощности d^*/L, необходимые для поведения среднего слоя разреза типа H в качестве экранирующего: в верхней строке приведены значения, полученные программой численного определения поля, а в нижней — по оценке (3); B — индукционное число, M — обозначение разреза.

values where $d^*/L > 0.5$ are marked by a star, because there the estimate is meaningless since the resolution power of frequency sounding rapidly decreases below the depth of $h + d \geq 0.7\,L$. Thus, the more interesting part of the table is where the thin layers are involved. For $\sigma_2/\sigma_1 = 50$ no information is obtained from below a layer of $d/L = 0.2$ thickness, being at a depth greater than $0.2\,L$, as shown by the last line. The relative closeness of the values in the top and bottom lines of Table I. demonstrates the quality of estimate (3). The estimate is less sharp for small B and h values, as may also be deduced from the discussion of the uniform convergence of the $\varphi(t, a)$ function due to "a".

4. Effect of thin layer

Let us assume

$$\left| \frac{d}{h} \beta_2 \right| \ll 1 \tag{4}$$

and so the th(z) function may be approximated by z in (2), that is

$$b_1 = \frac{\frac{d}{h}(\beta_1^2 - \beta_2^2)}{2\beta_1 + \frac{d}{h}(\beta_1^2 + \beta_2^2)} e^{-2\beta_1}$$

If it is also assumed that

$$\left| \frac{d}{h} \beta_1^2 \right| \ll |\beta_1| \tag{5}$$

and

$$\left| \frac{d}{h} \beta_2^2 \right| \ll |\beta_1| \tag{6}$$

then

$$b_1 = \frac{\frac{d}{h}(\beta_1^2 - \beta_2^2)}{2\beta_1} e^{-2\beta_1} = \frac{\frac{d}{h}(\sigma_2 - \sigma_1) i\omega\mu h^2}{2\beta_1} e^{-2\beta_1}. \tag{7}$$

When substituting this formula of b_1 to Eq. (1) the second term in the denominator of the kernel function may be neglected, because due to $\mathrm{Re}\,\beta_1 \geq 0$:

$$\left| \frac{t + \beta_1}{t - \beta_1} \right| > 1.$$

(In the geometrical representation of complex values here the longer diagonal of the parallelogram is in the numerator.) On the basis of Eqs. (5) and (6), further of $|e^{-2\beta_1}| < 1$, from Eq. (7) follows that $b_1 \ll 1$.

Thus, substituting into Eq. (1) the form of b_1 into Eq. (7) we get

$$H_z^{(a)} = \frac{IS}{2\pi}\frac{1}{h^3}\frac{\sigma_2-\sigma_1}{\sigma_1}\frac{d}{h}\int_0^\infty \frac{t-\beta_1}{t+\beta_1} t^3 e^{-2\beta_1} J_0(rt)\,dt. \tag{8}$$

The importance of (8) is given by the fact that the integral already does not contain d and σ_2 parameters of the intermediate layer, so it is a clear form of the description of intermediate layers fulfilling conditions (4), (5) and (6). At first glance conditions (5) and (6) appear to be never satisfied, because integration parameter t — which varies between zero and infinity — is at the power of two on the left side of the inequality, while it is at the first power on the right side. However, the kernel function of expression (1) is of 0 (e^{-t}) order [SZIGETI 1983], so — because d is involved only on the left side of the inequalities — there always exists an adequately small d'/L that (4), (5) and (6) are satisfied for every $d \leq d'$ values by arbitrary values of B, σ_2/σ_1 and h/L. Further, it can be seen from the above discussion that d' is greater when B is smaller, and σ_2 is close to σ_1.

Presenting a simpler summing of the result it may be said that for given σ_1 and L the anomalous field of a thin layer is proportional to its thickness conductivity difference (in relation to the surroundings) product, i.e. it may be written in the form:

$$H_z^{(a)} = d(\sigma_2-\sigma_1)\quad G_z(B,h). \tag{9}$$

Thus we have obtained the condition of equivalence for H and K type models containing a thin layer: at given σ_1 and L, layers of parameters d', σ_2', and d'', σ_2'' being at equal depths cause equal effects at induction number B, if

$$d'(\sigma_2'-\sigma_1) = d''(\sigma_2''-\sigma_1) \tag{10}$$

PATRA and MALLICK [1980] have examined intermediate layers of greater thickness than those of conditions (4), (5) and (6). According to these authors the condition of equivalence is $d\sigma_2^2 = \text{const}$ for model H, and $d/\sqrt{\sigma_2} = \text{const}$ for model K. Details of the connection between these two results require further study.

Expression (9) calls attention to the important difference between the effect of the H and K type intermediate layers, because if H^α stands for $\sigma_2'/\sigma_1 = \alpha > 1$ and K^β stands for $\sigma_1/\sigma_2'' = \beta > 1$ then to get an effect of the same amplitude but opposite sign in the case of $\alpha = \beta$, and layer thickness d in model H a layer thickness of x is needed in model K, where

$$d'(\alpha\sigma_1-\sigma_1) = d''\left|\frac{\sigma_1}{\alpha}-\sigma_1\right|$$

and so

$$d'' = \alpha d'$$

i.e. an α times thicker intermediate layer is necessary in model K. Instead of the

H_z quantity the behaviour of the $R = (H_z/H_r)$ ratio — which is measured on the field — is studied by computer calculations in *Fig. 2* for H^α and K^β intermediate layers in the $1 \leq \alpha_1, \beta \leq 10$ interval by $B = 1$ induction number and $h/L = 1/3$ values. Quantity d/L — relative thickness of the layer — is on the horizontal axis, and the relative deviation of the R ratio of the given model from that of the half-space model is on the vertical axis.

The steepness of the curves belonging to different models and their deviation from the straight line show the approximate satisfaction of (8) and its inaccuracy. The graph is also valid in the whole $B \leq 1$ interval.

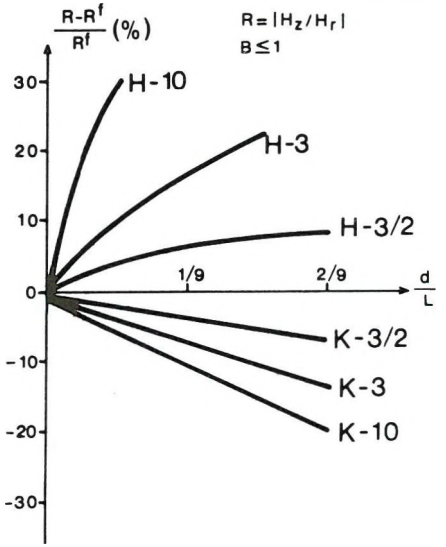

Fig. 2. Deviations of the low frequency part of the $|H_z/H_r|$ ratio from the homogeneous model (in per cent) for interbedded layers of different parameters

2. ábra. $|H_z/H_r|$ hányados alacsony frekvenciás részének homogén modelltől való százalékos eltérései különböző paraméterű betelepült rétegek esetére

Рис. 2. Процентные отклонения низкочастотной части отношения $|H_z/H_r|$ от однородной модели для различных параметров среднего слоя.

REFERENCES

MUNDRY E. and BLOHM E. K. 1986: Frequency electromagnetic sounding using a vertical magnetic dipole. Geophys. Prosp. **35**, 1, pp. 110–123

PATRA H. P. and MALLICK K. 1980: Geosounding Principles, 2. Time-Varying Geoelectric Sounding. Elsevier, 419 p.

PRÁCSER E., SZIGETI G., SZABADVÁRY L. 1982: Computation of multifrequency electromagnetic sounding curves. Annual Report of the Eötvös Loránd Geophysical Institute of Hungary for 1982, pp. 213–215

SZIGETI G. 1983: Numerical computation of frequency sounding curves (in Hungarian). ELGI Methodological Report 52 p.

FREKVENCIASZONDÁZÁS VÁLASZFÜGGVÉNYEI NÉHÁNY TULAJDONSÁGÁNAK VIZSGÁLATA H ÉS K TÍPUSÚ GEOELEKTROMOS MODELLEK ESETÉN

SZIGETI Gábor

Tanulmányunk tárgya az egyszerű háromréteges modell, a frekvenciaszondázás kutatási lehetőségeinek teljesebb megértése szempontjából. A modellt leíró képleteknek a második réteg paraméterei szerinti aszimptotikus vizsgálatával könnyen kezelhető feltételt kaptunk a középső réteg árnyékoló voltára, illetve a vékony réteg egyszerűsített leírásával megkaptuk ezen rétegek ekvivalenciájának pontos feltételét.

ИЗУЧЕНИЕ НЕКОТОРЫХ СВОЙСТВ ОТВЕТНЫХ ФУНКЦИЙ ЧАСТОТНОГО ЗОНДИРОВАНИЯ ДЛЯ СЛУЧАЯ ГЕОЭЛЕКТРИЧЕСКИХ РАЗРЕЗОВ ТИПА Н И К

Габор СИГЕТИ

Для более полного понимания возможностей частотного зондирования изучается простой трехслойный геоэлектрический разрез. Путем асимптотического исследования параметров второго слоя в уравнении, характеризующем данный разрез, можно получить ясное условие превращения среднего слоя в экранирующий, или же путем упрощенного описания тонкого слоя можно получить точное условие эквивалентности этих слоев.

GEOPHYSICAL TRANSACTIONS 1987
Vol. 33. No. 2. pp. 131–151

SPECIAL CROSSPLOTS PREPARED FROM WELL LOGS

Dénes SZENDRŐ*

Consideration of the standard deviations of logging values enables more accurate discussion of correlation connections from the point of view of probability theory. If one takes the log values to be probability variables the level of probability of their expected values to be in certain given intervals can be calculated by using the measured values and the standard deviations that are dependent on their derivatives. Representing this in a co-ordinate system, for two logs a two-dimensional average probability distribution is obtained whereas three logs give a weighted mean value distribution.

Compared with the conventional crossplot the cross-probability plot method developed is of a "filtered" character. Thus logging data near layer boundaries have less weight and parameters characterizing rock types can be determined by higher accuracy.

Keywords: well logging, interpretation, probability, standard deviation, crossplot, statistical distribution

1. Introduction

For the computer aided processing of well logs the crossplots reflecting the statistical and correlation connections between two or more well logs are of great significance. These representations allow the determination of the basic geophysical parameters dependent on the rock types as well as the estimation of their degrees of uncertainty and the reduction of systematic measuring and processing errors and the calibration of the mesurements. Apart from the inaccuracy of the instrument, the possible statistical behaviour of the measured quantity and the inaccuracy of the depth determination, in the conventional method all measurement data are considered with one numerical value, and the data pairs or the groups of three data relating to one depth point are always considered to be equally and absolutely related.

If few data are considered, it results in the values of the two-dimensional frequency distribution randomly fluctuating according to the degree of inaccuracy. If many data are considered then for thin layers the intervals characteristic for rock types merge into each other and cannot be separated. This results from the fact that for this method also the considerably varying parts of the log values, i.e. the environments of the layer boundaries, are equally considered as the constant parts of the log values (i.e. the points inside the layers). To investigate the more exact connections the theory of probabilities is discussed.

* Eötvös Loránd Geophysical Institute of Hungary, POB 35, Budapest, H–1440
Manuscript received: 14 November, 1986

2. Notations

CAL — caliper log
FID — density-porosity log
FIN — neutron-porosity log
GR — gamma ray log
i — index of the interval on the $\bar{X}$ axis of the co-ordinate system
I — number of intervals dividing the $\bar{X}$ axis of the co-ordinate system
j — index of the interval on the $\bar{Y}$ axis of the co-ordinate system
J — number of intervals dividing the $\bar{Y}$ axis of the co-ordinate system
l — index of the sampling point
L — number of sampling points
p_{ijl} — probability of the expected values of the x_l, y_l measured value pair to be in the S_{ij} interval
P_{ij} — average probability of the expected values of the measured value pairs to be in the S_{ij} interval
q_{il} — probability of the expected value of the measured value x_l to be in the ith interval
Q_i — average probability of the expected values of the measured values x_l ($l = 1, 2, \ldots, L$) to be in the lth interval
r_{jl} — probability of the expected value of the measured value y_l to be in the lth interval
R_j — average probability of the expected values of the measured values y_l ($l = 1, 2, \ldots L$) to be in the jth interval
ROB — density log
R10 — 10 cm normal resistivity log
R40 — 40 cm normal resistivity log
RTR — invert of the resistivity, i.e. the conductivity log
S_{ij} — interval of the co-ordinate system given by inequality (1)
SP — spontaneous potential log
X — log assigned to the $\bar{X}$ axis of the co-ordinate system
x_l — value of the X log in the lth sampling point
$\bar{X}$ — axis of the co-ordinate system
$\bar{x}_i$ — mean value of the ith interval of the $\bar{X}$ axis
Y — log assigned to the $\bar{Y}$ axis of the co-ordinate system
y_l — value of the Y log in the lth sampling point
$\bar{Y}$ — axis of the co-ordinate system
$\bar{y}_j$ — mean value of the jth interval of the $\bar{Y}$ axis
Z — log assigned to the $\bar{Z}$ axis of the co-ordinate system
z_l — value of the Z log in the lth sampling point
$\bar{Z}$ — axis of the co-ordinate system
$\bar{Z}_{ij}$ — weighted mean value assigned to the S_{ij} interval
$\bar{Z}_i^{(x)}$ — weighted mean value assigned to the ith interval of the $\bar{X}$ axis
$\bar{Z}_j^{(y)}$ — weighted mean value assigned to the jth interval of the $\bar{Y}$ axis

$\Delta\bar{x}$ — width of the intervals dividing the $\bar{X}$ axis
$\Delta\bar{y}$ — width of the intervals dividing the $\bar{Y}$ axis
σ_{ij} — standard deviation of the weighted mean value $\bar{Z}_{ij}$
$\sigma_i^{(x)}$ — standard deviation of the weighted mean value $\bar{Z}_i^{(x)}$
$\sigma_j^{(y)}$ — standard deviation of the weighted mean value $\bar{Z}_j^{(y)}$
σ_{xl} — standard deviation of log value x_l
σ_{yl} — standard deviation of log value y_l
σ_{zl} — standard deviation of log value z_l
ε_{x1} — parameter characterizing the absolute error of the X log
ε_{x2} — parameter characterizing the relative error of the X log
ε_{x3} — parameter characterizing the error dependent on the derivative of the X log
ε_{y1} — parameter characterizing the absolute error of the Y log
ε_{y2} — parameter characterizing the relative error of the Y log
ε_{y3} — parameter characterizing the error dependent on the derivative of the Y log
ε_{z1} — parameter characterizing the absolute error of the Z log
ε_{z2} — parameter characterizing the relative error of the Z log
ε_{z3} — parameter characterizing the error dependent on the derivative of the Z log

3. Formulation of the theory

For clarity let us see *Fig. 1*. Let the points plotted on the axis of the $\bar{X}$, $\bar{Y}$ rectangular co-ordinate system at equal distances $\Delta\bar{x}$ and $\Delta\bar{y}$ consecutively be $\bar{x}_i$ ($i = 1, 2, \ldots, I$) and $\bar{y}_j$ ($j = 1, 2, \ldots, J$). Let the values—measured at equal distances as a function of depth—of the X, Y logs examined as for the correlation connections consecutively be x_l, y_l, z_l ($l = 1, 2, \ldots, L$). The standard deviations of the log values for the lth sampling point are, consecutively, σ_{xl}, σ_{yl}, σ_{zl} ($l = 1, 2, \ldots, L$). Let us denote the rectangular domains of the co-ordinate system for which

$$\begin{aligned} \bar{x}_i + \frac{\Delta\bar{x}}{2} \geqq \bar{x} > \bar{x}_i - \frac{\Delta\bar{x}}{2} \\ \bar{y}_j + \frac{\Delta\bar{y}}{2} \geqq \bar{y} > \bar{y}_j - \frac{\Delta\bar{y}}{2} \end{aligned} \tag{1}$$

is true, by S_{ij} ($i = 1, 2, \ldots, I$, $j = 1, 2, \ldots, J$).

The conventional frequency-plot gives the number of the (x_l, x_l) point pairs in the S_{ij} ($i = 1, 2, \ldots, I$; $j = 1, 2, \ldots, J$) domain whereas the Z-plot gives the mean values of the Z_l values of these point pairs. On the basis of probability theory we assume that the differences between the expected and measured value of the logs follow a Gaussian distribution or can be approximated by that. Thus in the lth sampling point the probability density that the expected value of the x_l log value with standard deviation σ_{xl} is $\bar{x}$:

$$\frac{\mathrm{d}q_l(\bar{x})}{\mathrm{d}\bar{x}} = \frac{1}{\sqrt{2\pi}\,\sigma_{xl}} \mathrm{e}^{-\frac{(\bar{x}-x)^2}{2\sigma_{xl}^2}}; \quad l = 1, 2, \ldots, L. \tag{2}$$

Similarly, the probability density that the expected value of the y_l log value with standard deviation σ_{yl} is $\bar{y}$:

$$\frac{\mathrm{d}r_l(\bar{y})}{\mathrm{d}\bar{y}} = \frac{1}{\sqrt{2\pi}\sigma_{yl}} \mathrm{e}^{-\frac{(\bar{y}-y_1)^2}{2\sigma_{yl}^2}}; \quad l = 1, 2, \ldots, L \tag{3}$$

where $q_l(\bar{x})$ and $r_l(\bar{y})$ are the distrubution functions of x_l and y_l respectively. If we plot density functions (2) and (3) on the respective axes of the co-ordinate system, we can see from Fig. 1 that these curves have maxima at the x_l and y_l log values and are Gaussian curves dependent on the degree of the standard deviations σ_{xl} and σ_{yl}.

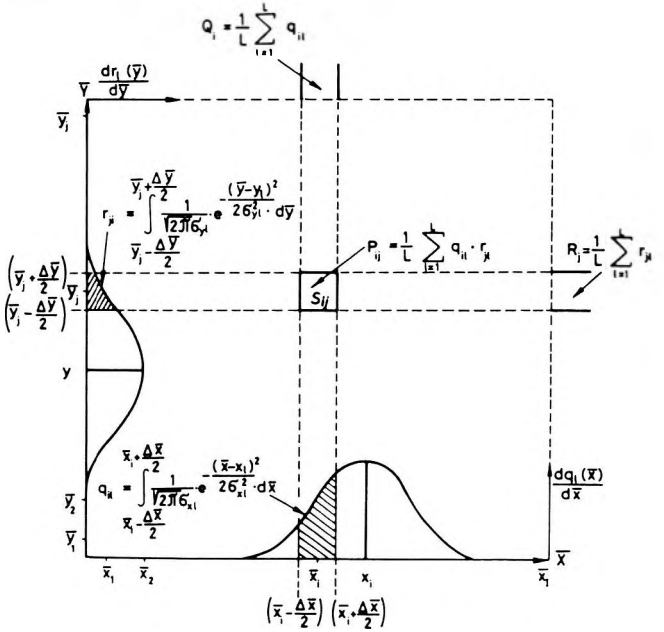

Fig. 1. Construction of probability plot

1. ábra. A gyakorisági valószínűség-eloszlás előállítása

Рис. 1. Составление вероятностной диаграммы.

By means of probability density function (2) we can calculate the level of probability of the expected value $\bar{x}$ of the measured value x_l being in the ith interval between the points $\left(\bar{x}_i - \frac{\Delta\bar{x}}{2}\,;\ \bar{x}_i + \frac{\Delta\bar{x}}{2}\right)$:

$$q_{il} = \int_{\bar{x}_i - \frac{\Delta\bar{x}}{2}}^{\bar{x}_i + \frac{\Delta\bar{x}}{2}} \frac{1}{\sqrt{2\pi}\sigma_{xl}} e^{-\frac{(\bar{x} - x_l)^2}{2\sigma_{xl}^2}} d\bar{x} \tag{4}$$

$$i = 1, 2, \ldots, I; \quad l = 1, 2, \ldots, L.$$

Similarly, the probability that the expected value y of the measured value y_l is in the jth interval between the points $\left(\bar{y}_j - \frac{\Delta\bar{y}}{2} ; \bar{y}_j + \frac{\Delta\bar{y}}{2}\right)$ is:

$$r_{jl} = \int_{\bar{y}_j - \frac{\Delta\bar{y}}{2}}^{\bar{y}_j + \frac{\Delta\bar{y}}{2}} \frac{1}{\sqrt{2\pi}\sigma_{yl}} e^{-\frac{(y - y_l)^2}{2\sigma_{yl}^2}} d\bar{y} \tag{5}$$

$$j = 1, 2, \ldots, J; \quad l = 1, 2, \ldots, L.$$

Figure 1 also shows that the probability q_{il} is the area in the interval of the Gaussian distribution curve between the points $\left(\bar{x}_i - \frac{\Delta\bar{x}}{2}\right)$ and $\left(\bar{x}_i + \frac{\Delta\bar{x}}{2}\right)$ where the maximum of the curve is at the measured value x_l and the standard deviation is σ_{xl}. Similarly, probability r_{jl} is the area in the interval of the Gaussian distribution curve between the points $\left(\bar{y}_j - \frac{\Delta\bar{y}}{2}\right)$ and $\left(\bar{y}_j + \frac{\Delta\bar{y}}{2}\right)$ where the maximum of the curve is at the measured value y_l and the standard deviation is σ_{yl}.

One can see that the measured values x_l and y_l need not be in the $\left(\bar{x}_i - \frac{\Delta\bar{x}}{2} ; \bar{x}_i + \frac{\Delta\bar{x}}{2}\right)$ and $\left(\bar{y}_j - \frac{\Delta\bar{y}}{2} ; \bar{y}_j + \frac{\Delta\bar{y}}{2}\right)$ intervals so that the probability values differ from zero. We can also see that proportionately to the value of the standard deviation and the width of the interval one measurement value may contribute to several adjacent intervals.

Since the magnitude of the whole area below the Gaussian curve is unity the sum of the probabilities assigned to the intervals of the co-ordinate axes is also unity. The smaller the values of the standard deviations in relation to the width of the intervals the fewer the intervals they contribute to but the higher are these probability values. Conversely, the greater the values of the standard deviations in relation to the width of the intervals the more the intervals they contribute to but the lower the probability values there are for this.

It is obtained from integral probabilities (4) and (5) separately that the measured values x_l and y_l approximate the expected values of the ith interval of the $\bar{X}$ axis and the jth interval of the $\bar{Y}$ axis respectively. The question arises as to what is the resulting probability that the expected values $\bar{x}$ and $\bar{y}$ of the

measured values x_l and y_l be in the rectangular domain defined by the inequality (1). Utilizing the fact that the x_l and y_l measured data are unrelated, the resulting probability is the product of the probabilities q_{il} defined by (4) and r_{jl} given by (5):

$$p_{ijl} = q_{il} \cdot r_{jl}$$
$$i = 1, 2, \ldots, I; \quad j = 1, 2, \ldots, J; \quad l = 1, 2, \ldots, L. \tag{6}$$

Probability p_{ijl} obtained from (6) indicates that the expected values $\bar{x}$ and $\bar{y}$ of the x_l and y_l measured value pair are defined in the S_{ij} domain by inequality (1).

In the case of having L measured value pairs the mean value of the probabilities given by (6) can be obtained for all the domains of the co-ordinate system:

$$P_{ij} = \frac{1}{L} \sum_{l=1}^{L} p_{ijl}$$
$$i = 1, 2, \ldots, I; \quad j = 1, 2, \ldots, J. \tag{7}$$

The average probability P_{ij} shows the level of average probability that the expected values of the measured value pairs be in the S_{ij} domain of the co-ordinate system. Useful information can also be obtained by forming the sum of the average probabilities P_{ij} related to j and i and given by (7):

$$Q_i = \sum_{j=-\infty}^{+\infty} P_{ij} = \frac{1}{L} \sum_{l=1}^{L} q_{il} \left(\sum_{j=-\infty}^{+\infty} r_{jl} \right) = \frac{1}{L} \sum_{l=1}^{L} q_{il} \tag{8}$$
$$i = 1, 2, \ldots, I$$

$$R_j = \sum_{i=-\infty}^{+\infty} P_{ij} = \frac{1}{L} \sum_{l=1}^{L} r_{jl} \left(\sum_{i=-\infty}^{+\infty} q_{il} \right) = \frac{1}{L} \sum_{l=1}^{L} r_{jl}. \tag{9}$$

When deriving (8) and (9) we utilized the fact that the sums of the $\bar{x}$ and $\bar{y}$ domains of the probabilities q_{il} — defined by (4) — and r_{jl} — defined by (5) — between $-\infty$ and $+\infty$ are equal with the whole area below the Gaussian curves, i.e. with unity.

The probabilities Q_i given by (8) characterize only the probability distribution of the x_l log values whereas the probabilities R_j given by (9) characterize only that of the y_l log values. In order to visualize the values of the probabilities P_{ij} $(i = 1, 2, \ldots, I; j = 1, 2, \ldots, J)$, Q_i $(i = 1, 2, \ldots, I)$ and R_j $(j = 1, 2, \ldots, J)$ similarly to Fig. 1, we introduce the term probability plot.

If standard deviations σ_{xl} and σ_{yl} were consecutively negligible, taking zero for their values, the integrates (4) and (5) could only be zero and one and thus the conventional frequency plot was obtained again. The domains characterizing the certain rock types — the probability values being greater than in their environments — can be determined on the basis of the probabilities of the co-ordinate system. Since in the calculation of the average probabilities P_{ij} not only the x_l, y_l values in the S_{ij} domain play a part but also the point pairs in

the neighbouring domains, so the average probabilities P_{ij} already show a filtered character.

When investigating the connection of the x_l, y_l, z_l ($l = 1, 2, \ldots, L$) values measured by depth points of threee logs probability P_{ij} given by relations (6) and (7) shows that the expected values $\bar{y}$ of the point pairs x_l, y_l are in domain S_{ij} given by inequality (1). Since the probability of a single point pair may differ from zero in several S_{ij} domains the log value z_l with standard deviation σ_{zl} can no longer be assigned exclusively to a single S_{ij} domain of the co-ordinate system. Therefore instead of a simple mean a weighted mean value should be produced considering the probability p_{ijl} and the extent of the standard deviation.

When forming the weighted mean which can be assigned to the individual domains the weighting factor is taken to be in direct proportion to the probability $p_{ijl} = q_{il} \cdot r_{jl}$ of its originating from the given domain and to be inversely proportional with the square of the standard deviation σ_{zl}^2 characterizing the measurement value z_l. The latter means that the more accurate log value with smaller standard deviation plays a greater part in the forming of the mean than the less accurate log value with greater standard deviation. Forming the weighted means $\bar{Z}_{ij}$ in the way said earlier we can write:

$$\bar{Z}_{ij} = \frac{\sum_{l=1}^{L} \frac{q_{il} \cdot r_{jl}}{\sigma_{zl}^2} \cdot z_l}{\sum_{l=1}^{L} \frac{q_{il} \cdot r_{jl}}{\sigma_{zl}^2}} \qquad (10)$$

$$i = 1, 2, \ldots, I; \quad j = 1, 2, \ldots, J.$$

The weighted mean $\bar{Z}_i^{(x)}$ — which can be assigned to the ith interval between the points $\left(\bar{x}_i - \frac{\Delta\bar{x}}{2}\right)$ and $\left(\bar{x}_i + \frac{\Delta\bar{x}}{2}\right)$ on the $\bar{X}$ axis — can similarly be formed:

$$\bar{Z}_i^{(x)} = \frac{\sum_{l=1}^{L} \frac{q_{il}}{\sigma_{zl}^2} \cdot z_l}{\sum_{l=1}^{L} \frac{q_{il}}{\sigma_{zl}^2}}. \qquad (11)$$

$$i = 1, 2, \ldots, I$$

The same is true for the forming of the weighted mean $\bar{Z}_j^{(y)}$ which can be assigned to the jth interval between the points $\left(\bar{y}_j - \frac{\Delta\bar{y}}{2}\right)$ and $\left(\bar{y}_j + \frac{\Delta\bar{y}}{2}\right)$ on the $\bar{Y}$ axis:

$$\bar{Z}_j^{(y)} = \frac{\sum_{l=1}^{L} \frac{r_{jl}}{\sigma_{zl}^2} \cdot z_l}{\sum_{l=1}^{L} \frac{r_{jl}}{\sigma_{zl}^2}}. \qquad (12)$$

$$j = 1, 2, \ldots, J$$

The most probable Z value that can be assigned to the $\bar{x}_i$, $\bar{y}_i$ co-ordinates on the basis of log values x_l, y_l, z_l is given by the weighted mean $\bar{Z}_{ij}$ of relation (10). On the basis of this the domains of the co-ordinate system can be determined in which the $\bar{Z}_{ij}$ values are nearly constant, i.e. characteristic for only one rock type.

The most probable values of the z_l log values are assigned to the respective $\bar{x}_i$ and $\bar{y}_j$ values of the co-ordinate system by the weighted means $\bar{Z}_i^{(x)}$ and $\bar{Z}_j^{(y)}$. On the basis of this it can be decided whether there is a correlation between the respective logs and if yes, then to what extent. Since for the weighted means related to the individual domains not only those points are considered whose values x_l, y_l are in the S_{ij} domain but more than these (i.e. those whose probabilities obtained for the S_{ij} domain are not zero), the weighted mean values are more reliable than the simple mean values and the adjacent ones do not oscillate considerably.

In order to visualize the $\bar{Z}_{ij}$ ($i = 1, 2, \ldots, I; j = 1, 2, \ldots, J$) as well as the $\bar{Z}_i^{(x)}$ ($i = 1, 2, \ldots, I$) and the $\bar{Z}_j^{(y)}$ ($j = 1, 2, \ldots, J$) weighted means as in *Fig. 2*, we introduce the term ZW-plot. If the limit values of the standard deviations σ_{xl}, σ_{yl} approach zero and all the possible l values of the standard deviation σ_{zl} were to be constant then Z_{ij} would be reduced to a simple mean and the conventional

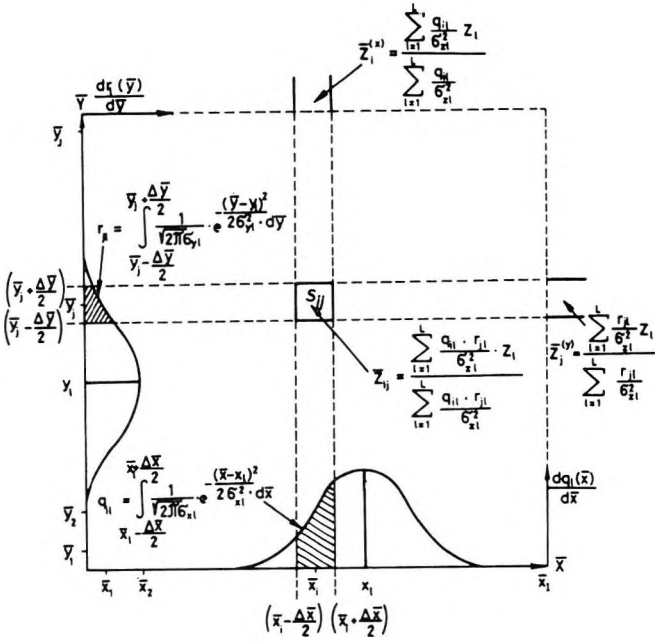

Fig. 2. Construction of weighted mean (ZW) plot

2. ábra. A súlyozott átlagérték (ZW) eloszlás előállítása

Рис. 2. Составление диаграммы средневзвешенного значения (ZW).

Z-plot would be obtained again. To interpret the ZW-plot for geophysical purposes it is necessary to know the standard deviations of the weighted means calculated by formulae (10), (11) and (12). For the reliable determination of the domains characteristic for certain lithological formations the comparison of the means, i.e. the forming of their difference, is not enough, since the standard deviations of the latter are needed that is equal to the square root extracted from the sum of the square of the standard deviation of the two means.

Forming the standard deviations σ_{ij}, $\sigma_i^{(x)}$ and $\sigma_j^{(y)}$ of the weighted means $\bar{Z}_{ij}$, $\bar{Z}_i^{(x)}$ and $\bar{Z}_j^{(y)}$ in the usual way, we obtain:

$$\sigma_{ij} = \left[\sum_{l=1}^{L}\left(\frac{\partial \bar{Z}_{ij}}{\partial z_l}\right)^2 \cdot \sigma_{zl}^2\right]^{1/2} = \frac{\sqrt{\sum_{l=1}^{L}\frac{q_{il}^2 \cdot r_{jl}^2}{\sigma_{zl}^2}}}{\sum_{l=1}^{L}\frac{q_{il} \cdot r_{jl}}{\sigma_{zl}^2}} \qquad (13)$$

$$i = 1, 2, \ldots, I; \quad j = 1, 2, \ldots, J$$

$$\sigma_i^{(x)} = \left[\sum_{l=1}^{L}\left(\frac{\partial \bar{Z}_i^{(x)}}{\partial z_l}\right)^2 \cdot \sigma_{zl}^2\right]^{1/2} = \frac{\sqrt{\sum_{l=1}^{L}\frac{q_{il}^2}{\sigma_{zl}^2}}}{\sum_{l=1}^{L}\frac{q_{il}}{\sigma_{zl}^2}} \qquad (14)$$

$$i = 1, 2, \ldots, I$$

$$\sigma_j^{(y)} = \left[\sum_{l=1}^{L}\left(\frac{\partial \bar{Z}_j}{\partial z_l}\right)^2 \cdot \sigma_{zl}^2\right]^{1/2} = \frac{\sqrt{\sum_{l=1}^{L}\frac{r_{jl}^2}{\sigma_{zl}^2}}}{\sum_{l=1}^{L}\frac{r_{jl}}{\sigma_{zl}^2}} \qquad (15)$$

$$j = 1, 2, \ldots, J.$$

On examining the relations obtained for standard deviations (13), (14), (15) we can see that the standard deviations decrease with the increase in the number of the data from which the means are formed even when highly uncertain data are included in the forming of the mean, and that they are smaller in the domain to which the data of smaller standard deviation belong.

Comparison with the probability plot is also interesting: while in the case of the probability plot the probabilities are higher inside the domains characteristic for the rock types, then here the values of the standard deviations are smaller exactly inside the domain and are greater at the boundaries. For the diagram of standard deviations σ_{ij} ($i = 1, 2, \ldots, I$; $j = 1, 2, \ldots, J$) $\sigma_i^{(x)}$ ($i = 1, 2, \ldots, I$) and $\sigma_j^{(y)}$ ($j = 1, 2, \ldots, J$) as in *Fig. 3* we introduce the term SD-plot. If the SD-plot is always applied together with the respective ZW-plot the determination of the domains characteristic for the rock types can be more reliable.

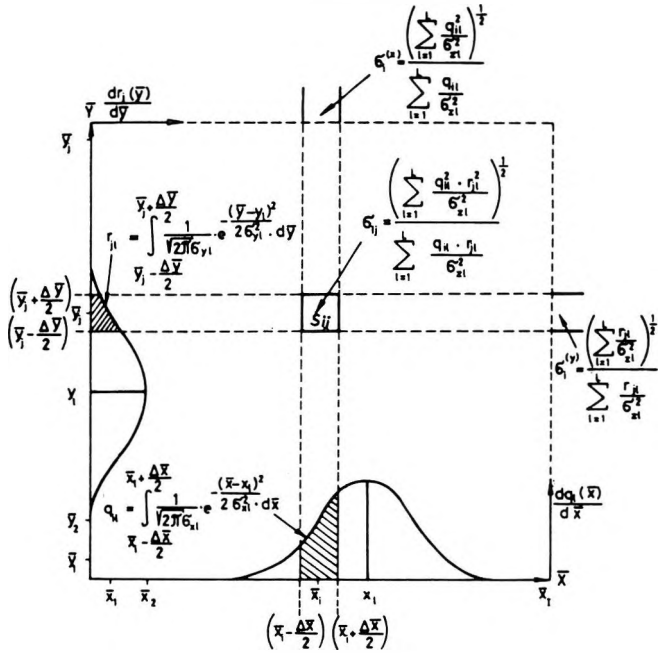

Fig. 3. Construction of standard deviation (SD) plot

3. ábra. A szóráseloszlás (SD) előállítása

Рис. 3. Составление диаграммы дисперсии (SD).

The domains characteristic for the rock types can reliably be seperated if the difference between the weighted means characteristic for the two domains is greater than two or three standard deviations of the square root extracted from the respective squares of the standard deviations. Otherwise these can only be incidental oscillations and the dividing into separate domains is not reliable.

4. Applications

Estimation of the standard deviations

In practical applications the following relations are used to estimate the standard deviations:

$$\begin{aligned} \sigma_{xl}^2 &\approx (\varepsilon_{x1} + \varepsilon_{x2} \cdot x_l)^2 + (\varepsilon_{x3} \cdot x_l')^2 \\ \sigma_{yl}^2 &\approx (\varepsilon_{y1} + \varepsilon_{y2} \cdot y_l)^2 + (\varepsilon_{y3} \cdot y_l')^2 \\ \sigma_{zl}^2 &\approx (\varepsilon_{z1} + \varepsilon_{z2} \cdot z_l)^2 + (\varepsilon_{z3} \cdot z_l')^2 \\ l &= 1, 2, \ldots, L \end{aligned} \tag{16}$$

where x'_l, y'_l, z'_l are the derivatives according to depth of the individual logs in the lth sampling point, $\varepsilon_{x1}, \varepsilon_{y1}, \varepsilon_{z1}$ are the parameters characterizing the absolute error, whereas ε_{x2}, ε_{y2}, ε_{z2} are the parameters characterizing the relative error and ε_{x3}, ε_{y3}, ε_{z3} the ones characterizing the error dependent on the derivative and considering the effect of the relative depth deviation. From (16) we can see that the standard deviations of the logs may vary from point to point and may be highly dependent on the log values.

If the derivative is great, i.e. the shape of log is steep (at the bed boundaries) and the standard deviation is also high, i.e. the log value is not absolutely reliable, the derivative contributes to the probability of several domains in the probability plot, whereas in the ZW-plot it plays a smaller part in the forming of the mean value. Conversely, if the derivative is small, i.e. the course of the log is smooth (inside the layers), the standard deviation is small, the log value is more reliable and as a result of appearing sharply on the probability plot contributes considerably to the probability of less domains whereas on the ZW-plot it plays a greater part in the forming of the mean.

The computer program of the method

The language of the computer program of the method developed is FORTRAN–IV. The names of the logs to be used, the depth interval to be investigated and the error parameters necessary for the standard deviations estimated by (16) should be given as input data.

The results are printed out in the form illustrated in Figs. 1–3. At the top the type of cross probability plot, the name and the depth interval of the well, the names of the logs assigned to the $\bar{X}$, $\bar{Y}$ and $\bar{Z}$ co-ordinate axes and the number of the investigated points are printed out by the program.

The relation is also printed here on the basis of which the value of the probability and the weighted mean can be obtained from the values in the inside of the co-ordinate system.

Axes $\bar{X}$ and $\bar{Y}$ are divided into fifty parts between the minimum and maximum log values occurring and thus a net of 50×50 is made by the program. When printing the probabilities 50 is assigned to the maximal probability and so numbers from one to fifty may occur in the domains of the co-ordinate system.

In order to prepare the ZW-plot the $\bar{Z}$ axis is also divided into 50 parts between the minimum and maximum value of the log and so numbers from zero to fifty may occur in the domains of the co-ordinate system. In the case of the SD-plot the number 50 belongs to the maximum standard deviation and so the numbers 0 to 50 may occur in the domains of the co-ordinate system. Conversion into real values is enabled in every case by the relation printed in the heading. The real values of the probabilities, and the weighted means and standard deviations relating to the individual lines and columns can also be determined by means of this relation. In order to decrease computation time the

integrals given by (4) and (5) are approximated by using the table function given in the article of SZENDRŐ [1983].

Example

The logs in the example can be seen in *Fig. 4*, the values of the parameters necessary for estimating the standard deviations are in *Tables I* and *II*. The standard deviations calculated by relation (16) on the basis of the parameters of Table I are zero, i.e. the results obtained correspond to the conventional frequency-plot and Z-plot. The standard deviation values estimated by relation (16) on the basis of the parameters of Table II are already right; the standard deviations may vary from point-to-point depending on the log values and their derivative. The results in accordance with Table I can be seen in *Figs. 5* and *6* whereas the results obtained by considering the standard deviations estimated by the error parameters of Table II are in *Figs. 7–9*. The SD-plot belonging to the ZW-plot in Fig. 8 is shown in Fig. 9.

Logs	Absolute error parameter	Relative error parameter	Error parameter depending on the derivative
X = FIN	$\varepsilon_{x1} = 0$	$\varepsilon_{x2} = 0$	$\varepsilon_{x3} = 0$
Y = FID	$\varepsilon_{y1} = 0$	$\varepsilon_{y2} = 0$	$\varepsilon_{y3} = 0$
Z = RTR	$\varepsilon_{z1} = 0$	$\varepsilon_{z2} = 0$	$\varepsilon_{z3} = 0$

Table I. Values of the error parameters of the logs, illustrated as an example, for conventional crossplots

I. táblázat. A példaként bemutatott szelvények hibaparaméterei a hagyományos eloszlási diagramok esetében

Таблица I. Значения параметров ошибок по изученным профилям для случая традиционных прямоугольных диаграмм

Logs	Absolute error parameter	Relative error parameter	Error parameter depending on the derivative
X = FIN	$\varepsilon_{x1} = 0.01$	$\varepsilon_{x2} = 0.01$	$\varepsilon_{x3} = 0.05$ m
Y = FID	$\varepsilon_{y1} = 0.01$	$\varepsilon_{y2} = 0.01$	$\varepsilon_{y3} = 0.05$ m
Z = RTR	$\varepsilon_{z1} = 0.01\ \Omega m^{-1}$	$\varepsilon_{z2} = 0.01$	$\varepsilon_{z3} = 0.05$ m

Table II. Values of the error parameters of the logs, illustrated as an example, in the case of the probability theory

II. táblázat. A példaként bemutatott szelvények hibaparaméterei a valószínűségelméleti tárgyalás esetében

Таблица II. Значения параметров ошибок по изученным профилям для случая рассмотрения в рамках теории вероятностей.

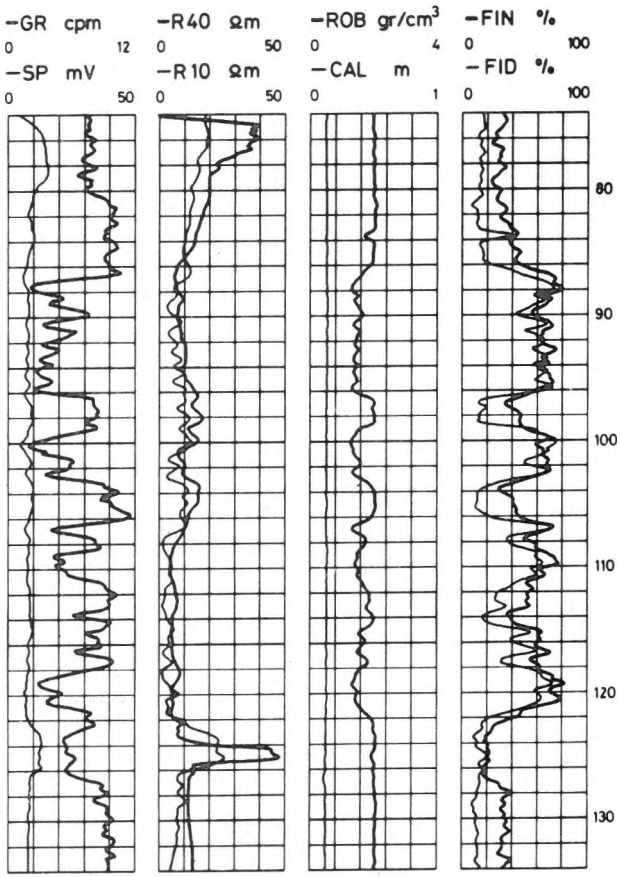

Fig. 4. Logs of a borehole from a North-Hungarian lignite-producing area (Visonta)

4. ábra. A példaként szereplő Visonta környéki lignitkutató fúrásban mért görbék: GR = természetes gamma; SP = természetes potenciál; R40 = 40 cm szondahosszú ellenállás; R10 = 10 cm szondahosszú ellenállás; ROB = sűrűség; CAL = lyukátmérő; FIN = neutron porozitás; FID = gamma-gamma porozitás

Рис. 4. Кривые, полученные по скважине на лигниты в окрестностях с. Вишонта (Северная Венгрия):
GR — естественная гамма-активность; SP — естественные токи; R40 — сопротивление, измеренное зондом в 40 см; R10 — сопротивление, измеренное зондом в 10 см; ROB — илотност; CAL — диаметр скважины; FIN — пористотсть по нейтрон-нейтронной кривой. FID — пористость по гамма-гамма кривой.

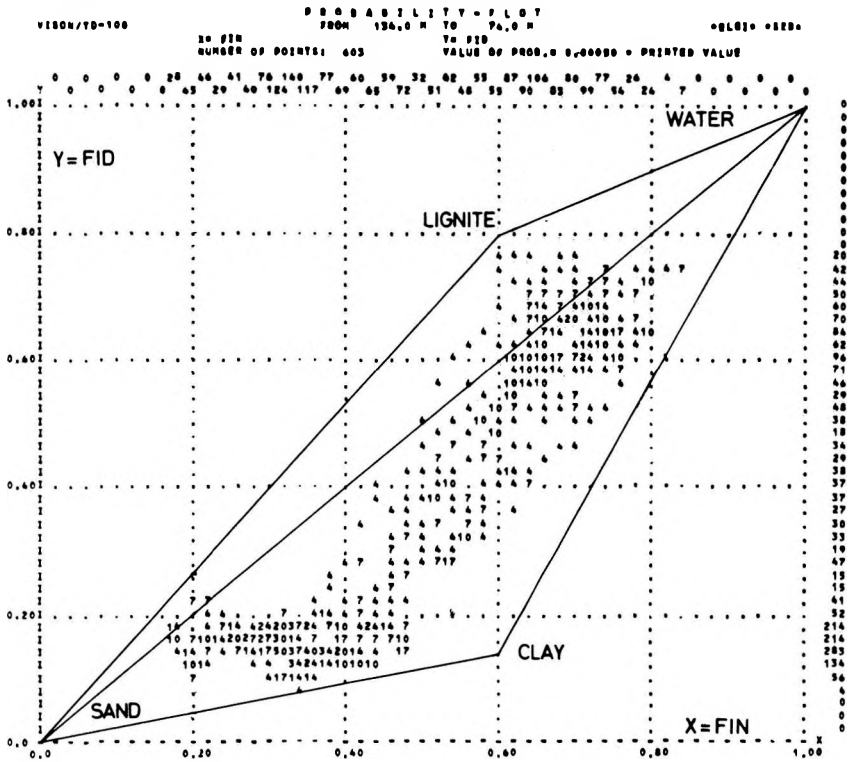

Fig. 5. Conventional frequency plot

5. ábra. Hagyományos gyakorisági eloszlás, a szórásokat nem véve figyelembe: FIN = neutron porozitás; FID = gamma-gamma porozitás

Рис. 5. Вероятностное распределение, совпадающее с таковым на традициональной прямоугольной диаграмме без учета дисперсий:
FIN — пористость по нейтрон-нейтронной кривой; FID — пористость по гамма-гамма кривой.

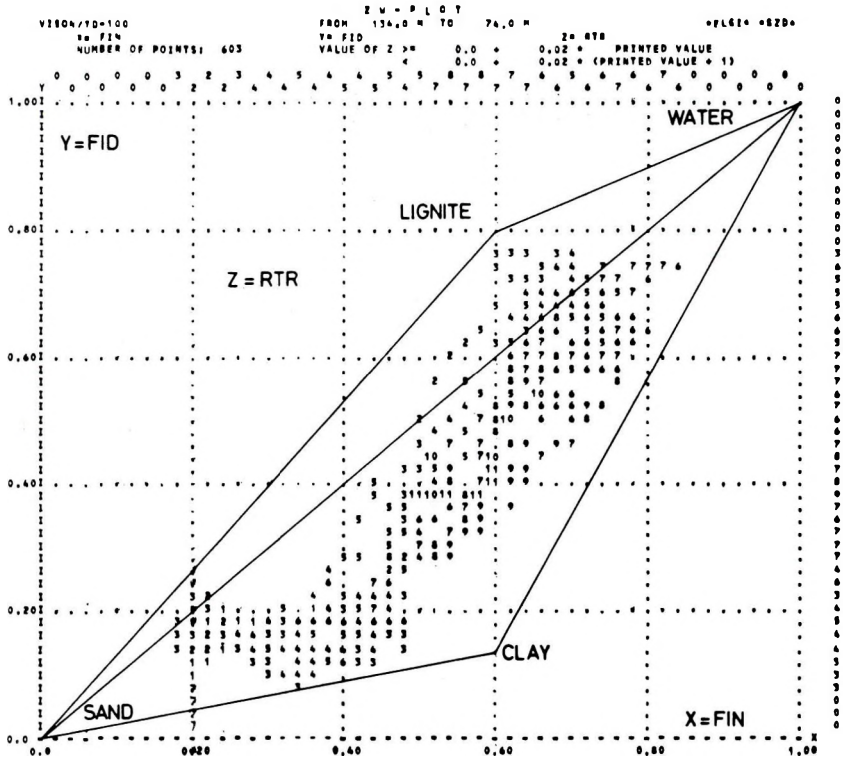

Fig. 6. Conventional Z-plot

6. ábra. Hagyományos átlagérték-eloszlás, a szórásokat nem véve figyelembe
FIN = neutron porozitás; FID = gamma-gamma porozitás; RTR = az ellenállás reciproka

Рис. 6. Распределение средних значений, совпадающее с таковым на традициональной диаграмме без учета дисперсий:
FIN — пористость по нейтрон-нейтронной кривой; FID — пористость по гамма-гамма кривой, RTR — величина, обратная сопротивлению.

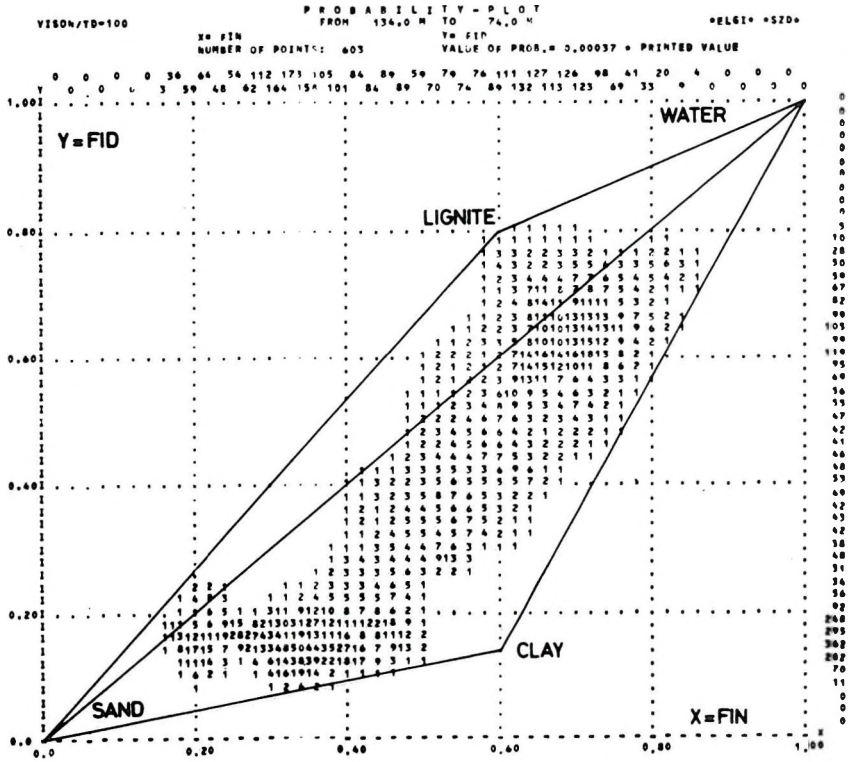

Fig. 7. Probability plot

7. ábra. Gyakorisági valószínűség-eloszlás

Рис. 7. Результаты по изучаемой скважине на вероятностной диаграмме.

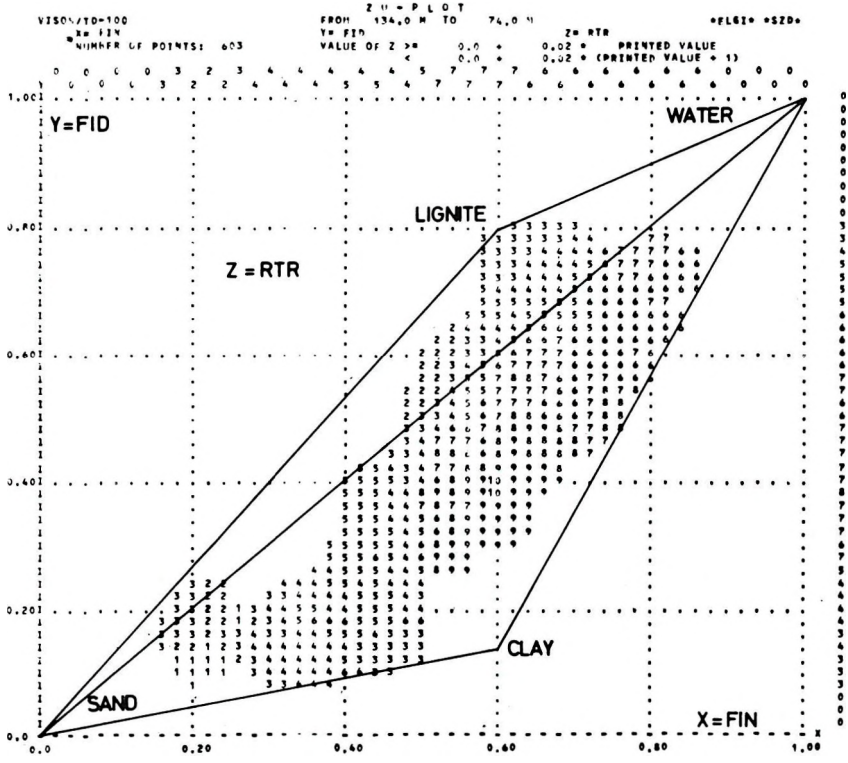

Fig. 8. Weighted mean ZW-plot

8. ábra. Súlyozott átlagérték (ZW)

Рис. 8. Результаты по изучаемой скважине на диаграмме ZW.

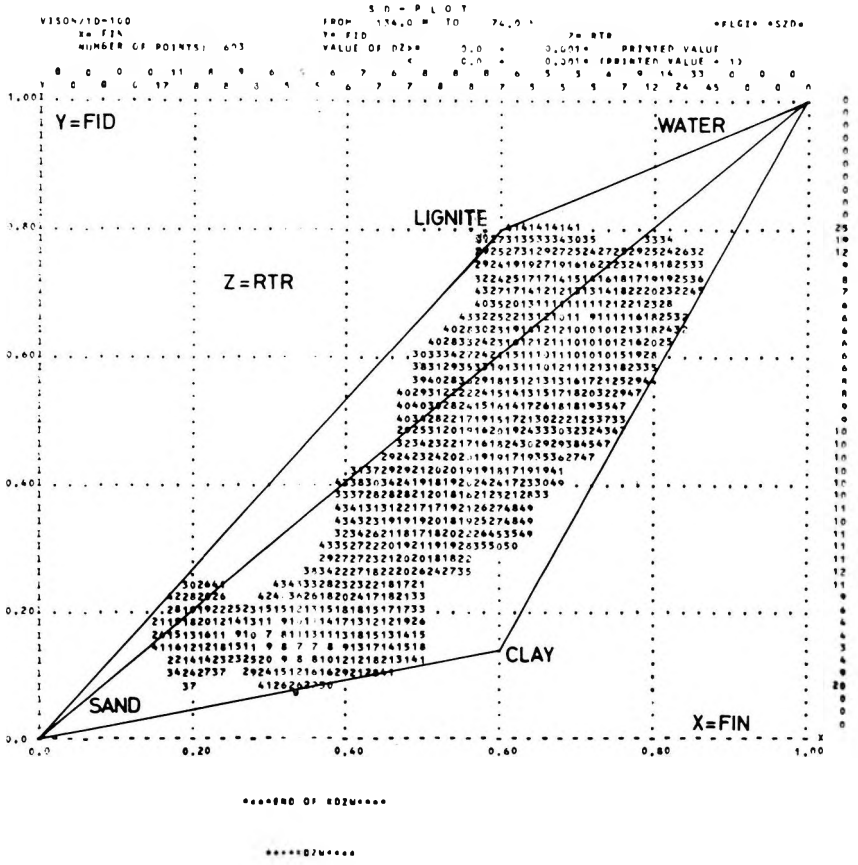

Fig. 9. Standard deviation SD-plot

9. ábra. Szóráseloszlás (SD)

Рис. 9. Результаты по изучаемой скважине на диаграмме SD

The conclusion drawn from the Figures is clear: the adjacent points of the distributions in Figs. 7–9 oscillate to a smaller extent in relation to the conventional plots corresponding to Figs. 5–6, they are of filtered character and the domains characterizing the individual rock-types can be separated with more certainty. The environments of the local maxima of the probability distribution on the probability plot provide good help for separating the domains on the ZW-plot as well as those of the local minima of the standard deviations on the SD-plot.

In the example there is lignite, clay, and sand in the well. Characterizing the log values of the rock types by low, medium and high values the distinction illustrated in *Table III* can be made. The limits of the plain lithological formations were marked on the distribution in Figs. 7–9 according to the classification in Table III simultaneously considering the probability plot, the ZW-plot and the SD-plot.

Logs	Lignite	Clay	Sand
X = FIN	high	high	low
Y = FID	high	medium	low
Z = RTR	medium	high	low

Table III. Log values of the well in the example as a function of lithological formations
III. táblázat. A példaként szereplő kút szelvényértékei a kőzettani jelleg függvényében
Таблица III. Сопоставление профилей по изученной скважине с литологическими подразделениями.

5. Conclusions

Every item of measuring data is considered with two quantities, viz. with the measured value and with its standard deviation, by the method described. When estimating the standard deviation the inaccuracy of the instrument, the possible statistical behaviour of the measured quantity and the inaccuracy of the depth deviation in connection with the derivative of the log may be considered. Considering two logs and dividing the rectangular coordinate system $\bar{X}$, $\bar{Y}$ into domains of rectangle shape the level of probability that the expected values of a point pair relating to a depth be in certain domains can be calculated.

Summing the probabilities of the measuring pairs belonging to the domains and forming the average, a two dimensional average probability distribution is obtained as a result. If this is compared with the frequency plot used so far this shows a "filtered" character where the boundaries of the domains characteristic for the rock types are less faded by the points at the layer boundaries and appear as nearly permanent background noise.

If the related data of three logs are studied the probabilities of certain data pairs can be calculated in the way described above. A weighted mean value is calculated from the data of the third log for every domain where the weights are in direct proportion with the probability of belonging to the given domain

and are inversely proportional with the square of the standard deviation of the data for the third log. Thus a "filtered" weighted mean distribution is obtained the adjacent values of which oscillate to a smaller extent than for the conventional Z-plot.

BIBLIOGRAPHY

BURKE J. A., CAMPBELL R. L., SCHMIDT A. W. 1969: The litho-porosity crossplot. SPWLA Annual Symposium, Paper Y. pp. 827–835

DESBRANDES R. 1985: Encyclopedia of well logging. Editions Technip, Paris, p. 584

FERTL W. H. 1978: Openhole crossplot concepts — A powerful technique in well log analysis. EU90, SPE of AIME, European Offshore Petroleum Conference and Exhibition, London

JÁNOSSY L. 1965: Theory and practice of the evaluation of measurements. Clarendon Press, Oxford

LANG W. H. 1972: Porosity–resistivity cross-plotting. Transactions SPWLA, Paper F

MCFADZEAN T. B. 1973: Cross-plotting — A neglected technique in log analysis. Transactions SPWLA, Paper Y

RATLIFF J. R., THROOP W. H., WILLIAMS F. G., HALL J. D. 1971: Applications of the SARABAND sand–shale technique in North America Transactions SPWLA, Paper P

SCHMIDT A. W., LAND A. G., YUNKER J. D., KILGORE E. C. 1971: Applications of the CORIBAND technique in complex lithologies. Transactions SPWLA, Paper Z

SZENDRŐ D. 1974: Lithologic discrimination by means of well logs (in Hungarian). Mathematics and computers for the interpretation of geological formations. Edition of Hungarian Geological Society, pp. 60–79

SZENDRŐ D. 1981: Application of the statistical lithologic method for the determination of geological formations. Proc. 26th Int. Geoph. Symp., Leipzig, **II.** pp. 489–496

SZENDRŐ D. 1983: A statistical method for lithologic interpretation from well logs. The Log Analyst, **24,** 3, pp. 16–23

SZENDRŐ D. 1984: Special "cross-plots" computed from logs to interpret the presence of raw materials. Proc. 29th. Int. Geoph. Symp., Sofia, pp. 355–363

SZENDRŐ D., KARAS GY., BARÁTH I. 1986: Interpretation of coal exploratory boreholes by the ASOIGIS system. Proc. 31st Int. Geoph. Symp., Gdansk, **I.** pp. 345–355

SPECIÁLIS ELOSZLÁSI DIAGRAMOK KÉSZÍTÉSE KAROTÁZS SZELVÉNYEKBŐL

SZENDRŐ Dénes

A mélyfúrási adatokat eloszlási diagramokon ábrázolva lehetőség van a szelvények közötti statisztikus, korrelációs kapcsolatok vizsgálatára. A mérési értékekhez rendelhető szórások figyelembevétele a pontosabb valószínűségelméleti tárgyalást, s így a szorosabb korrelációs kapcsolatok feltárását teszi lehetővé. A szelvényértékeket valószínűségi változóknak tekintve, mért értékeiktől és differenciahányadosaiktól is függő szórásaik felhasználásával kiszámítható, hogy várható értékeik milyen valószínűséggel lehetnek egyes előre megadott intervallumokban. Koordináta-rendszerben ábrázolva két szelvény esetében így egy kétdimenziós, átlagos valószínűségeloszlást, míg három szelvény esetében egy súlyozott középérték eloszlást kapunk eredményül.

A kidolgozott speciális diagramok módszere a hagyományoshoz viszonyítva „szürt" jelleget mutat. Az új eljárással készített diagramokon a réteghatárok környékén levő mérési adatok kisebb súllyal jelennek meg, így a kőzettípusokra jellemző paraméterek pontosabban határozhatók meg.

СОСТАВЛЕНИЕ СПЕЦИАЛЬНЫХ ПРЯМОУГОЛЬНЫХ ДИАГРАММ ПО КАРОТАЖНЫМ КРИВЫМ

Денеш СЕНДРЁ

Путем изображения каротажных данных на диаграммах распределения обеспечивается возможность изучения статистических, корреляционных связей между кривыми. Учет дисперсий данных измерений дает возможность более точного рассмотрения с точки зрения теории вероятностей, то-есть обнаружения более тесных корреляционных связей. Рассматривая значения, снятые с кривых, в качестве вероятностных переменных, с использованием измеренных значений и дисперсий, зависящих также и от их дифференциалов, можно рассчитать, с какой вероятностью ожидаемые значения попадают в тот или иной заданный интервал. Переходя к системам координат, в случае двух кривых получается двумерное среднее вероятностное распределение, а в случае трех — распределение средневзвешенных значений. Разработанный метод специальных диаграмм распределения обнаруживает в сравнении с традиционными прямоугольными диаграммами признаки фильтрации, поскольку данные измерений, полученные вблизи границ слоев, менее затрудняют точное определение характерных параметров определенных типов горных пород.